SANDIA REPORT

SAND97–0047 • UC–700
Unlimited Release
Printed January 1997

Fire Characterization and Object Thermal Response for a Large Flat Plate Adjacent to a Large JP-4 Fuel Fire

Louis A. Gritzo, Jaime L. Moya, Douglas Murray

Prepared by
Sandia National Laboratories
Albuquerque, New Mexico 87185 and Livermore, California 94550
for the United States Department of Energy
under Contract DE-AC04-94AL85000

Issued by Sandia National Laboratories, operated for the United States Department of Energy by Sandia Corporation.

Available to DOE and DOE contractors from
Office of Scientific and Technical Information
PO Box 62
Oak Ridge, TN 37831

Prices available from (615) 576-8401, FTS 626-8401

Available to the public from
National Technical Information Service
US Department of Commerce
5285 Port Royal Rd
Springfield, VA 22161

NTIS price codes
Printed copy: A05
Microfiche copy: A01

SAND97-0047
Unlimited Release
Printed January 1997

Distribution
Category UC-700

Fire Characterization and Object Thermal Response for a Large Flat Plate Adjacent to a Large JP-4 Fuel Fire

Louis A. Gritzo
Unsteady and Reactive Fluid Mechanics, Org. 9116, MS 0836

Jaime L. Moya
Mechanical and Thermal Environments, Org 9735, MS 0865

Sandia National Laboratories
Albuquerque, NM 87185-0836

Douglas Murray
Environmental/Safety Test and Evaluation, Code 528200D
Naval Air Warfare Center
China Lake, CA 93555

Abstract

A series of three 18.9 m diameter JP-4 pool fire experiments with a large (2.1 m X 4.6 m), flat plate calorimeter adjacent to the fuel pool were recently performed. The objectives of these experiments were to: 1) gain a better understanding of fire phenomenology, 2) provide empirical input parameter estimates for simplified, deterministic Risk Assessment Compatible Fire Models (RACFMs), 3) assist in continuing fire field model code validation and development, and 4) enhance the data base of fire temperature and heat flux to object distributions.

Due to different wind conditions during each experiment, data were obtained for conditions where the plate was not engulfed, fully-engulfed and partially engulfed by the continuous flame zone. Results include the heat flux distribution to the plate and flame thermocouple temperatures in the vicinity of the plate and at two cross sections within the lower region of the continuous flame zone. The results emphasize the importance of radiative coupling (i.e. the cooling of the flames by a thermally massive object) and convective coupling (including object-induced turbulence and object/wind/flame interactions) in determining the heat flux from a fire to an object. The formation of a secondary flame zone on an object adjacent to a fire via convective coupling (which increases the heat flux by a factor of two) is shown to be possible when the object is located within a distance equal to the object width from the fire.

Acknowledgments

This report concludes a multi-year study of the data from a suite of unique fire experiments. The authors would like to thank the following individuals for their participation in this effort.

- John Gilliland, Ed Lusher, and others at the CT-4 test facility for their efforts in preparing and assisting in the execution of the pool fire experiments at the Naval Air Warfare Center at China Lake, California.
- Major John Deplitch and Major Joseph Crews of the Defense Special Weapons Agency (DSWA) for their sponsorship of this effort.
- Sheldon Tieszen, Vernon Nicolette, and Russell Skocypec of Sandia for their technical advice, discussions, and support.

This study was sponsored by the Department of Defense - DSWA, and was performed in part at Sandia National Laboratories which is operated by Lockheed Martin Corp. for the U. S. Department of Energy under Contract DE-AC04-94AL85000.

Table of Contents

List of Figures

List of Tables

1. Introduction

1.1 Background

Exposure to a large hydrocarbon pool fire is one of the many scenarios to be considered when assessing the fire survivability of engineered systems. Such fires occur as a result of transportation accidents. The spectrum of technologies required to accurately predict the fire environment for such scenarios is presently under development at Sandia National Laboratories (SNL). Due to the complex interaction of nonlinear phenomena present in fires, an integrated approach including full scale experiments, the development of advanced diagnostic techniques and the development of a suite of numerical models is required for significant, applicable technical progress to be realized.

In support of this integrated effort, an extensive full scale fuel fire experimental program was initiated at the Naval Air Warfare Center, Weapons Division (NAWCWPNS). The objectives of this program are to: 1) gain a better understanding of fire phenomenology, 2) provide empirical input parameter estimates for simplified, deterministic Risk Assessment Compatible Fire Models (RACFMs) [1], 3) assist in continuing fire field model validation and development [2], and 4) enhance the data base of fire temperature and heat flux to object distribution measurements. These experiments are supported by the Defense Special Weapons Agency (DSWA) as part of a Fuel Fire Technology Base Program. The goal of the Fuel Fire Technology Base Program is to develop validated numerical tools capable of predicting the fuel fire thermal environment resulting from an aircraft or ground transportation accident. These numerical simulation capabilities are required to improve the fidelity of Weapons System Safety Assessments (WSSAs).

As part of the full scale fuel fire experimental program, a series of 18.9 m diameter JP-4 pool fire experiments with a large (2.1 m X 4.6 m) flat plate calorimeter adjacent to the fuel pool were recently performed at NAWCWPNS. One objective of this series is to obtain the data required to validate and further the development of fire field models. The ability to numerically model the fire environment is required to improve the design and assessment of fire-survivable engineered systems. Fire modeling, including the influence of objects on the fire environment and the thermal response of objects, requires that many coupled, nonlinear, physical phenomena be represented. Currently, a fire field model is under development at SNL to predict the fire environment from a "first principles" approach whereby the governing transport and phenomenological equations are solved for all primary relevant variables. The comparison of model predictions and high fidelity experimental data is an essential component of the model development process. Depending on the results of such comparisons, it may be possible to obtain increased confidence in the ability of the model

to predict certain variable fields within the uncertainty inherent in the experimental measurements. In this sense "validation" of one or more aspects of the model can be achieved.

When discrepancies between model predictions and experimental results is observed, an understanding of the fire phenomenology is required to reconcile the differences. This understanding must frequently be developed by investigating the characteristics of the measurements and the details of the model predictions. Based on the results of these investigations, the model and experimental technology development processes are supported in the most efficient manner possible by directing research efforts towards the appropriate areas.

Of all fire scenarios which include an engulfed object, it is important to compare experimental results and model predictions for cases when the object size and shape is such that the geometry of the flame zone is altered due to the presence of the object. These scenarios are difficult to address because the alteration of the flow field due to the presence of the object, and the influence of the altered flow field on the fire physics, must be known to determine the flame zone geometry. The presence of a large flat plate adjacent to the fuel pool (as performed in this series), which serves to redirect the flames toward and along the front surface of the plate, was expected to result in fires within this class of scenarios.

Large computational times are required to perform fire field model simulations. They are therefore not well-suited for the initial series of numerous calculations required by Probabilistic Safety Assessments (PSAs). A suite of simplified, deterministic, risk assessment compatible fire models (RACFMs) are presently being developed at Sandia National Laboratories (SNL) for this purpose. These models apply first principles to the dominant physical phenomena (radiative and advective transport) and rely on empirically-determined parameters to represent the remaining physics [1]. Using this approach, run times are reduced to a level acceptable for PSAs. Presently, predicting the heat release due to combustion, which is largely controlled by mixing and hence requires the numerical simulation of the flow field, is beyond the scope of these models [3]. It is therefore necessary to represent the temperature and radiative property fields which result from combustion of the fuel using empirical parameters. Data generated from large scale experiments, complemented by fire field model simulations, are used to develop the necessary empirical relationships and constants. In many cases, significant differences are observed between these data and commonly accepted estimates which appear in fire protection engineering handbooks [4]. These deviations can largely be attributed to the lack of large scale fire data. It is therefore necessary to supplement the existing knowledge base with data from carefully designed experiments.

Although a comprehensive knowledge of "free fires" (i.e. fires without objects) has yet to be obtained, the most significant immediate benefit to WSSAs is yielded

from an improved ability to quantify the heat flux to *objects* subjected to large fires. One of the most fundamental of these cases occurs when the flames are uniformly advected along a flat surface. Although the presence of a flat plate adjacent to the fuel pool may cause global changes in the continuous flame zone, the region of the fire which is close enough to affect the heat flux to the plate is expected to be composed of flames flowing parallel to the plate surface when the plate is engulfed. Despite the foundational importance of these type of scenarios, this case has not been addressed prior to this study. An additional objective of this series of experiments is to provide data for the development and validation of RACFMs. An improved understanding of the associated fire phenomenology which has not previously been realized due to the lack of the appropriate data is also expected to be acquired as a result of these experiments.

1.2 Objectives

The objectives of this report are to:

1. document the instrumentation employed in the series of experiments
2. document the conditions under which each experiment in the series was performed,
3. present the data collected during the series in a manner suitable for comparison with numerical model predictions,
4. present the data collected during the series needed to determine empirical parameters required by RACFMs,
5. investigate and document trends observed in the data.

Each of these objectives will be addressed in the chapters which follow.

2. Instrumentation

2.1 Overview of Experimental Setup

The experimental series was performed at the NAWCWPNS CT-4 test site. The experimental setup consists of a large, vertical flat plate calorimeter which is located adjacent to an 18.9 m diameter pool fire test pit. The site is at the bottom of a gradually-sloping valley which is approximately 800 m wide. The calorimeter was placed such that the calorimeter surface was normal to prevailing valley wind direction (which is approximately 210^0 clockwise from south). Fire environment instrumentation includes an array of thermocouples and heat flux gauges positioned within the fuel pool in front of the calorimeter and two thermocouple arrays extending from the pool center to slightly beyond the exterior of the north end of the test pit. The test pit is approximately 25 cm deep and is initially filled with approximately 15 cm of water. Prior to each experiment, a fuel pool is formed in the pit by floating military-grade JP-4 fuel on top of the water. The fuel is ignited at three locations by triggering a 110V signal across a book of matches. experiments are concluded when all of the fuel is consumed.

2.2 Vertical Flat Plate Calorimeter Construction, Instrumentation, and Placement

The vertical flat plate calorimeter is constructed from a 2.1 m X 5.2 m X 3 cm thick mild-steel plate mounted on two vertical W5X5 beams. The vertical beams are maintained in an upright position by a triangular support structure. The assembly was constructed at the SNL Lurance Canyon Burn Site and shipped to NAWCWPNS. Design drawings of the assembly are included in Appendix A. The front face of the calorimeter is coated with Pyromark™ flat black paint.

Type-K, 0.16 cm diameter sheathed thermocouples are mounted as shown in Figure 2.1 to the back side of the plate calorimeter at 17 locations. Prior to attaching the thermocouples, a hand grinder was used to remove oxidation at each location on the calorimeter surface. To minimize the influence of conduction through the thermocouple lead on the temperature measurement, the end of each thermocouple was bent to form a "J-hook" with diameter of approximately 2.0 cm. Nichrome strips were then placed on top of the "J-hook" and were tack welded to the calorimeter at approximately 30 locations to secure the thermocouple to the calorimeter surface.

Thermocouples are mounted to the back side of the calorimeter plate at the 14 locations (P1-P14) shown in Figure 2.2. To assess the repeatability associated with the thermocouples and the attachment technique, two thermocouples were installed at three locations (P2 & P3, P7 & P8, and P12 & P13) on the calorimeter. The back

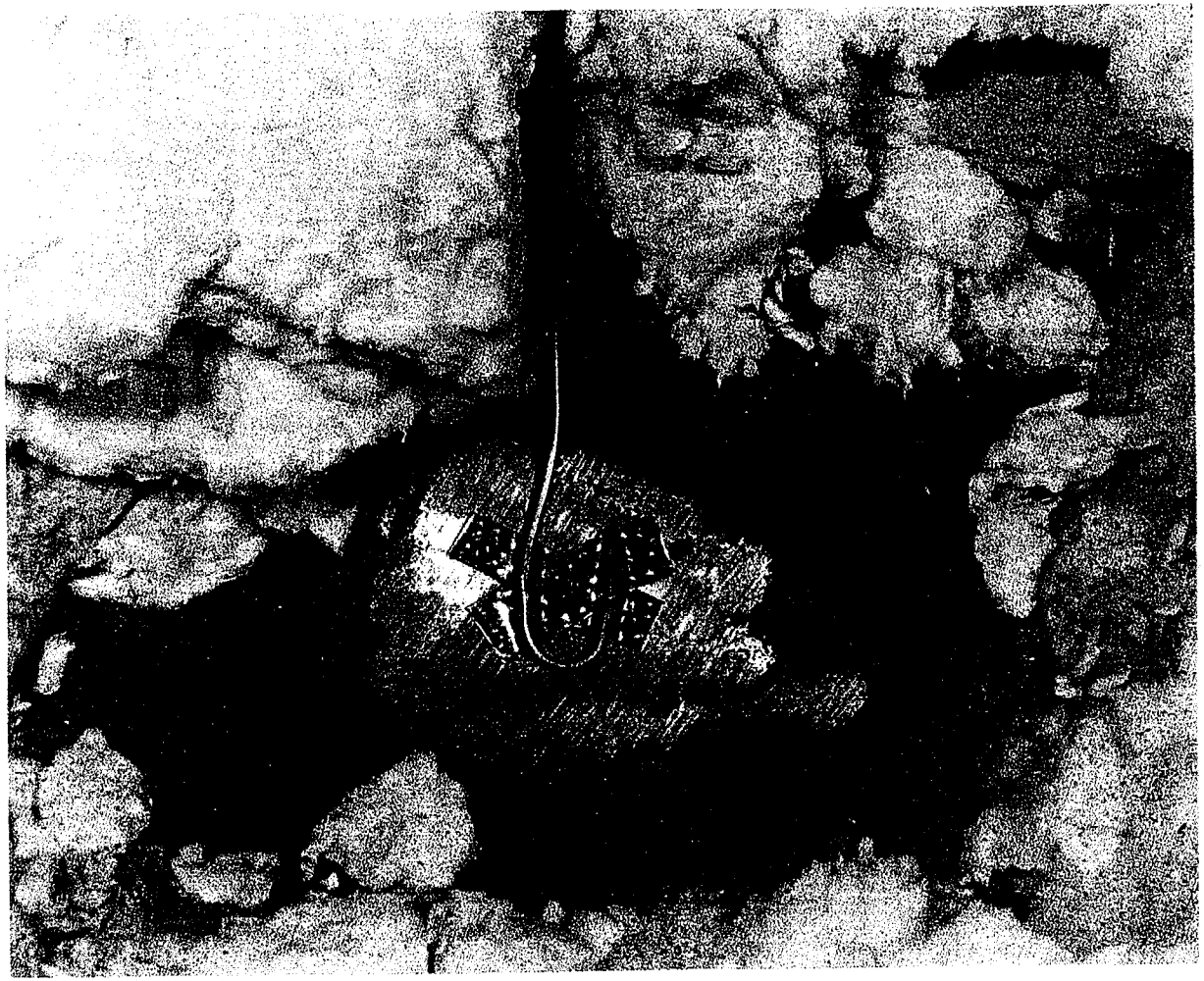

Figure 2.1 Thermocouple Attachment Technique

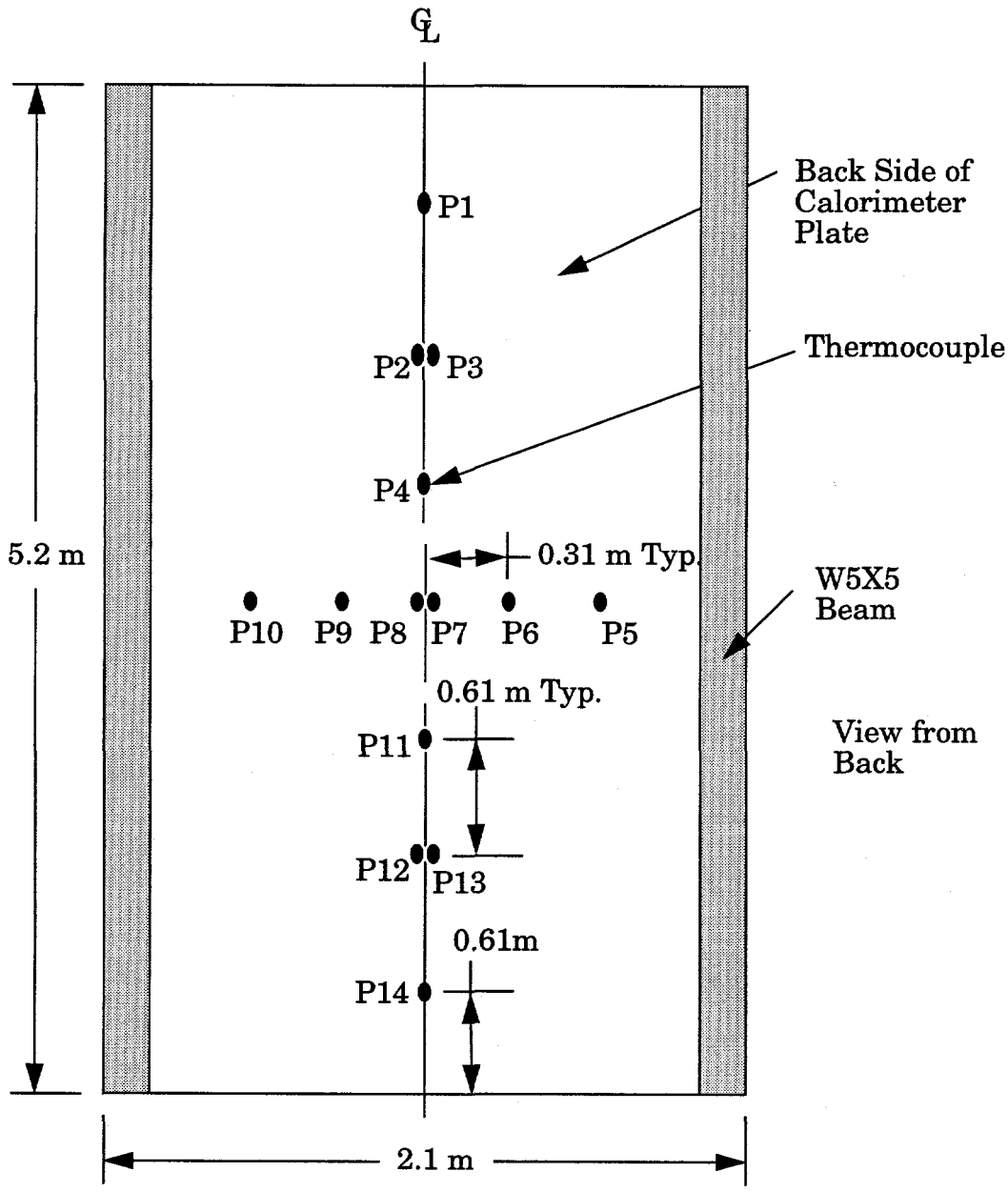

Figure 2.2 Thermocouple Locations on Back of Calorimeter

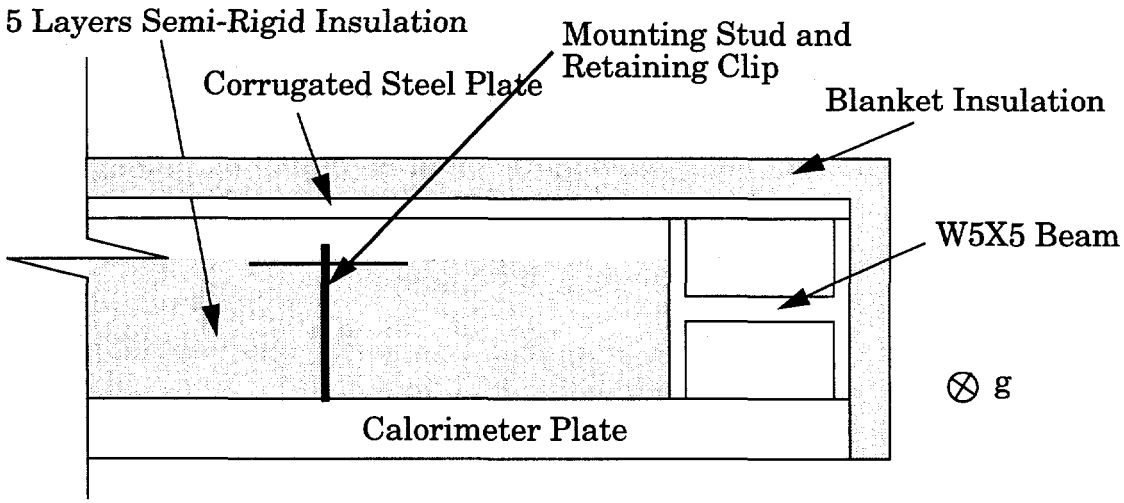

Figure 2.3 Cross Sectional View of Calorimeter Plate

side of the calorimeter plate was insulated with 5 layers of 1.25 cm semi-rigid, ceramic fiber insulation, as shown in Figure 2.3, to provide a boundary condition for an inverse calculation of the heat flux using the measured temperatures. All insulation was attached using 0.32 cm diameter mild steel mounting studs with retaining clips. The semi-rigid insulation was enclosed by a 0.32 cm corrugated steel plate which was attached to the back side of the vertical W5X5 beams. Thermocouples were mounted at 3 locations on the corrugated plate, as shown in Figure 2.4. The exterior of the corrugated plate, the exposed sides of the W5X5 beams, and the remainder of the support assembly were covered with 2.54 cm thick ceramic fiber blanket insulation for thermal protection. Insulation on the exterior of the support assembly was held in place using stainless steel wire. To avoid toppling of the assembly into the fuel pool, supports extending to the bottom of the test pit were welded to the front of the calorimeter support structure as shown in Figure 2.5.

Leads from thermocouples mounted on the back side of the calorimeter were routed on top of the semi-rigid insulation, covered with ceramic fiber blanket, and routed through the bottom of the assembly. Thermocouples located on the corrugated steel back plate were routed along the back plate and fastened together with the remaining thermocouples at the bottom of the assembly. The bundle of leads was covered with ceramic fiber blanket insulation for protection against the fire environment up to the point where the leads were immersed in the water contained in the test pit.

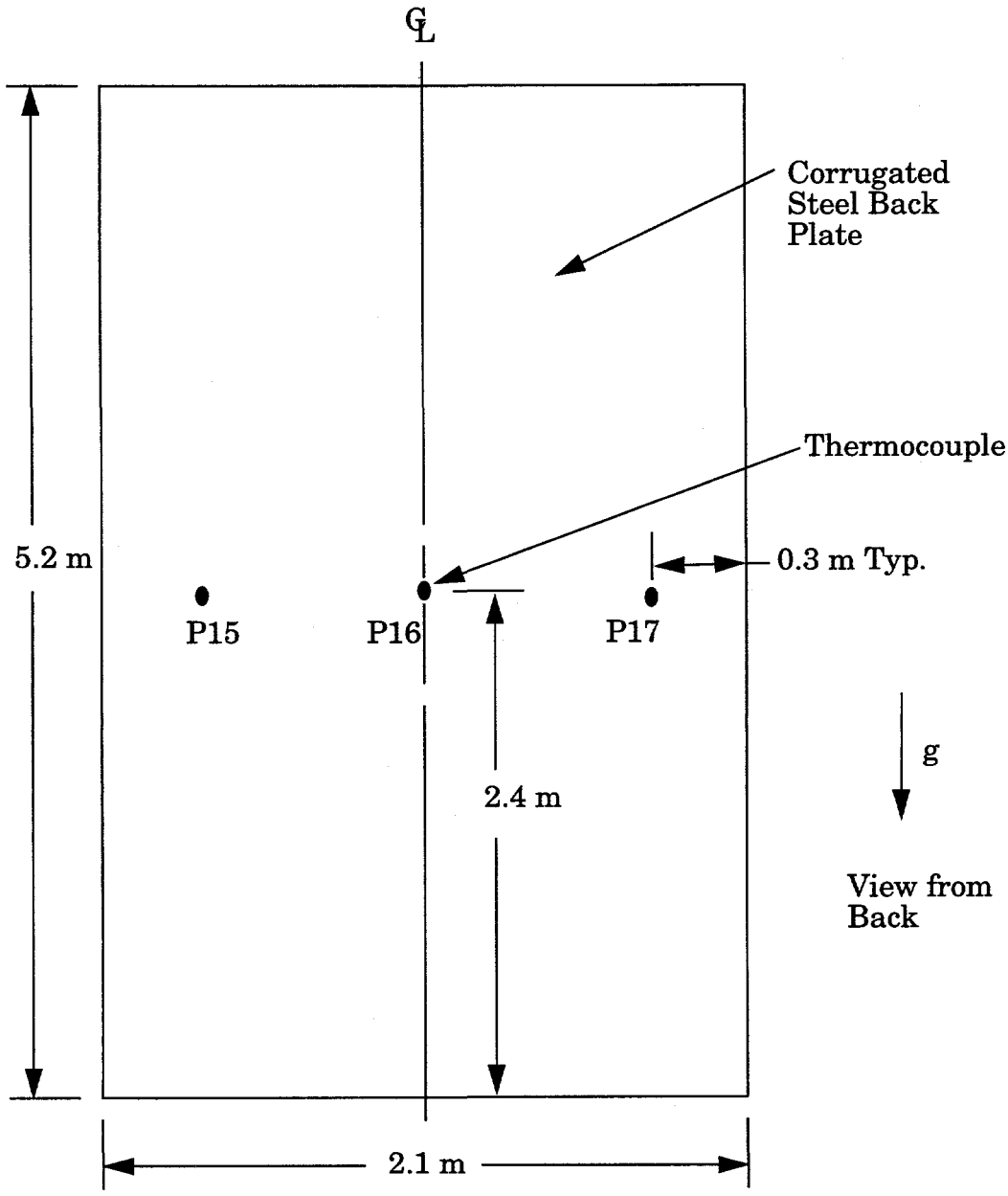

Figure 2.4 Thermocouple Locations on Corrugated Steel Back Plate

2.3 Fire Environment Instrumentation

Twenty seven "free fire" (i.e. thermocouples which were directly exposed to the flames) Type-K, 0.16 cm diameter sheathed thermocouples and 10 Hemispherical Heat Flux Gauges (HFGs) mounted on three stringer assemblies, as shown in Figure 2.5, were used to monitor the fire environment near the calorimeter.

HFGs use a thin (0.025 cm) flat sensor disk with a thermocouple attached to the interior side. Thermal contact between the sensor disk and the remainder of the gauge is minimized and hence the sensor disk rapidly (limited by the time constant of the attached thermocouple) approaches equilibrium with the fire environment. A high temperature sensor surface reduces the potential for soot deposition due to thermophoresis. A Pyromark™ black coating is applied to the sensor disk to yield a diffuse and gray surface. When convection is negligible, the emissive power of the diffuse, gray sensor surface, in equilibrium with the surroundings, provides a measurement of the incident heat flux. The gauges used in this series include sensor surfaces on both ends to measure the heat flux in two directions. At the time of these experiments, HFGs were still under development. At four locations, gauges which included light (0.025 cm) stainless steel shields, to investigate the potential of reducing the influence of convective heat transfer, were located next to unshielded gauges. Future enhancements of the gauge have resulted in eliminating the use of shields and increasing the sensor diameter from 2.5 cm to 5 cm to reduce heat loss to the gauge body. Production versions of the HFGs are presently constructed according to SNL drawing R45066. A detailed description of the HFG, including calibration data and general heat flux measurement considerations, is also available [5].

The stringer assemblies were constructed at SNL and shipped to NAWCWPNS where they were mounted on three water-filled towers as shown in Figure 2.5. Figure 2.5 also shows the thermocouple labeling scheme. To support the instrumentation stringers, "J-shaped" hangers were welded to the towers. Figure 2.6 shows the stringer dimensions and the tower mounting technique. Stringers were located at elevations of 1.2 m, 2.4 m, and 3.6 m from the horizontal plane formed by the bottom of the calorimeter plate. The stringers were placed so that the axis of the stringer is normal to the face of the calorimeter plate, and the nearest point on the stringer is 25 cm from the face of the plate, as shown in Figure 2.5. All thermocouple leads for the stringer assemblies were secured to, and routed along, the center tower. All towers and thermocouple leads were insulated with 2.54 cm thick, ceramic fiber blanket for protection against the fire environment. A photo of the stringer assemblies positioned on the towers as received at NAWCWPNS (i.e. with thermocouple leads packaged and gauge faces uncoated) which shows the shielded and unshielded gauges is given in Figure 2.7.

To characterize the fire environment at a distance from the calorimeter, an assembly of water-cooled, insulated poles forming two thermocouple arrays was located

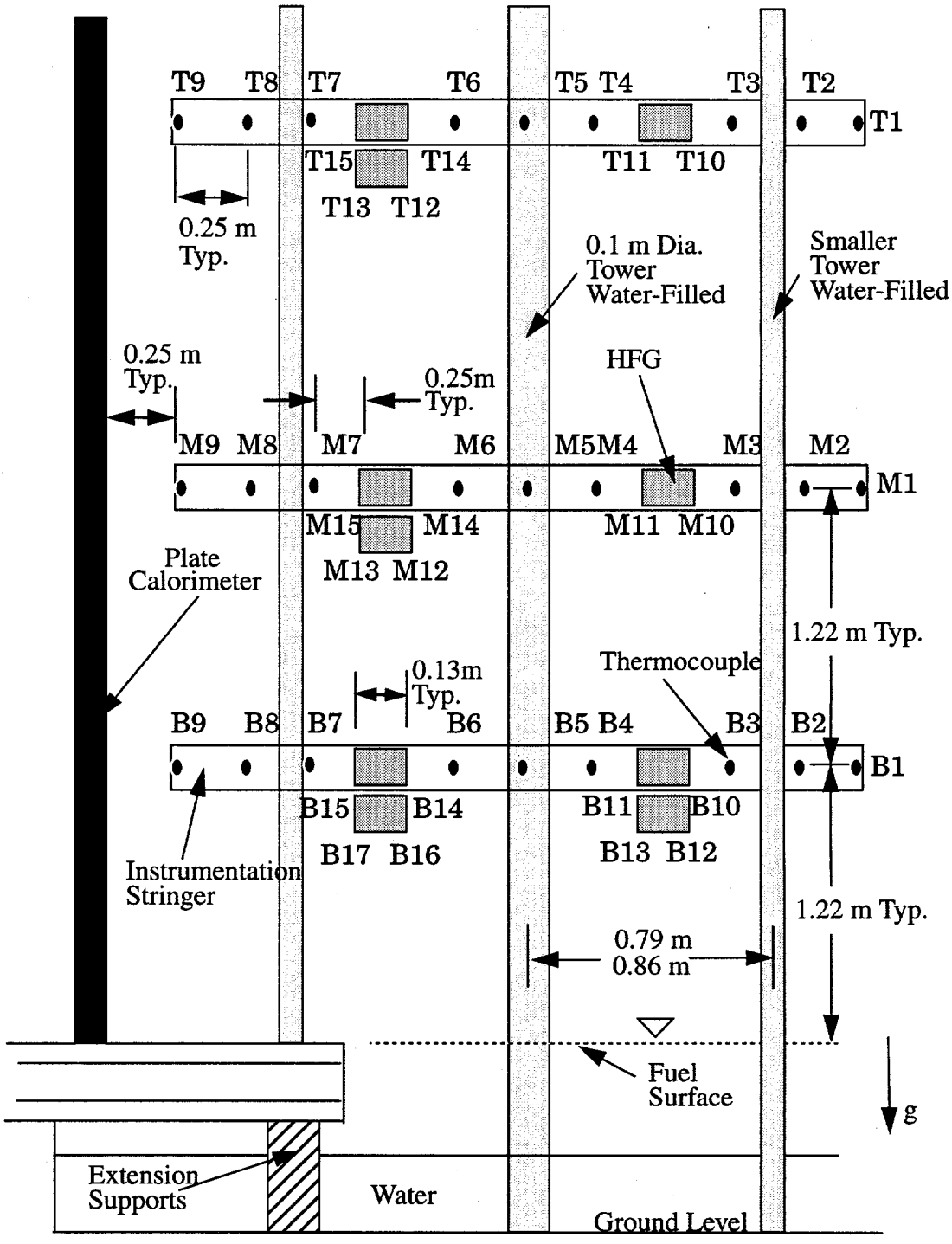

Figure 2.5 Instrumentation Stringer Layout

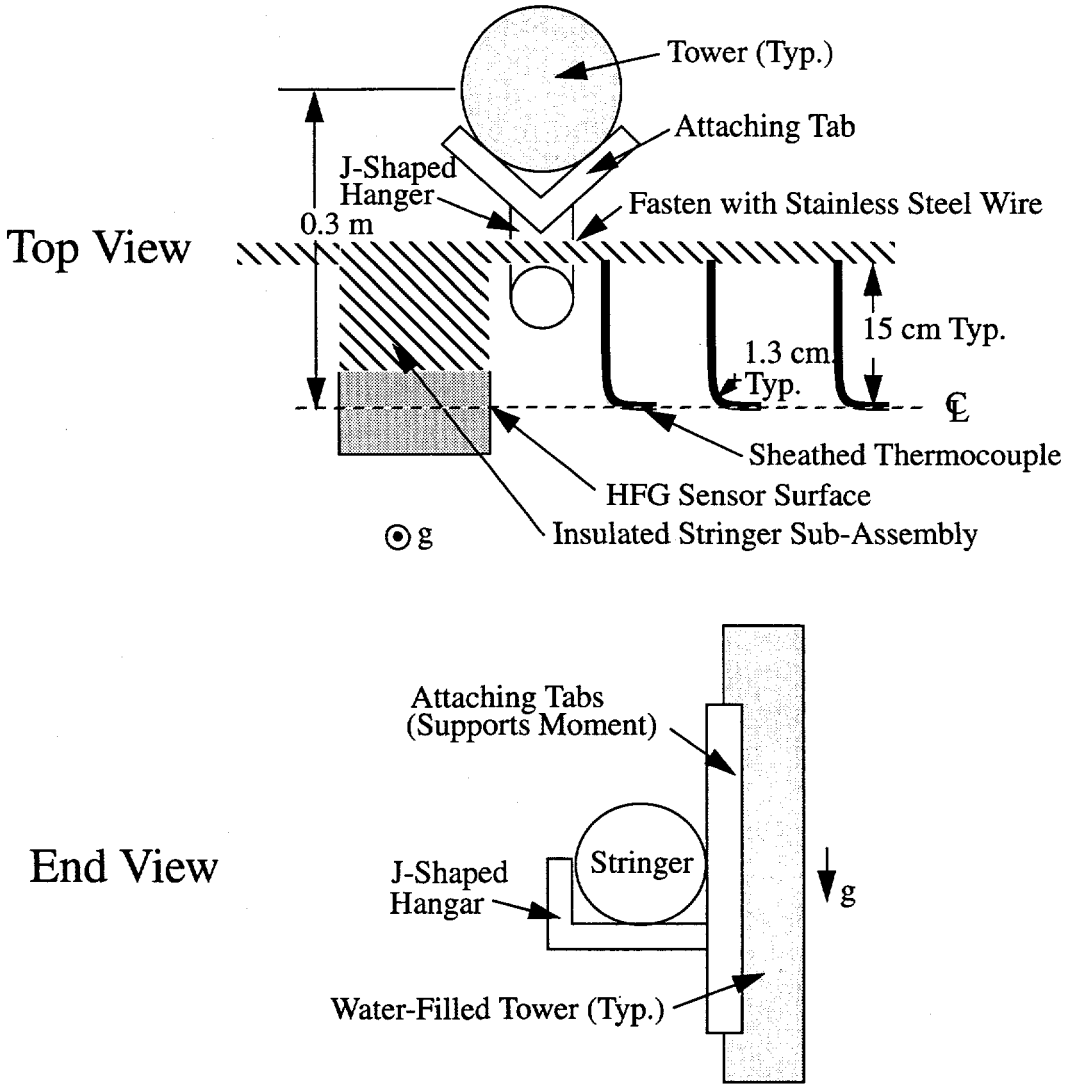

Figure 2.6 Typical Stringer Dimensions and Mounting

within the fuel pool along a line from south to north. The arrays extended from the pool center to slightly beyond the exterior of the test pit. Type K, 0.16 cm bare-junction thermocouples were mounted on the poles such that the junction extended 0.46 m from the surface of the pole. A layout of the thermocouple locations, a thermocouple pole detail, and the pole and thermocouple labeling scheme is given in Figure 2.8.

A photograph of the overall experimental setup, showing the fully-insulated calorimeter and all of the fire environment instrumentation, is given in Figure 2.9.

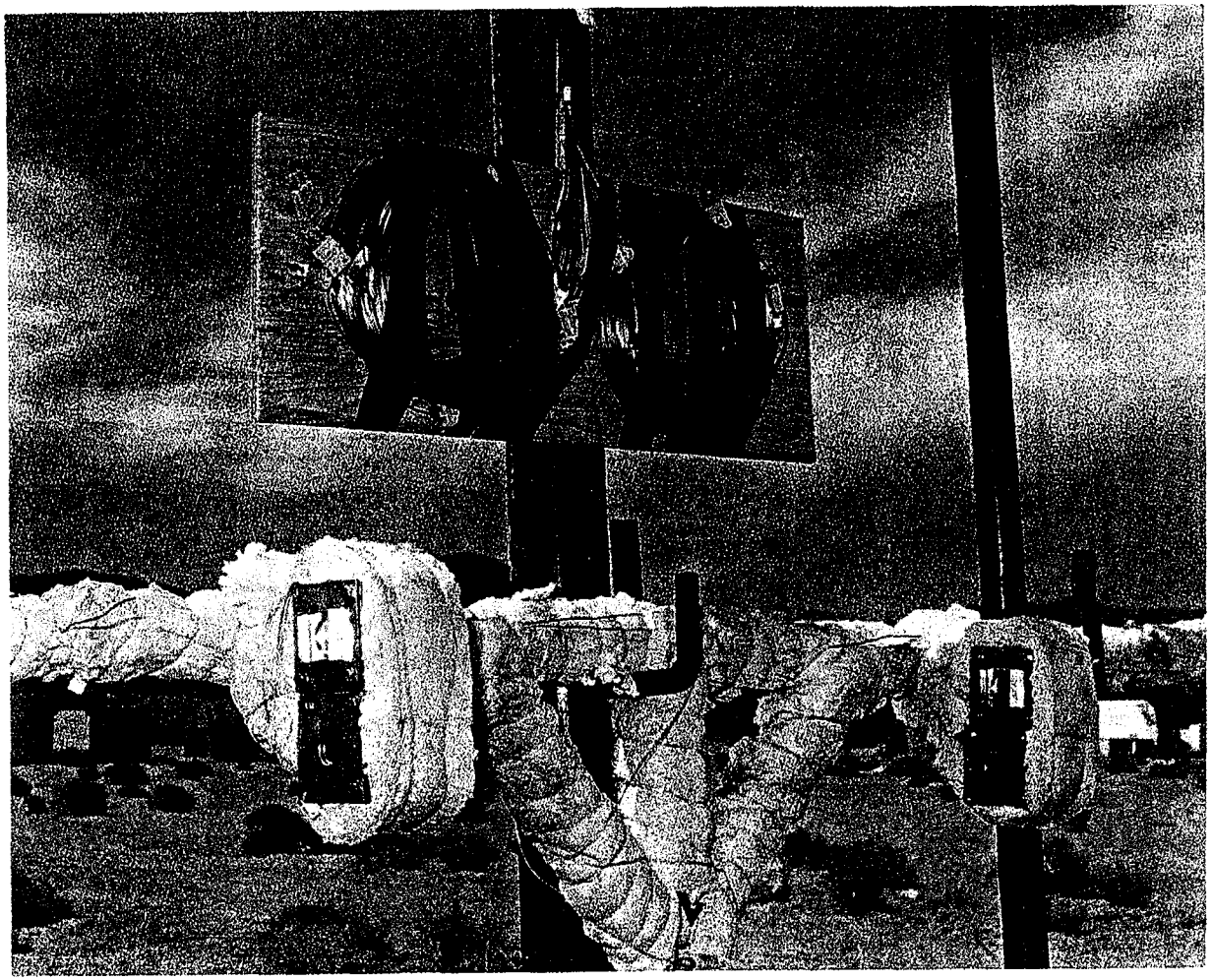

Figure 2.7 Photograph of Stringer Assemblies as Received at NAWCWPNS

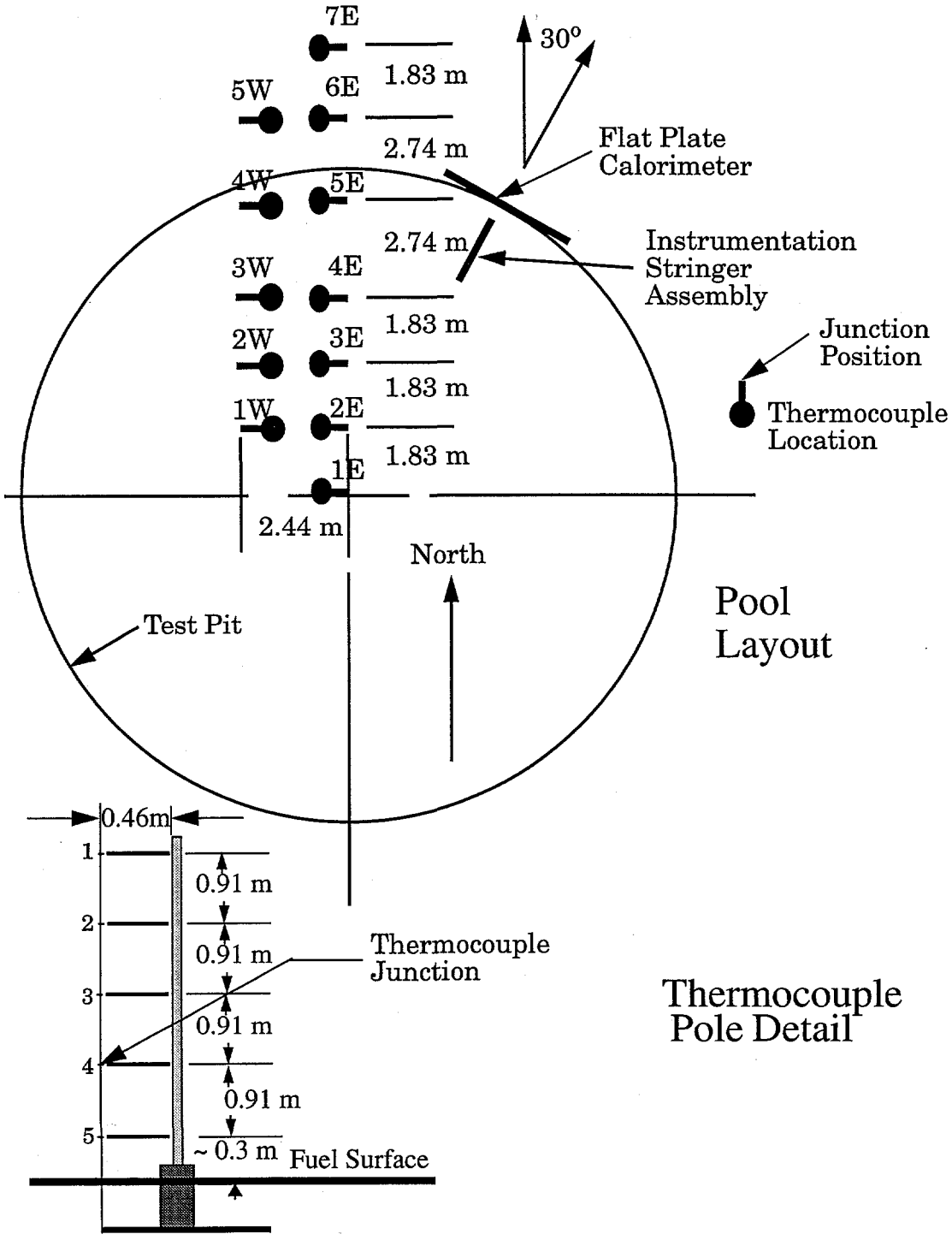

Figure 2.8 Additional Thermocouple Measurements Within Fire

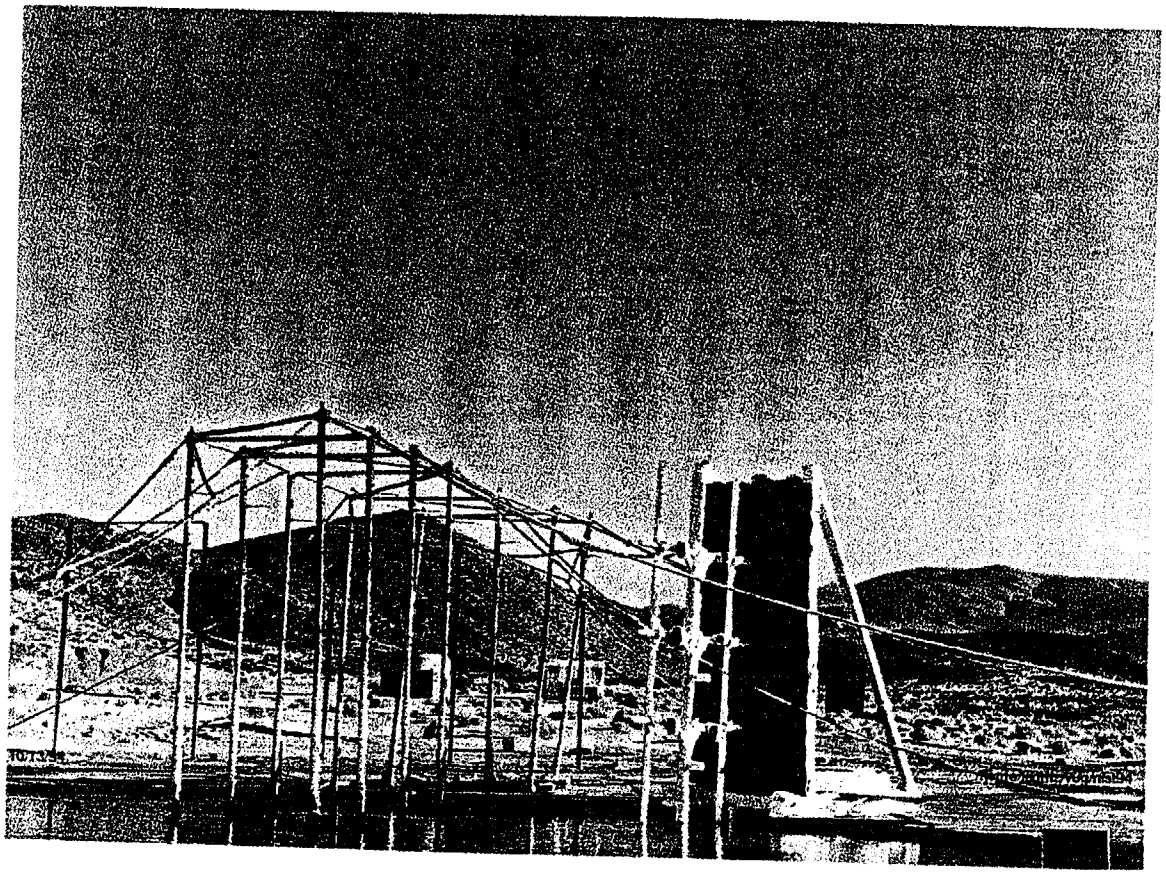

Figure 2.9 Photograph of Overall Experimental Setup

2.4 Wind Condition Instrumentation

Wind speed and direction measurements were performed using a vane-type gauge located 5.5 m from the ground surface and 12.2 m from the south edge of the pool. The gauge was calibrated within the stated accuracy of the instrument.

2.5 Data Acquisition

Type-K thermocouple data were acquired for a total of 134 channels: 20 HFG channels, 27 free fire thermocouple channels from the array adjacent to the calorimeter, 70 free fire thermocouple channels from the additional two thermocouple arrays, and 17 calorimeter channels. All channels were tested immediately prior to the fire experiment. Data was sampled simultaneously for all channels at a rate of 1 sample per second over a period of time beginning approximately 2 minutes (+/- 1min) prior to ignition of the fire and continuing until 2 minutes (+/- 1min) after all of the fuel was consumed.

3. Experimental Results

3.1 Overview of Experiments

Experiments were performed on 8/12/93 (Exp. 1), 9/14/93 (Exp. 2), and 9/16/93 (Exp. 3). Results presented here include a general description of the experiments, wind measurements performed during the experiments, average fuel consumption rates, the identification of periods of quasi-steady state behavior, and temperature and heat flux results during those periods. A discussion of relevant phenomena is also included. Observations from the video record are included in the discussion of the results. Copies of the video record for these experiments, and the raw numerical data, are available from the primary author. The numerical data have also been entered in the Fire Data Management System (FDMS), an international database of fire experiment results.

3.2 Wind Conditions

Wind speed and direction measurements are provided in Figures 3.1, 3.2, and 3.3 for experiments 1, 2 and 3, respectively. Wind directions are specified in terms of the direction of the wind vector where south is zero degrees and the clockwise direction is positive. A wind direction of 180^{o} from south is hence from the south and towards the north.

As shown in Figure 3.1, wind speeds were initially very low (i.e. conditions were essentially calm) during experiment 1. Approximately 400 s after ignition, a gust of wind over 2.2 m/s (5 MPH) was measured. Winds then became reasonably steady at a speed of near 1.1 m/s (2.5 MPH). Measured wind directions tended to oscillate between 180^{o} and 270^{o} from south, with isolated sudden changes, during this experiment.

Significantly higher wind speeds were measured during experiment 2 as shown in Figure 3.2. Winds were initially above 2.2 m/s (5 MPH) but decreased during the experiment to speeds below 0.9 m/s (2 MPH). Some anomalies can be seen in the data presented in Figure 3.2. From the time of ignition until 600s into the experiment, the wind speed data tend to "fall out" by suddenly dropping to less than 0.5 m/s (1 MPH) and then suddenly increasing back to speeds over 1.8 m/s (4 MPH). An instrumentation malfunction is the suspected cause of this intermittent loss of the signal from the gauge. Evidence of this malfunction does not appear later in the experiment. Following this experiment, the instrument was refurbished in hopes of eliminating future anomalies. Winds were towards the north early in the experiment but quickly shifted to fluctuating directions between 90^{o} and 120^{o} from the south where they remained reasonably stable for the remainder of the experiment.

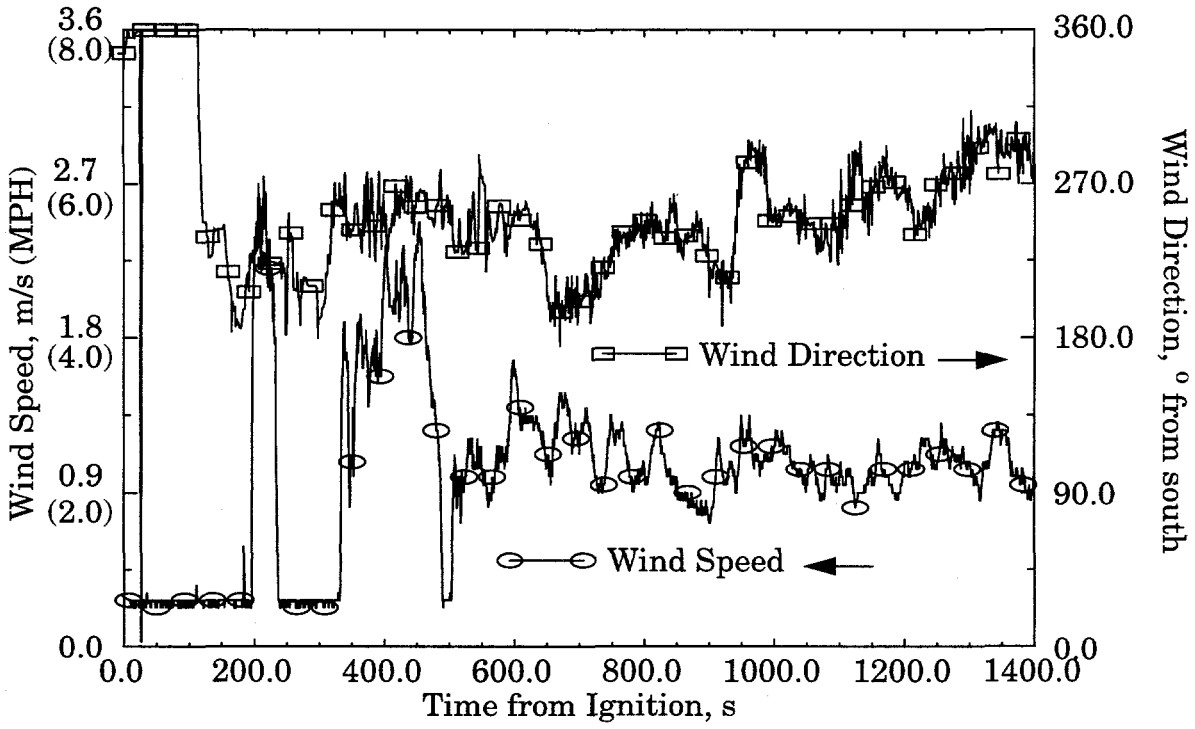

Figure 3.1 Wind Speed and Direction - Exp. 1

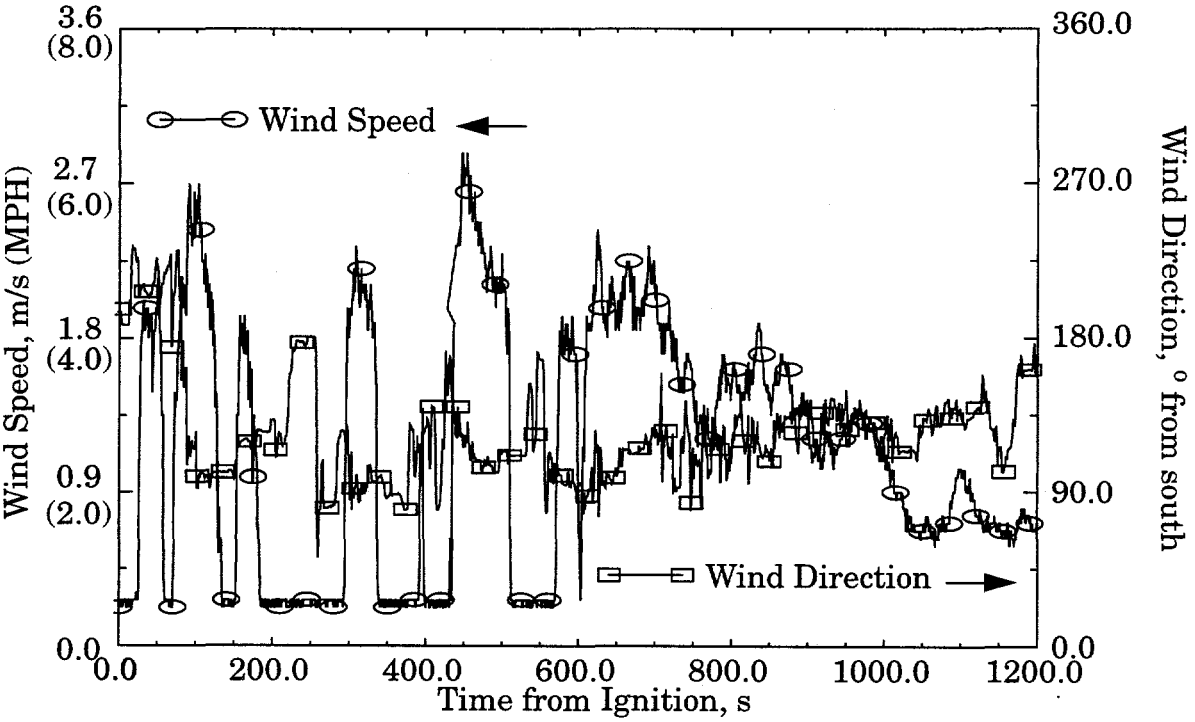

Figure 3.2 Wind Speed and Direction - Exp. 2
(Sudden Drop in Speed due to Suspected Gauge Malfunction)

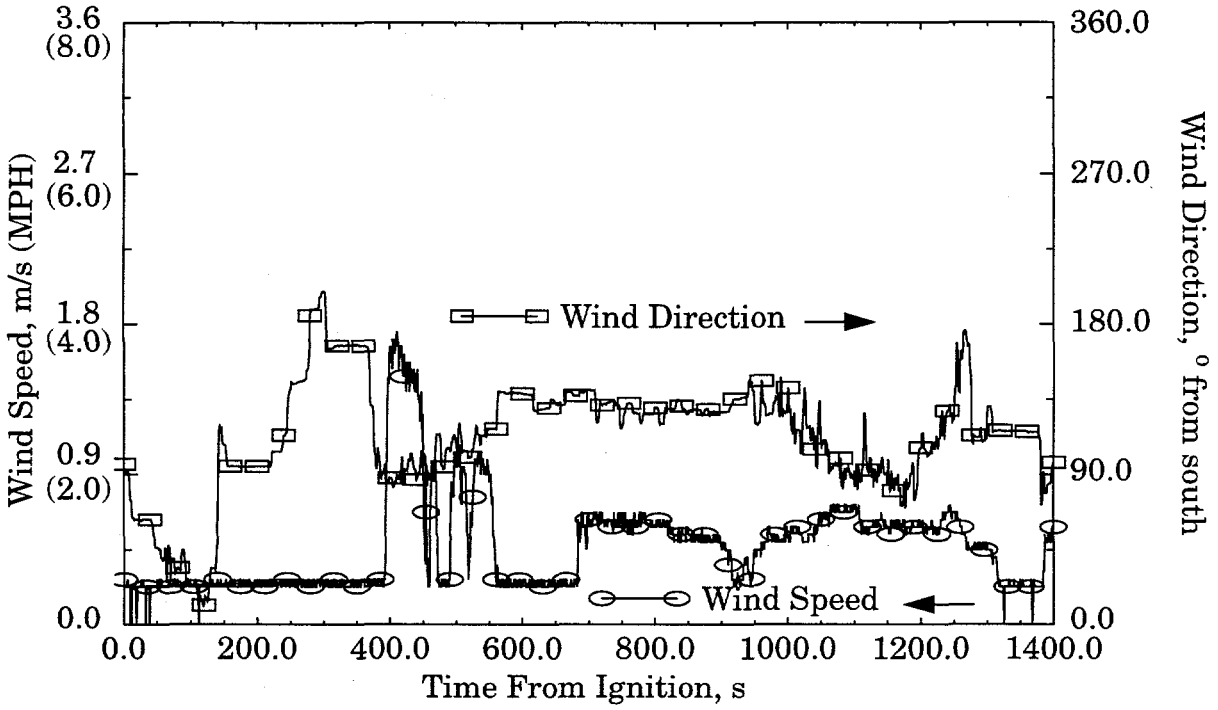

Figure 3.3 Wind Speed and Direction - Exp. 3

With the exception of a 1.8 m/s (4 MPH) gust 400 s into the experiment and some low (~ 0.5 m/s (1 MPH)) winds later in the experiment, conditions during experiment 3 were essentially calm. The data in Figure 3.3 show a wind speed of approximately 0.2 m/s (0.5 MPH) with occasional spikes down to 0. This trend is attributable to the resolution and response of the gauge. Wind speeds less than 0.2 m/s (0.5 MPH) can not be resolved by the instrument. Occasional drops to 0 are due to vane motion in the opposite direction of normal rotation. Wind direction has limited meaning for this experiment due to the small magnitude of the wind vector.

3.3 Average Fuel Consumption Rate

Thermocouple temperature data were investigated to determine the duration of the fire and hence allow the average fuel consumption rate to be deduced. For experiment 1, full burning (as illustrated by thermocouple temperatures greater than 1000 K and therefore representative of flame cover) at all elevations was observed at the center of the fuel pool 21 s after ignition. The period of full burning ended 1280 s after ignition and there was no evidence of burning 1300 s after ignition. For this experiment, the same period of full burning was observed at the north end of the fuel pool. As shown in Figure 3.1, the winds were primarily towards the north near the

end of the experiment. Fuel swept towards the north end of the pool by the wind continued to burn in the form of small flamelets up to 1311 s after ignition.

During experiment 2, full burning occurred at elevations up to 0.91 m at the pool center and north end 12 s and 18 s after ignition, respectively. Full burning at all elevations occurred between 39 s and 1104 s at the pool center and between 56 s and 1080 s at the north end of the pool. All burning ended at the pool center 1145 s after ignition and at the north end 1155 s after ignition. The differences in the rate and positions in which full burning occurred in experiment 1 and experiment 2 are attributable to the differences in wind speed at the beginning of the two experiments. The higher wind speeds during experiment 2 initiated burning earlier at the lower elevations, but greater time was required to reach full burning at all elevations due to advection of the vaporized fuel by the wind.

Full burning was observed at the center of the pool 14 s after ignition during experiment 3. Significantly longer times were required for full burning to be obtained at the north end of the pool. Thermocouple temperatures typical of flame exposure were measured 0.3 m above the pool at the north end 30 s after ignition. A time of 81 s was required to establish burning at all elevations. The cause of the delay in burning at the north end is not clear from the available data. Full burning ended at 1220 s and all burning ended 1300 s after ignition at both locations.

The preceding observations can be used to estimate burn time, which, in conjunction with the volume of fuel consumed and the density of the fuel, provides an estimate of the average fuel mass consumption rate. For these purposes, the minimum burn time is defined as the elapsed time where full burning over the entire fuel surface is observed. The maximum burn time is the elapsed time from ignition to complete extinction. To estimate the fuel consumption rate, a nominal burn time is useful. This value is obtained by assuming that the growth and decline in heat flux to the fuel surface (and hence fuel burning rate) is approximately parabolic immediately during flame spread and immediately prior to extinction. Data from measurements of heat flux to the fuel surface [6] tend to support this assumption. The nominal burn time is then defined by approximating the average fuel consumption rate during the time periods of flame spread and flame extinction to be 1/3 of the total average fuel consumption rate (i.e. the integral of a parabolic profile) during full burning. Considerable uncertainty is associated with this approximation, but it represents the best available estimate and a considerable improvement over a linear average between the minimum and maximum burn times.

The volume of fuel consumed, estimates of the burn time, and the corresponding estimates of the average fuel consumption rate are given in Table 3.1. The average fuel consumption rate as a function of the average wind speed is shown in Figure 3.4. Despite the uncertainty inherent in the fuel consumption rate estimates, (the maximum and minimum values in Table 3.1 are shown in the form of error bars in Figure

3.4) it is evident that the lowest estimate of the burn rate is significantly higher for the experiment performed during predominantly high wind conditions (Exp. 2) than the upper estimate of the burn rate for the experiment performed when low winds prevailed (Exp. 3). Significantly larger fuel consumption rates are observed for experiment 2, where the wind speeds were, as shown in Figure 3.2, generally greater than 1.3 m/s. The lowest fuel consumption rate estimate corresponds to the virtually calm conditions which prevailed during experiment 3. This trend is due to two phenomena: 1) enhanced convective mass transfer at the fuel surface, and 2) improved mixing close to the fuel surface which results in improved combustion and hence increased radiative heating of the fuel.

Table 3.1: Burn Time and Average Fuel Consumption Rate

Exp	Volume of Fuel (m^3)	Burn Time (s)			Fuel Consumption Rate (kg/m^2s)[a]		
		Min.	Max.	Nominal	Max.	Min.	Nominal
1	38.55	1259	1310	1276	0.083	0.079	0.081
2	30.28	1024	1255	1101	0.080	0.065	0.074
3	30.28	1139	1300	1192	0.072	0.063	0.069

a. JP4 density = 760 kg/m^3 [7]

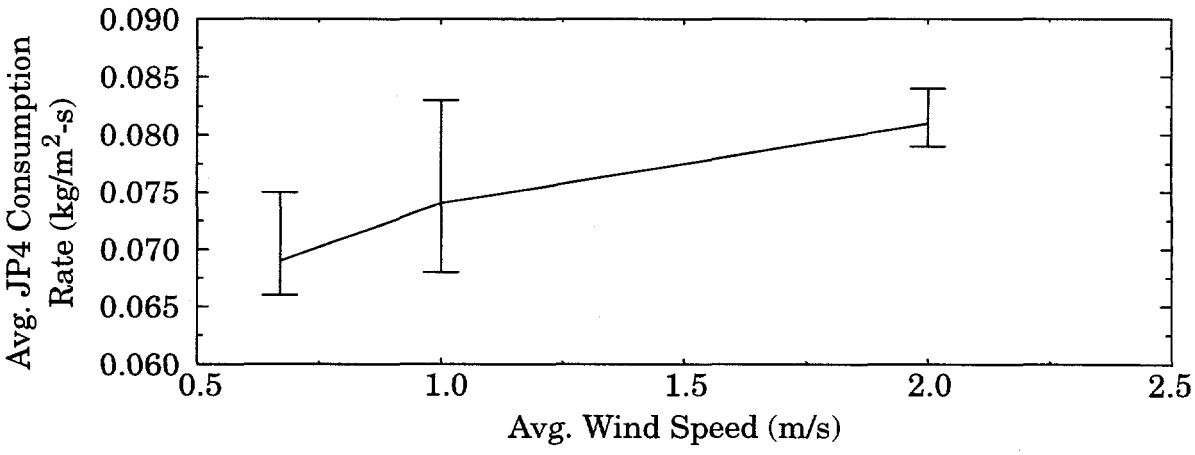

Figure 3.4 Average Fuel Consumption Rate as a Function of Wind Speed

Fuel recession rates ranging from 5 mm/min to 6.5 mm/min (corresponding to the fuel consumption rates given in Table 3.1 and Figure 3.4) observed here are significantly greater than the 4.4 mm/min recession rates acquired in the limited number of experiments included the classical study by Blinov and Khudiakov [8]. Their results show an increase in fuel consumption rate prior to the onset of the fully turbulent regime occurring for pool diameters greater than approximately 1 m. Within the fully turbulent regime, their data shows an essentially constant fuel recession rate (with perhaps a slight downward trend for large diameters) for both high volatility (gasoline) and low volatility (kerosene) fuels. Additional studies are underway to determine the source of the discrepancy.

3.4 Transient Calorimeter Thermal Response

Temperatures measured by thermocouples mounted on the calorimeter and observations regarding the heat fluxes inferred from calorimeter temperature measurements, both as a function of time, are presented in this section. The results illustrate the heating of the calorimeter with elapsed exposure to the fire, and the spatial variations in calorimeter heating observed during different experiments. The changes in the calorimeter temperature (and hence incident heat flux) distribution that occur with time due to changes in wind conditions are also assessed from these data. Further discussion will be focused on spatial characterization of the fire environment under specified wind conditions. The results will therefore be averaged over selected time periods.

3.4.1 Calorimeter Temperature

The transient temperature distribution, as measured by the thermocouples along the center line of the back surface of the calorimeter, is shown for the duration of experiment 1 in Figure 3.5. Transient inverse heat conduction analyses discussed later show a negligible difference between the temperature of the front and rear surfaces of the calorimeter. Accordingly, only the rear surface temperatures are presented here. Due to the surface preparation and thermocouple attachment technique employed, contact resistance between the thermocouple and the calorimeter is neglected and the temperature of the rear surface of the calorimeter is assumed to be given by the thermocouple measurements. The results in Figure 3.5 show an approximately linear increase in the calorimeter temperature with time up to approximately 750 s after ignition. Temperatures increase at a reduced rate towards the end of the fire indicating that the calorimeter is approaching thermal equilibrium with the fire environment. The maximum temperature is observed near the end of the fire (~1300s). As shown in Figure 3.1, winds of approximately 1-2 m/s, in a direction primarily towards the calorimeter, were present during this experiment. The flame

zone was therefore tilted by the wind towards the calorimeter and the calorimeter was engulfed in the flame zone for the majority of the experiment.

An enlarged view for the time period between 450 and 650 s after ignition is shown in Figure 3.6. In general, the temperature decreases with elevation, although the temperature at the lowest point along the centerline (z = 0.61 m) drops to the lowest of the measured temperatures approximately 525 s after ignition. Figure 3.1 shows a reduction in the wind speed at approximately the same time. This reduction in wind speed will result in less tilting of the flame zone. A reduction in the tilt of the flame zone will cause the cold, oxygen-starved flame zone interior near the fuel surface to move towards the center, raising the temperature of the lower portion of the calorimeter located at the edge of the pool. Correlation therefore exists between measured wind speeds and spatial temperature distributions on the calorimeter surface. These results emphasize the influence of wind on the heat flux to an object.

The transient temperature distribution along the centerline of the calorimeter during experiment 2 is shown in Figure 3.7. The highest temperature (~850K) is observed near the bottom of the calorimeter with temperatures decreasing with increasing elevation. A lower maximum temperature is observed in experiment 2 and the trend is opposite from the trend of data acquired during experiment 1 and shown in Figure 3.6. A significantly larger variation in temperature as a function of elevation is also evident in the data from experiment 2. These differences are due to wind

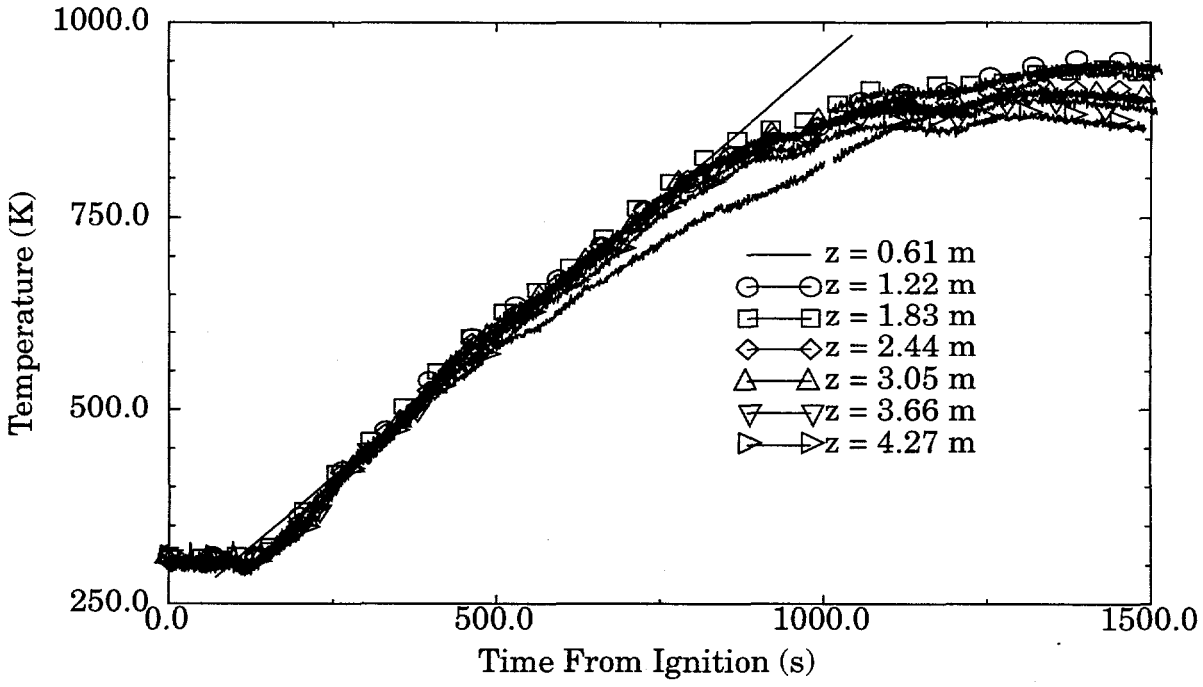

Figure 3.5 Transient Temperature Along Plate Vertical Centerline - Exp. 1

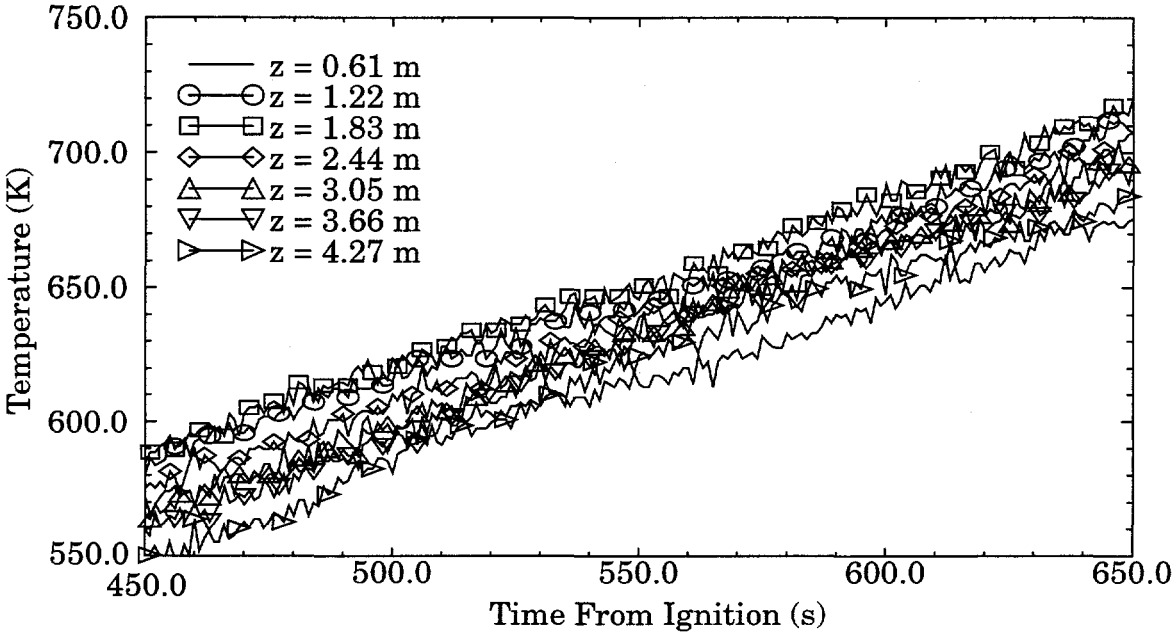

Figure 3.6 Transient Temperature Along Plate Vertical Centerline - Exp. 1, 450-650s

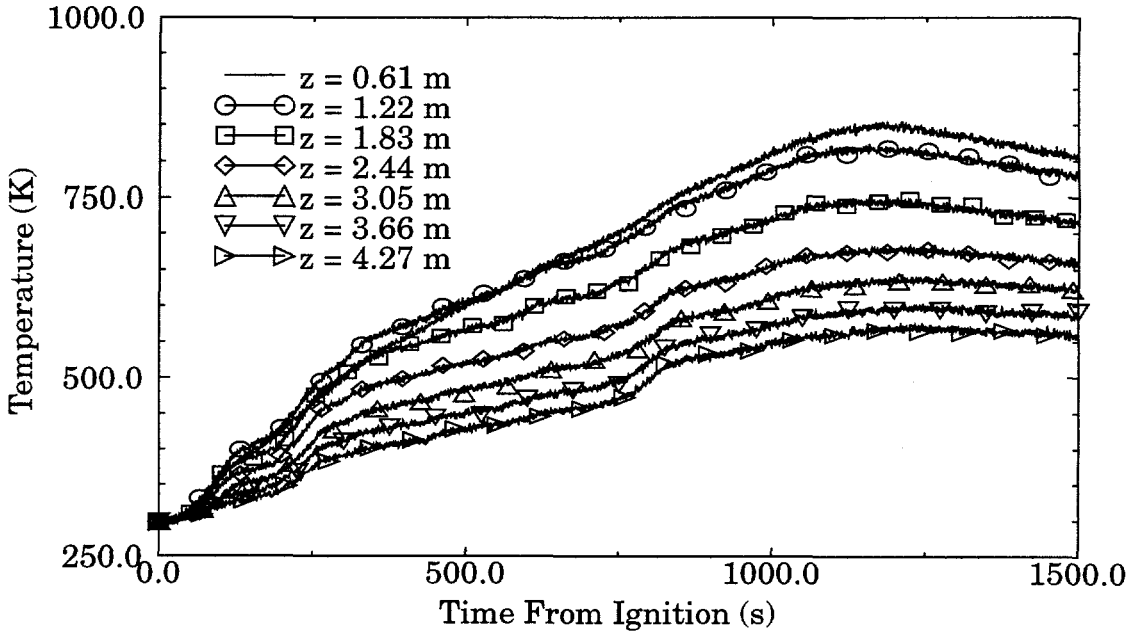

Figure 3.7 Transient Temperature Along Plate Vertical Centerline - Exp. 2

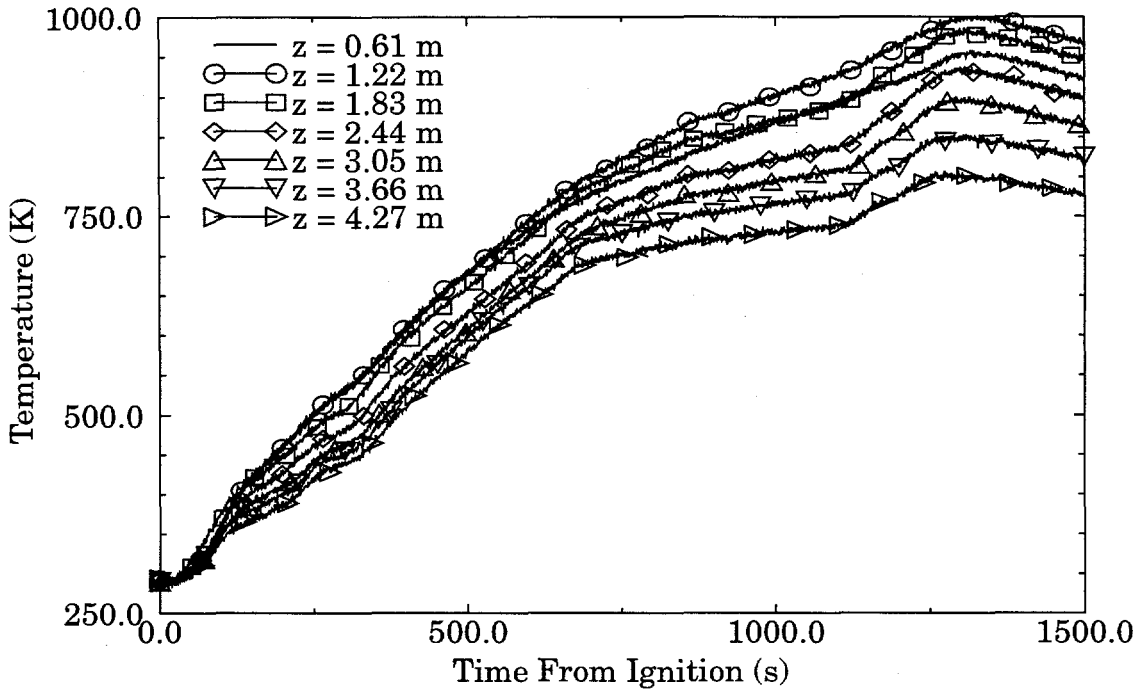

Figure 3.8 Transient Temperature Along Plate Vertical Centerline - Exp. 3

conditions which tend to engulf the calorimeter during experiment 1, and winds which directed the flame zone away from the calorimeter during experiment 2.

Temperatures measured by thermocouples on the back surface of the calorimeter are shown for the duration of experiment 3 in Figure 3.8. In a manner similar to experiment 2, the highest temperature is observed near the bottom of the calorimeter. In comparison with experiment 2 and Figure 3.7, the variation as a function of elevation is significantly less pronounced and the maximum temperature is comparable to those observed during experiment 1 and shown in Figure 3.6. The existence of a change in slope of the calorimeter temperature approximately 700 s after ignition is consistent with the change in wind speed from calm conditions to winds slightly greater than 0.5 m/s shown in Figure 3.3. More rapid, short duration transient changes in wind conditions (such as those observed approximately 400 s after ignition) appear to have little or no effect on the thermal response of the calorimeter due to its thermal mass.

3.4.2 Calorimeter Heat Flux

Using temperature measurements acquired on the back side of the calorimeter, the Sandia One Dimensional Direct and Inverse Thermal Code (SODDIT) [9] was

used to estimate the front surface temperature and the total (radiative and convective), *net absorbed* (i.e. the energy which results in sensible heating of the calorimeter) heat flux. Two models were constructed: 1) a detailed model which performs the inverse calculation using two measured temperatures (the temperature on the back of the calorimeter plate and the temperature on the corrugated steel back plate), and 2) a simplified model which represents a 3.18 cm steel plate, a 6.35 cm layer of ceramic insulation, and an adiabatic back surface. A description of the detailed model, and the comparison of results for the detailed and simplified models, is provided in Appendix B. The simple model was proven to produce the same results as the more detailed model and was therefore applied at all locations to estimate the heat flux on the front surface of the calorimeter. The model parameters used in the simplified model are given in Appendix C.

The assumption of one-dimensional heat transfer invoked to calculate the absorbed heat flux was supported by a maximum plate temperature variation in the horizontal direction (along the centerline) of less than 10 K per 0.3 m (> 729 K to < 738 K) and vertical variations of less than 55 K (> 685 K to < 740 K) per 0.6 m. The front surface temperatures determined by SODDIT are consistently 2-5 K above those measured on the back side of the calorimeter plate and therefore the front surface temperatures were not presented here.

Interpretation and subsequent reduction of the heat flux results is worthy of additional discussion. The heat flux *incident* on the calorimeter (which is the measure of the thermal hazard posed by the fire) is given by the sum of the net absorbed heat flux and the front surface emissive power, assuming that the surface is diffuse and gray, by

$$q_{inc} = \frac{q_{net,absorbed}}{\varepsilon} + \sigma T^4 \qquad \text{(Eqn. 1)}$$

where ε is the emissivity of the front surface. The surface of the calorimeter was coated with flat black pyromark, which is expected to yield an emissivity between 0.85 (for pyromark exposed to higher temperatures) [10] and 1.0 (for surfaces coated with a thin layer of soot). According to Eqn. 1, the difference between the net, absorbed heat flux and the incident heat flux increases nonlinearly with increasing front surface temperature and decreasing emissivity. An example of this difference, using the largest measured temperature (i.e. that observed at the bottom of the calorimeter during experiment 3) is shown in Figure 3.9. The maximum influence of the unknown emissivity on the incident heat flux is approximately 20% and is observed early in the experiment when the surface temperature is low (and hence σT^4 is small). As the calorimeter surface temperature increases (towards the end of the experiment) the difference between the incident heat flux and the net absorbed heat flux becomes more significant and less subject to the influence of the unknown emissivity. The influence of the assumptions that are invoked to obtain incident heat flux

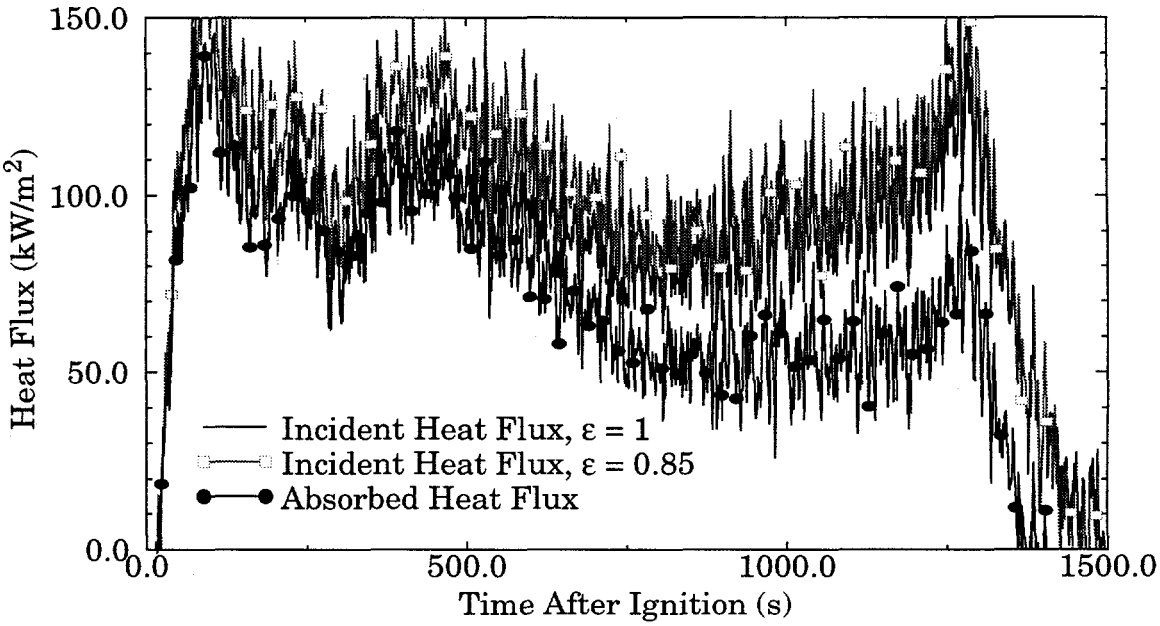

Figure 3.9 Transient Heat Flux Distribution, Z = 0.61 m - Exp. 3

data from absorbed fluxes (in terms of the radiative properties of the surface) therefore depend on the temperature of the calorimeter and hence on the time into the experiment. Reasonable minimum (or maximum) incident heat fluxes over intervals during the experiment can be determined by using the maximum emissivity and the minimum calorimeter surface temperature (or the minimum emissivity and the maximum calorimeter surface temperature). This approach is implemented in the following section.

The complication posed by increasing surface temperature can be minimized by attempting to keep the surface at a constant temperature via active cooling [11] or by using a calorimeter with less thermal mass. Both of these options present challenges for studies of the interaction of large flat surfaces with large fires. Active cooling is limited by cost considerations and surfaces with less thermal mass are subject to excessive warping.

As evident in Figure 3.9, heat flux data deduced from transient thermocouple measurements include large oscillations which appear to be noise. These features are expected since heat flux calculations require evaluating the derivative of the transient temperature data (which amplifies any noise in the signal). It is therefore preferred to either smooth the original data, or to represent the heat fluxes in terms of time-averaged values. The second approach is taken here, where the heat fluxes are averaged over periods of quasi-steady-state behavior.

3.5 Periods of Quasi-Steady-State Behavior

Fire data are characterized by rapid changes in temperature and heat flux due to the interaction of instrumentation such as thermocouples and heat flux gauges with turbulent flame sheets. In order to spatially characterize the fire environment, data are averaged over a period of quasi-steady-state behavior. For each experiment, time periods of quasi-steady-state behavior were identified that follow ignition by a sufficient time for all initial fire transients to stabilize. During these periods, no major changes in the flame geometry were observed in the video record of the experiment, and wind, temperature, and heat flux data oscillated uniformly about a constant mean value. For this experimental series, quasi-steady-state time periods were obtained for wind speeds of 0.45, 1.15, and 2.0 m/s during experiments 3, 1 and 2, respectively. The standard deviation of the wind speed during these periods did not exceed 0.09 m/s. Wind directions during these periods of 0.45, 1.15, and 2.0 m/s wind speeds were 130°, 242°, and 110° from south, respectively. The standard deviation of the wind direction during these periods did not exceed 9.8°. Quasi-steady-state time periods are summarized in Table 3.2. The sections which follow focus on results obtained by averaging data over these time periods.

Table 3.2: Quasi-Steady-State Time Periods

Exp. Number	Time After Ignition, min (s)	Wind Speed, m/s		Wind Direction, °from south	
		Mean	Standard Deviation	Mean	Standard Deviation
1	8.2 - 10.8, (492-648)	1.15	0.09	242	9.8
2	10.1 - 12.1, (606-726)	2.0	0.09	110	7.2
3	7.0 - 9.4, (420-564)	0.45	0.05	130	3.1

3.5.1 Time-Averaged Results, Experiment 1

From a review of the video record, the flame shape and behavior appeared to be relatively stable during the quasi-steady-state time period identified for experiment number 1. The calorimeter and thermocouple array were engulfed for the duration of this time period. Figure 3.10 is a sketch of the general range of the flame shape (flame remained between boundaries 1 and 2) for the time corresponding to this data set.

Time-averaged total incident heat fluxes along the centerline of the calorimeter and temperature contours from time-averaged thermocouple measurements taken

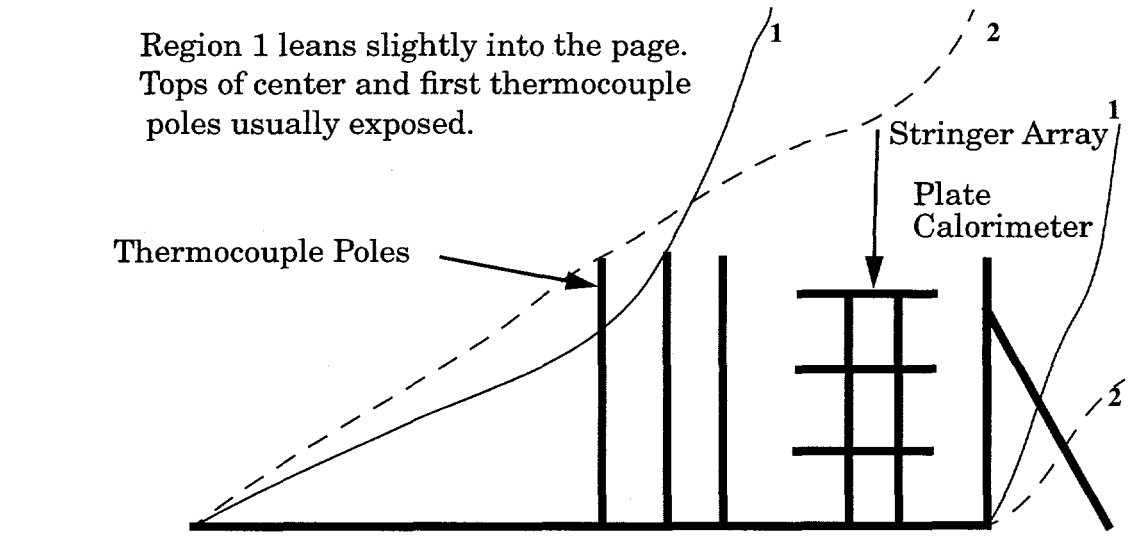

Figure 3.10 Flame Zone Shape, Quasi-Steady-State Time Period - Exp. 1

on the array directly in front of the calorimeter are shown in Figure 3.11. As shown in Chapter 2, replicate thermocouples were installed at three locations. Measurements at these locations differed by a maximum of 5 K and resulted in a maximum precision error of 1.3 kW/m^2, or approximately 1.3%, in the calculated heat flux. Since these data were acquired early in the experiment, the uncertainty associated with the total incident heat flux is dominated by the effect of unknown surface radiative properties. The range of heat flux represented by the error bars (which span approximately +/- 10% of the mean) corresponds to the range of surface emissivities between 0.85 and 1.0.

During the quasi-steady-state time period for this experiment, the surface of the calorimeter increased in temperature from approximately 600 K to 700 K (see Figure 3.6). The uncertainty due to the temperature rise of the plate during the quasi-steady-state time period is less than 5% at every measurement point. Additional uncertainty, including effects of contact resistance between the thermocouple, variations in the thermophysical properties of the material (tabulated values from Incropera and DeWitt [12] were used) are expected to comprise less than 5% and therefore, by comparison to features already identified, can reasonably be neglected.

It should be noted that the thermocouple temperatures measured in the fire and presented here can be, in general, very different from the local media temperature. Sources of these differences, which include participating media radiative heat transfer, thermocouple thermal inertia, and convective heat transfer, have been summa-

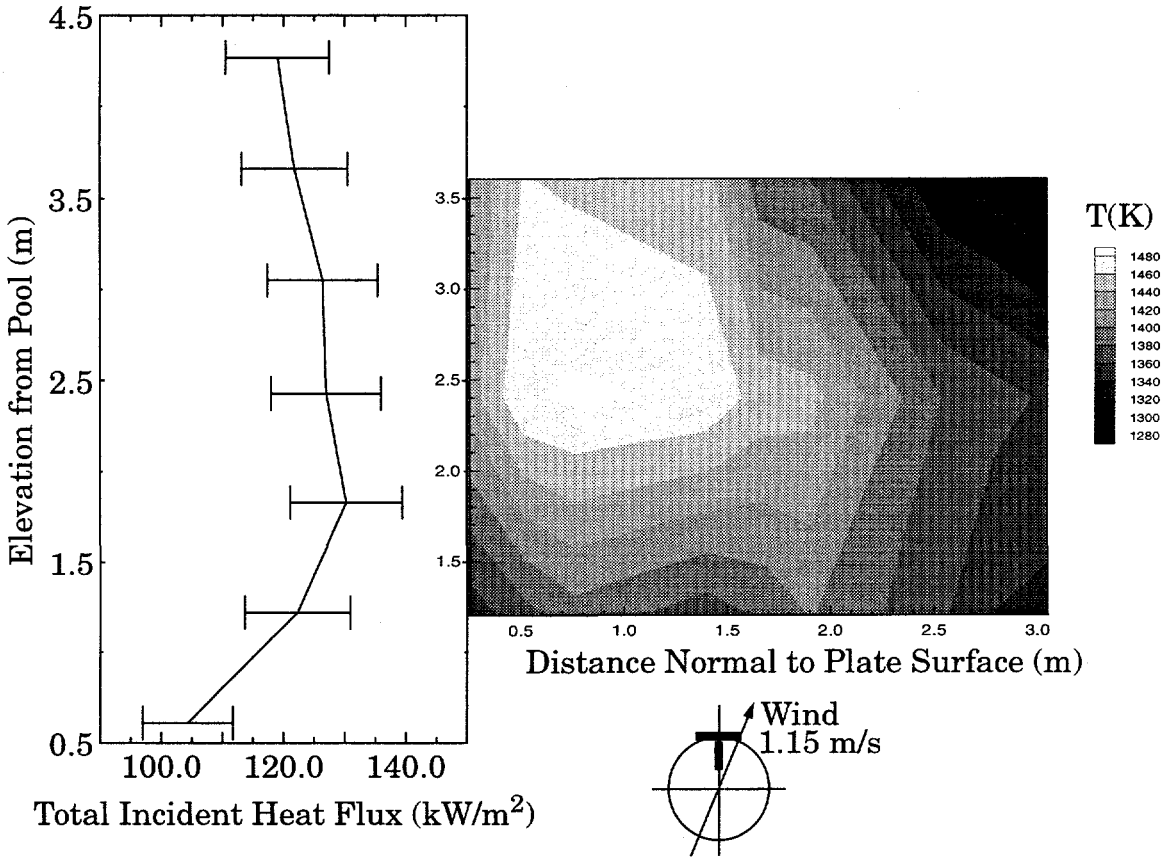

Figure 3.11 Heat Flux on Fully-Engulfed Calorimeter and Fire Thermocouple Temperature - Exp. 1

rized in a previous work [13]. Due to the presence of multiple modes of heat transfer between the thermocouple and the surrounding media, the thermocouple temperatures will tend to be "smoother" than the actual media temperature. Thermocouples located in high temperature regions will generally indicate temperatures lower than the media, and thermocouples in low temperature regions will generally indicate higher temperatures. Very large gradients in temperature which may be present in the fire are therefore not well-represented by thermocouples.

Spatial temperature gradients greater than 100 K/m are evident in the fire thermocouple measurements given in Figure 3.11. Larger gradients are likely to exist. A high (> 1450 K) temperature region is observed approximately 2.5 m from the pool surface and 0.8 m from the surface of the calorimeter. Reduced thermocouple temperatures were measured adjacent to the calorimeter. Lower thermocouple temperatures are expected in this region due to the radiative coupling between fire environments and large, thermally massive objects identified in earlier analyses [14,15]. The presence of a relatively low temperature region away (> 2.5 m) from the calorim-

eter is consistent with the presence of an oxygen-starved region observed in previous data [16].

The magnitude of the temperatures presented in Figure 3.11 are consistent with the temperature of thermocouples exposed to turbulent flame sheets in highly sooting fires. Relative to variations observed near flame zone boundaries, a small overall variation in temperature (200 K) was measured over the area shown in Figure 3.11. At these high temperatures, however, small temperature variations have a high influence on the radiative heat flux to an object due to the fourth power dependence of radiative emission on media temperature. For example, the blackbody emissive power (σT^4) of media at 1280 K (approximately the lower limit of the data shown in Figure 3.11) is approximately 152 kW/m^2, whereas the black body emissive power corresponding to 1480 K (near the upper limit of the data shown in Figure 3.11) is over 270 kW/m^2. This example illustrates the strong influence of the media temperature on radiative heat flux and emphasizes the importance of accurately characterizing the temperature field in order to estimate the resulting heat flux to an object.

Trends observed in calorimeter heat flux data are consistent with the temperature measurements. Figure 3.11 shows an increase in heat flux with elevation up to a maximum of over 125 kW/m^2 at a distance 1.5 to 3.0 m from the pool surface. The magnitude of the incident heat fluxes is slightly lower than expected based on the 150-270 kW/m^2 range of emissive powers corresponding to the thermocouple temperatures. The cause of these reduced fluxes is not well defined. Cold media (including soot and unburned gases) in the immediate (< 25 cm) vicinity of the plate is one potential explanation. It should also be emphasized that the radiative heat flux to the plate is determined by the temperature and radiative property distribution within a hemispherical field. The temperatures presented here were measured in a plane normal to the surface of the plate. Lower temperatures outside the plane of measurement will reduce the heat flux to the plate surface. Although the thermocouples will also be exposed to the same field, the convective component of the heat transfer to the thermocouple will be much larger than the contribution of convection to the heat flux acting on the plate. This difference in radiative/convective partitioning is due to the inverse relationship between the convective heat transfer coefficient and the relevant length scale. Since the diameter of the thermocouple is orders of magnitude smaller than the length along the surface of the plate, convection will tend to drive the thermocouple closer to the temperature of the local media and the thermocouple will therefore be less subject than the plate surface to the influence of the temperature outside the measurement plane.

The horizontal variation of heat flux on the surface of the calorimeter is given in Figure 3.12. At an elevation of 2.4 m, there is less than a 6% variation in the horizontal heat flux distribution. The distribution is skewed slightly towards x<0, due to the component of the wind in the x direction.

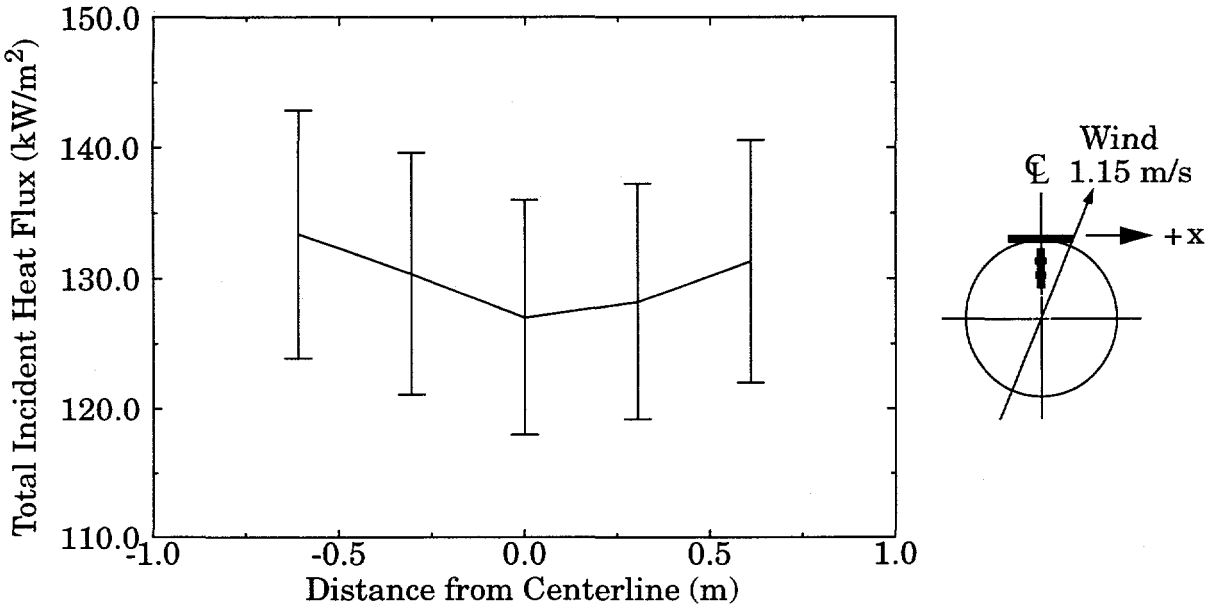

Figure 3.12 Horizontal Variation of Heat Flux at 2.4 m Elevation- Exp. 1

A plot of the hemispherical heat flux distribution, as measured by the HFGs in a plane directly in front of the calorimeter, is given in Figure 3.13. Symbols are used to denote the direction of the measured heat flux. Several trends are evident from inspection of these data. At the bottom level, the heat flux increases with distance from the plate. With increasing elevation, heat fluxes increase near the plate and decrease away (>2.0 m) from the plate. As shown in Figure 2.5, two HFGs were positioned at select locations. The data shown in Figure 3.13 show that the upper gauge consistently measures a higher heat flux than the HFG positioned directly below. This trend is constant with increased mixing, and hence improved combustion efficiency and increased heat release in the vicinity of the upper HFG due to the presence of the lower HFG. Highly mixed, and hence strongly luminescing, regions adjacent to such objects have been recently observed in time-averaged photographs [17]. The lower HFG measurements are therefore more representative of the fire environment. The magnitude of the incident heat fluxes within 1 m of the plate (~170 kW/m^2) given in Figure 3.10 are significantly larger than the magnitude of the incident heat flux to the plate (100 kW/m^2), but are lower than the local emissive power estimates (up to 270 kW/m^2) provided by the thermocouple measurements. As mentioned earlier with regard to the heat flux incident on the plate surface, the convective heat transfer between the flame and a thermocouple is significantly larger than the convective heat transfer between the flame and a flat plate (and hence the sensing surface of the HFG). The HFGs will therefore be more prone to the influence of nearby

regions of lower temperature. The comparatively lower magnitude of the heat flux to the flat plate as compared to the HFGs is consistent with the presence of a highly absorbing layer of cold soot near the plate surface. This effect is expected to be less relevant for the HFGs since the HFG temperature is significantly greater than the temperature of the plate surface and is closer to the temperature of the thermocouples.

As described in Chapter 1, thermocouple temperatures were also obtained along two planes away from the calorimeter. A contour plot of the time-averaged temperature distribution for the plane closest to the calorimeter, along with a schematic of the location of these measurements, is given in Figure 3.14. This figure shows the strong influence of wind on the temperature distribution within the continuous flame zone. The hottest region is located near the edge of the fuel pool (4 to 9 m from the pool center) at an elevation of 1 to 3 m. Temperatures within this region exceed 1300 K. Lower temperatures (1250 K) are observed at the center of the pool extend-

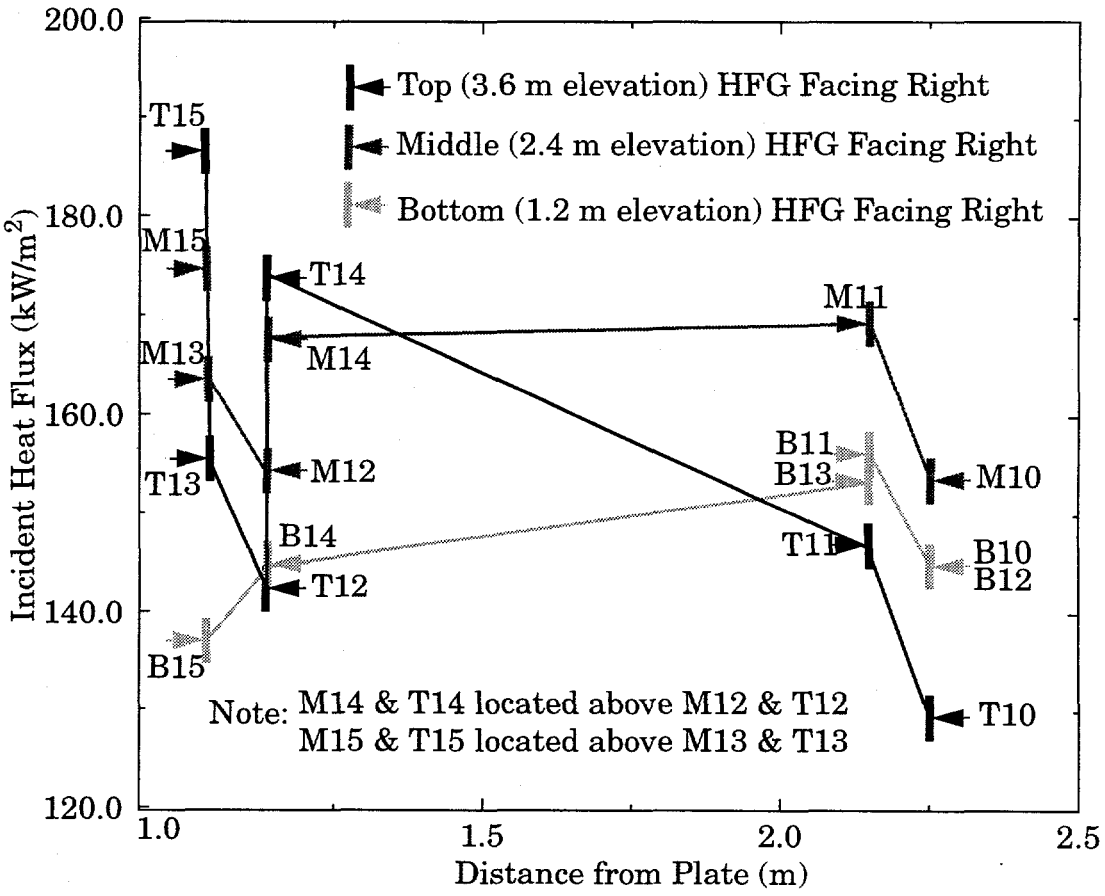

Figure 3.13 Hemispherical Heat Flux Distribution - Exp. 1

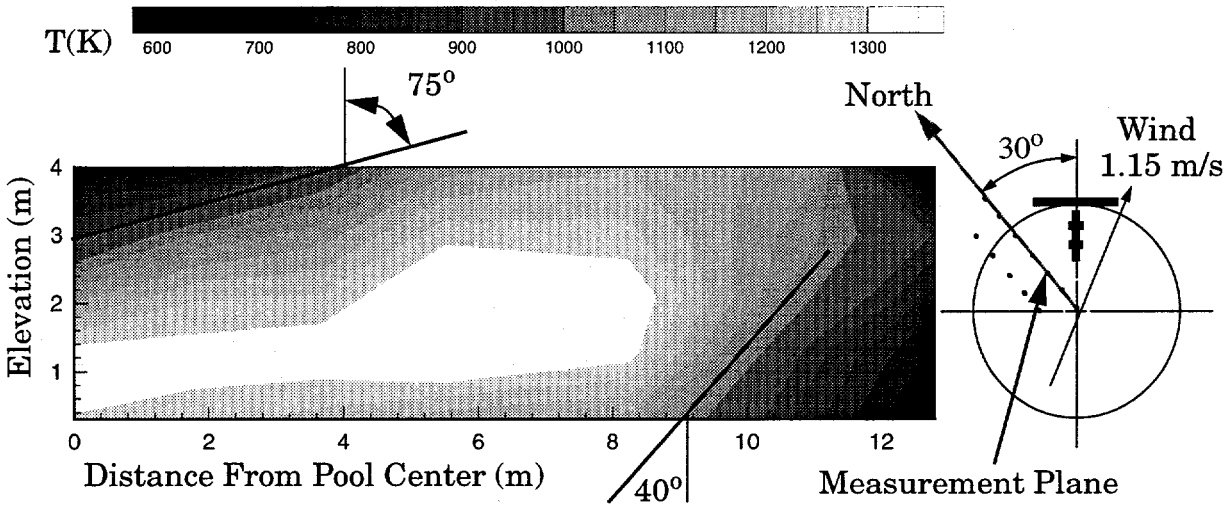

Figure 3.14 Fire Thermocouple Temperature Distribution, Plane Through Pool Center - Exp. 1

ing from the pool surface to an elevation of approximately 1.4 m. A reduction in temperature to less than 750 K occurs with increasing elevation from 1.4 m to 4.0 m.

The magnitude of the wind component along the direction of the plane of thermocouple poles is approximately 0.54 m/s. According to the standard practice [4], a 0.54 m/s wind should not significantly tilt the flame zone produced by a 20 m JP8 pool fire. Figure 3.14 shows that the center of the flame zone (i.e. the region with the highest thermocouple temperature) is significantly displaced along the direction of the wind. The flame zone within this plane, however, is not redirected by a single tilt angle due to the wind. As seen in Figure 3.14, the isotherms form a 75° angle from the normal on the windward side of the plane, whereas the isotherms on the leeward side of the flame zone form a significantly smaller angle of 40° from the vertical. This profile is typical of wind-induced flame zone shapes due to the increased horizontal momentum imparted on the windward side of the flame zone. Buoyancy-induced velocities dominate the influence of the wind on the leeward side. Due to the increase in temperature with elevation from the pool surface, the magnitude of the buoyancy-induced velocity increases with increasing elevation. This trend is clearly shown in Figure 3.14 by the decrease in the angle between the isotherms and the vertical on the leeward side of the flame zone with increasing elevation. Approximately 11 m from the pool center the isotherms become almost vertical at an elevation of 3 m. These results show significant deviation from the symmetric flame volume profile given by standard practice.

A contour plot of the temperature distribution along the plane and farthest from the calorimeter is shown in Figure 3.15. This plane is west of, and parallel to,

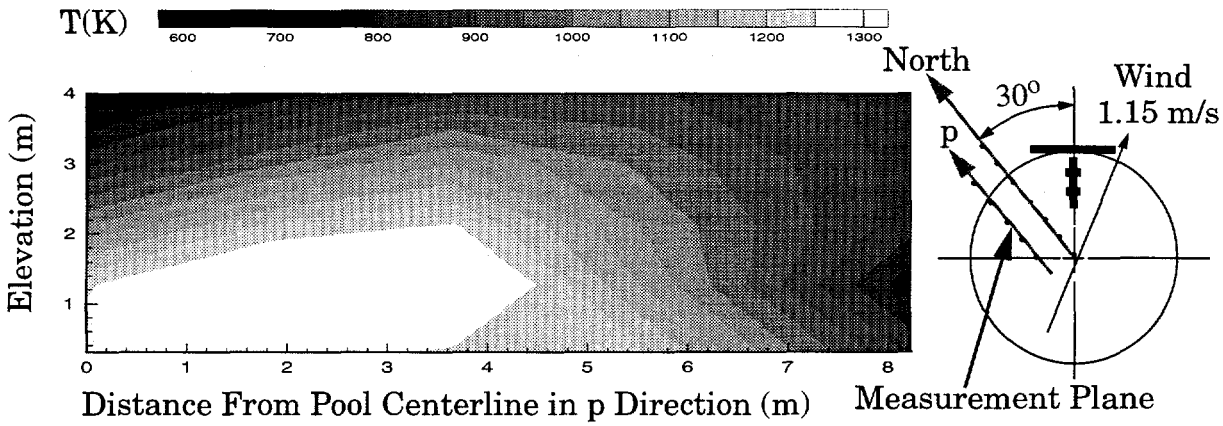

Figure 3.15 Fire Thermocouple Temperature Distribution, Plane West of Pool Center - Exp. 1

the plane represented in Figure 3.14. The two planes are separated by a distance of 2.44 m. The thermocouple temperature distribution shown in Figure 3.15 is representative of a plane closer to the windward edge of the pool. The high temperature region is considerably smaller than shown in Figure 3.14, although the maximum temperature within the two planes is approximately equal. These results emphasize the significant temperature gradients which are present near the edge of the flame zone.

3.5.2 Time-Averaged Results, Experiment 2

During this period, the flame volume was directed away from the flat plate as shown in Figure 3.16. The video record shows stable flame zone behavior with the innermost thermocouples on the bottom stringer to be intermittently engulfed by large-scale turbulent eddies on the exterior of the flame zone. The innermost thermocouples on the top stringer were only occasionally engulfed by the larger eddies.

The vertical distribution of the total incident heat flux at the calorimeter centerline is shown in Figure 3.17. The heat flux decreases with elevation from approximately 75 kW/m^2 near the pool surface to an approximately uniform value of 25 kW/m^2at an elevation of 3.5 to 4.5 m. Since only a very small portion at the bottom of the calorimeter is engulfed, the heat flux from the fire is due to radiative transfer from the flame zone to an object at a "stand-off" distance from the flame zone. In this case, the influence of the object on the entrained air is not sufficient to overcome the momentum transfer due to the wind. The influence of the wind therefore dominates the flame zone shape and the flame zone geometry is generally unaffected by the presence of the object.

When the object does not significantly influence the geometry of the flame zone, the heat transfer from hydrocarbon pool fires to a nearby object is dominated by the emissive power of the outer layer of the flame zone. In general, for highly-sooting hydrocarbons, the majority of this outer layer is covered with a layer of cold black smoke which is thought to be significantly opaque to "block" most of the thermal radiation from the active flame zone. Due to the formation of the large transient vortices which cause the fire to "puff", regions of the smoke layer are regularly displaced by a small (5-20%) area of brightly luminescing flames. Large columnar vortices on the leeward side of the flame zone due to the interaction of the fire with the wind will also produce large luminescing zones which significantly influence the heat flux to a nearby object.

Based on limited data, standard guidelines for hydrocarbon fire hazard estimates [4] provide an approximate value of 20 kW/m^2 for the emissive power of the smoke layer and an approximate value of 150 kW/m^2 for the luminescing regions. The results shown in Figure 3.17 are consistent with the emissive power guidelines for the smoke layer alone. At an elevation of 3.5 to 4.5 m the temperature data show the calorimeter to be approximately 2 m from the flame zone. The view factor from the surface to the exterior of the fire will therefore be nearly unity. Since the larger luminescing regions generally appear very high on the flame zone, or on the leeward side of the flame zone, the heat flux to the calorimeter at an elevation of 3.5 to 4.5 m on the windward side is expected to be primarily from the smoke layer. These data

NOTE: Thermocouple poles engulfed.
Most of stringer array visible
through flame.

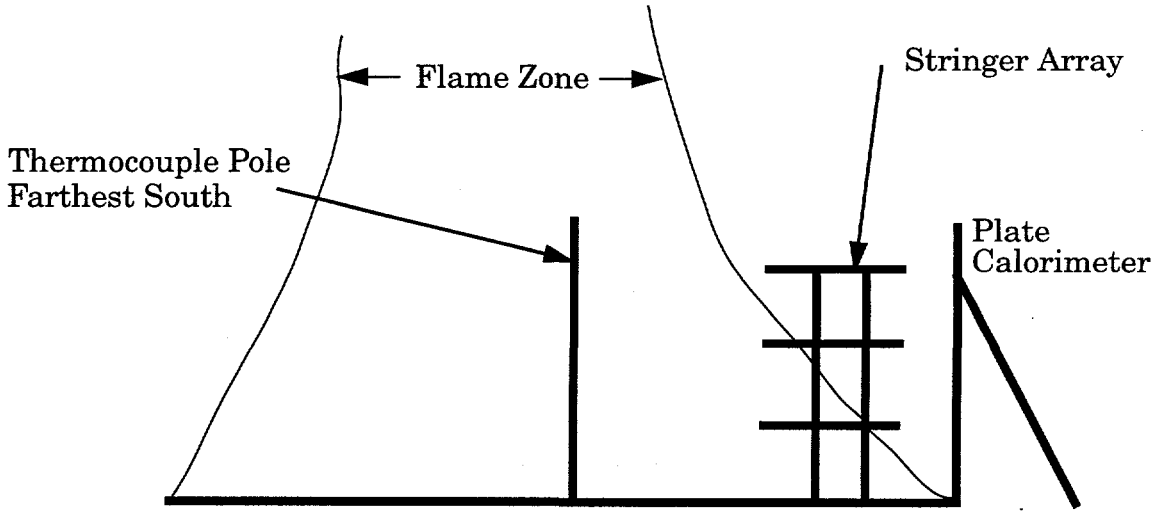

Figure 3.16 Flame Zone Shape, Quasi-Steady-State Time Period - Exp. 2

therefore tend to support previous measurements of the emissive power of the smoke layer.

The thermocouple temperature distribution adjacent to the calorimeter is also shown in Figure 3.17. Temperatures representative of flame exposure (1100-1300 K) are observed at distances of 2.5 to 3 m from the calorimeter surface at an elevation of 1.25 m. The remainder of the temperatures shown in Figure 3.14 are representative of thermocouples which are intermittently engulfed or are being heated by radiation from the fire exterior.

The horizontal heat flux variation is shown in Figure 3.18. Some slight variation in heat flux (a maximum of 8 kW/m^2) is observed. The trend, a higher heat flux on the negative x side of the calorimeter, is consistent with the presence of the wind component in the negative x direction.

Due to the lack of flame cover on the HFGs, data from these measurements are not presented. In these cases, convective effects can induce significant uncertainty into the fidelity of HFG measurements.

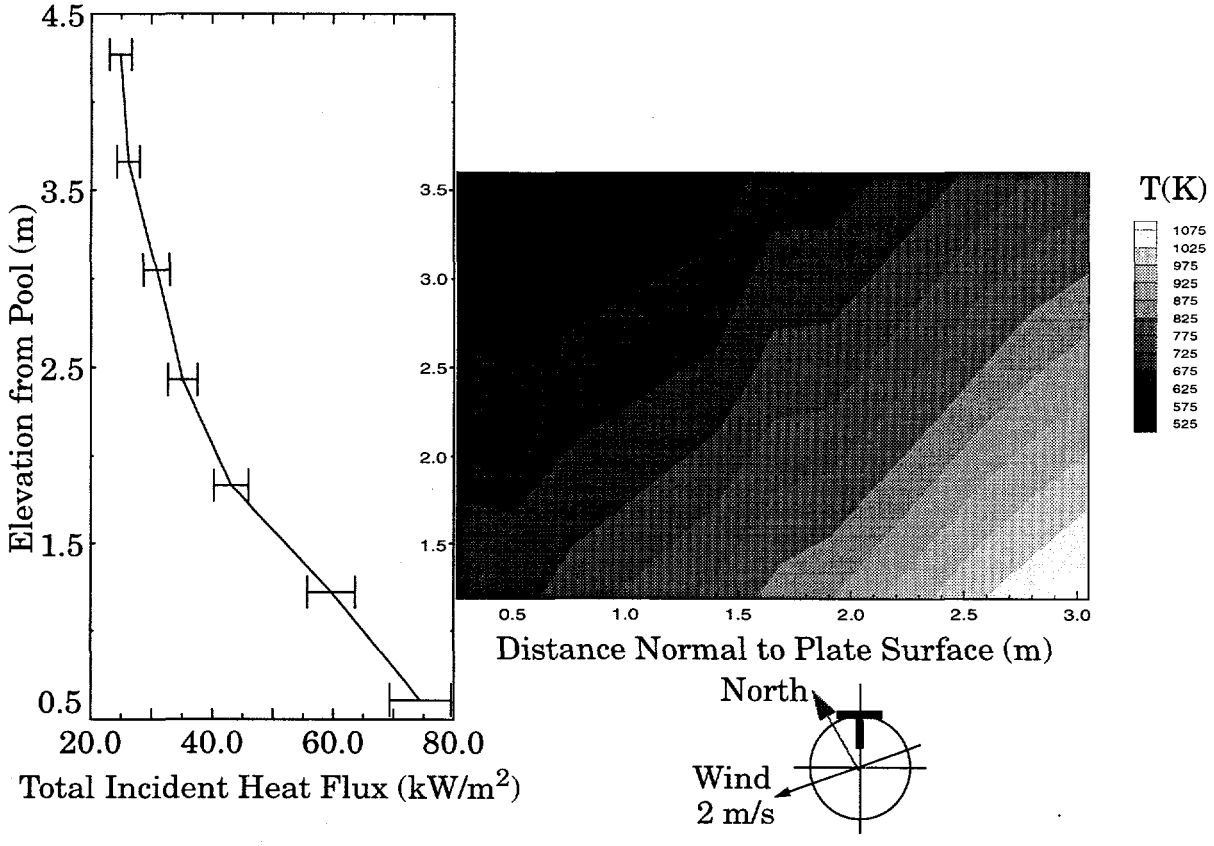

Figure 3.17 Heat Flux on Non-Engulfed Calorimeter and Fire Thermocouple Temperature - Exp. 2

The thermocouple temperature away from the calorimeter is shown in Figure 3.19. The distribution is characterized by temperatures representative of a large, active flame zone (~1300K) which extends from the pool surface to an elevation of approximately 2.5 m at the pool centerline and up to an elevation of nearly 4 m at a distance of 4 m from the pool center. The thermocouple temperature distribution in the region beyond the pool (a distance greater than 9.45 m from the pool centerline) is characterized by almost vertical contour lines near the pool surface. This trend is expected for a measurement plane almost normal to the direction of the wind. The decrease in temperature with increasing elevation near the centerline, as illustrated by the 60^{o} contour lines, is not expected. Given the direction and magnitude of the wind, one would expect the thermocouple temperatures to become constant near the pool center due to symmetry considerations, or to increase with increasing elevation indicating the presence of an oxygen-starved interior. Further investigation is required to resolve the source of this trend. Given the available data, the cause of this trend is not readily evident given the magnitude of the component of the wind in the direction of the measurement plane. It is possible that the profile is attributable to the complex the flow field induced by the calorimeter and measurement hardware located upwind of this cross section.

A contour of the temperature distribution along the plane farthest from the calorimeter is given in Figure 3.20. The same basic flame zone shape is observed except for the high temperature region which extends up to a greater elevation of 4 m. Since

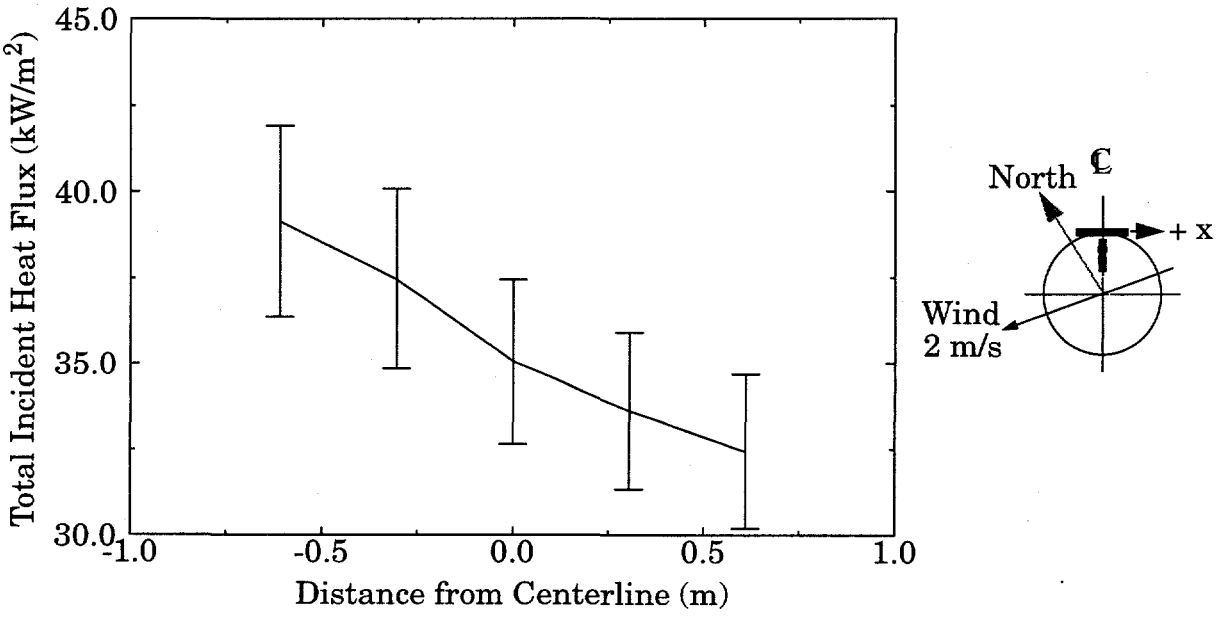

Figure 3.18 Horizontal Variation of Heat Flux at 2.4 m Elevation - Exp. 2

this plane is closer to the leeward side of the pool, a high temperature region indicative of the flame zone extending to a greater elevation is observed in Figure 3.20.

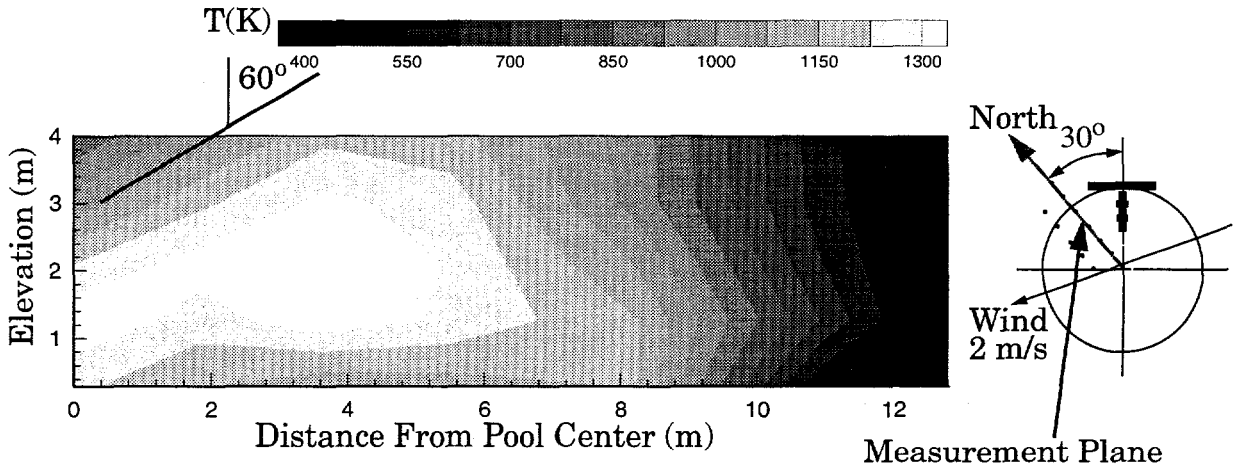

Figure 3.19 Fire Thermocouple Temperature Distribution, Plane Through Pool Center - Exp. 2

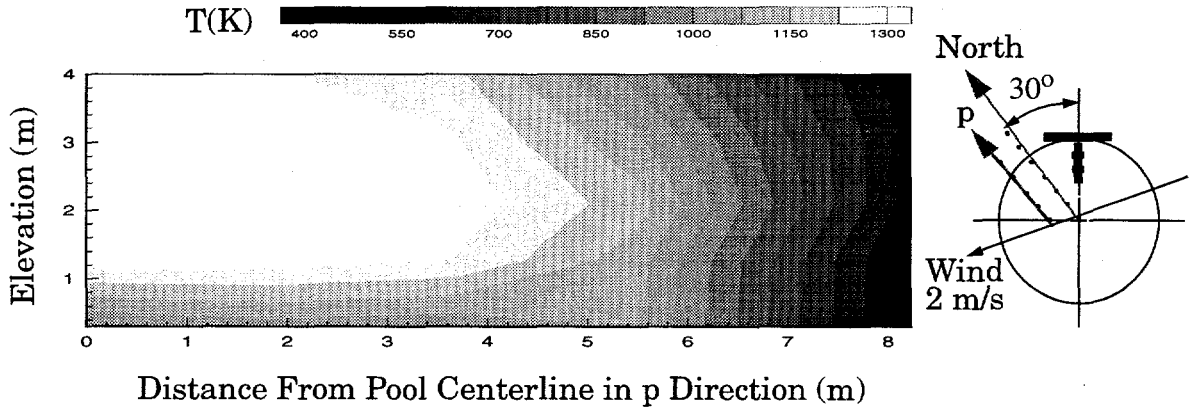

Figure 3.20 Fire Thermocouple Temperature Distribution, Plane West of Pool Center - Exp. 2

3.5.3 Time-Averaged Results, Experiment 3

As given in Table 3.2, very low (0.45 m/s) winds prevailed for the duration of the quasi-steady-state time period identified during experiment 3. Review of the video record for this time period showed extremely stable flame behavior consistent with the negligible wind speed. The main part of the flame, i.e. the primary flame zone, was essentially vertical as shown in Figure 3.21. Except for the periodic puffing, which is well known characteristic of buoyant plumes including pool fires [18], the flame zone shape was stable and did not change throughout the duration of the time period.

During this period, the fire was composed of a large primary flame zone, similar to a fire with no objects under calm wind conditions, and a much smaller secondary flame zone consisting of two standing, counter-rotating vortices formed at the edges of the calorimeter front surface. The formation of the secondary flame zone is due to the presence of the plate. The plate at the edge of the pool restricts the flow of entrained air and produces highly-mixed, and therefore highly combusting, regions at the edges of the front surface of the plate as shown in Section A-A of Figure 3.21. The intensity of these rotational structures is enhanced by baroclinic vorticity. A gap between the flame attached to the plate and the main flame volume was also observed

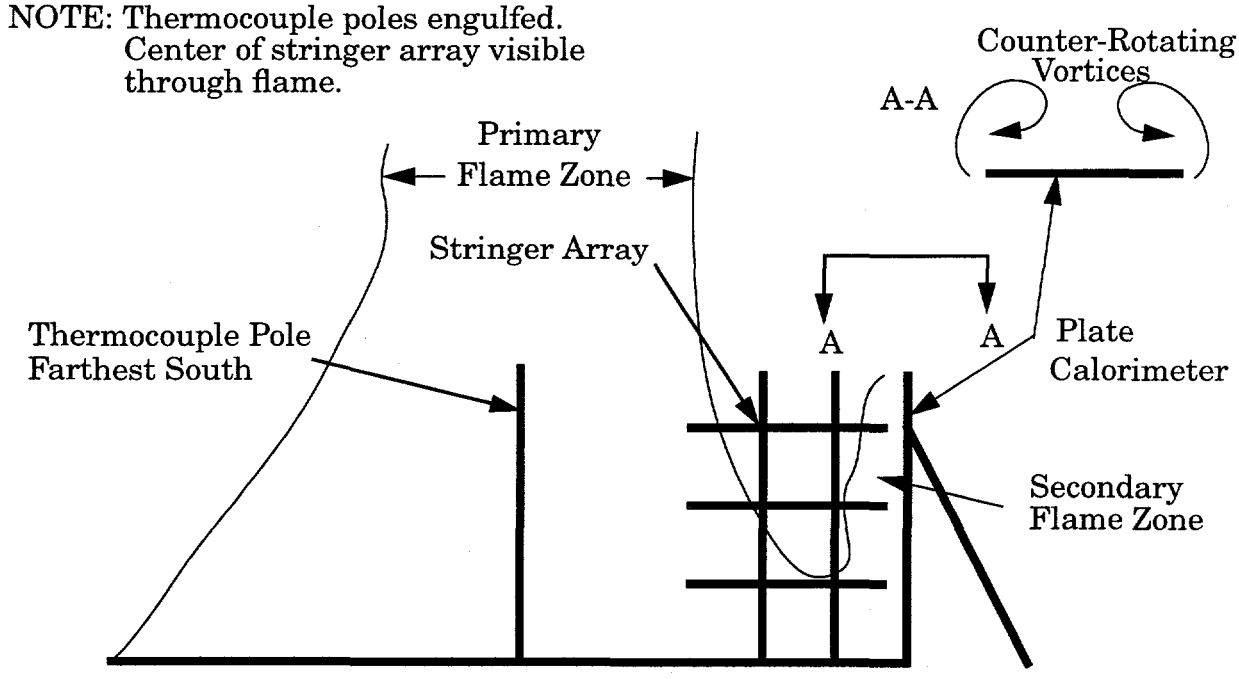

Figure 3.21 Flame Zone Shape, Quasi-Steady-State Time Period - Exp. 3

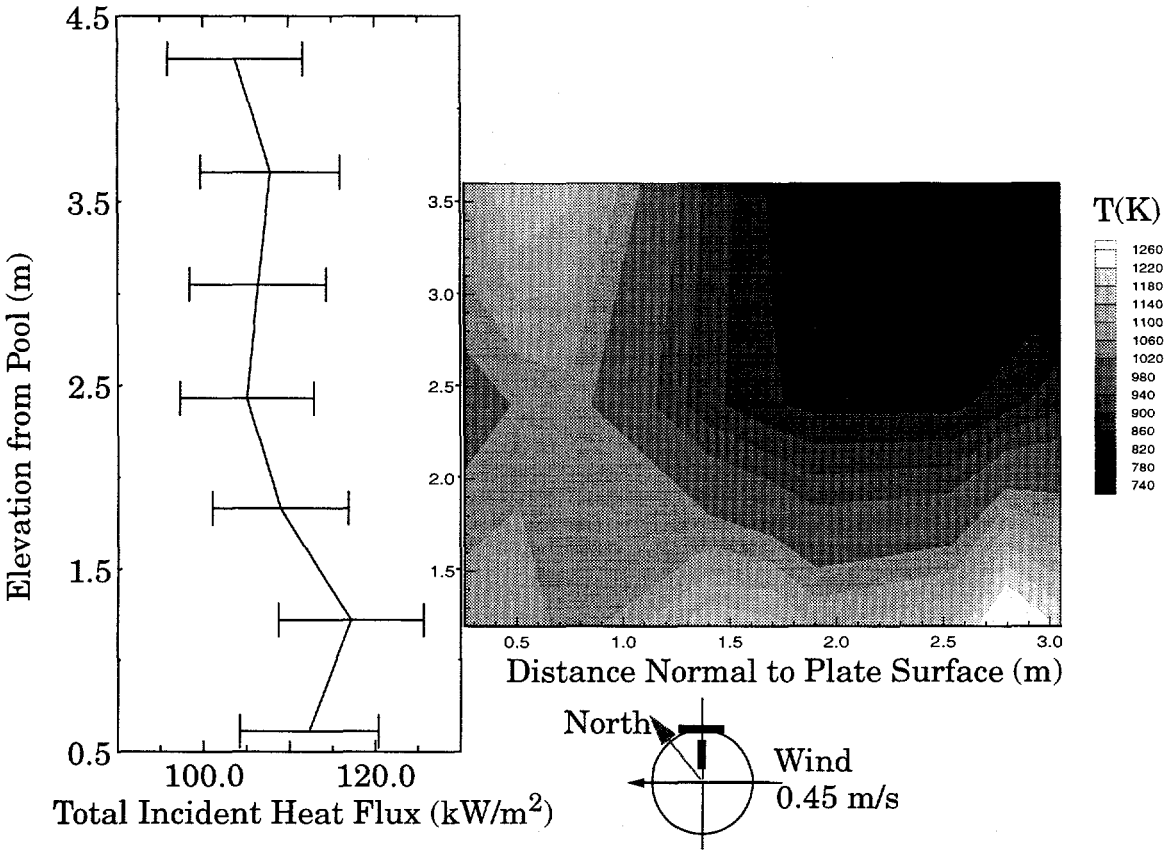

Figure 3.22 Heat Flux on Partially-Engulfed Calorimeter and Fire Thermocouple Temperature - Exp. 3

from the video record. Fire field model simulations [19] have been successful in capturing this phenomenon.

The presence of the secondary flame zone is evident in the thermocouple temperatures shown in Figure 3.22. The gap between the primary and secondary flame zones is illustrated by the low (<800 K) temperature region which extends down to an elevation of 2.5 m from the pool surface between 1.5 m and 2.5 m from the plate surface. High (up to 1200 K) temperatures associated with a secondary flame zone are evident up to 1.0 m from the plate at elevations of 1.2 to > 3.0 m.

As shown in Figure 3.22, heat fluxes of approximately 105 kW/m^2, which remain relatively constant with elevation, were measured at the front surface of the plate. These heat flux values are significantly larger than the ~ 40 kW/m^2 which one would estimate using standard practices [4] which neglect the formation of a secondary flame zone due to the presence of the object. In the data presented here, the heat fluxes are only 10-15% less than the fluxes measured for the fully engulfed case of experiment 1. Although the spatial extent of the flame cover adjacent to the object is

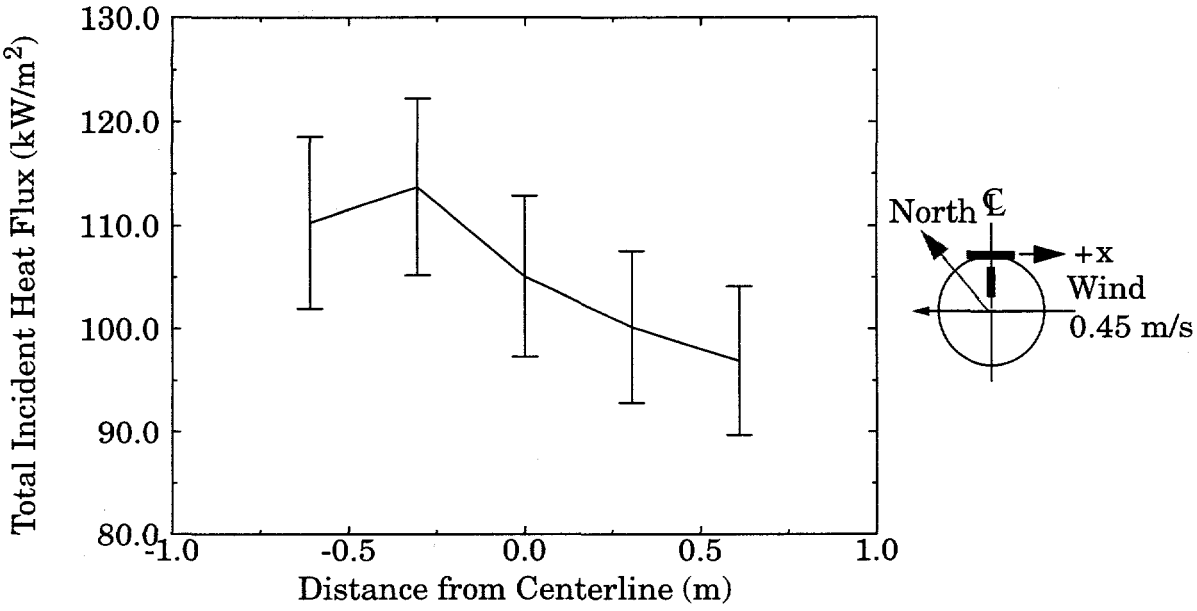

Figure 3.23 Horizontal Variation of Heat Flux at 2.4 m Elevation - Exp. 3

reduced for the wind conditions of experiment 3, high temperatures were measured between the large counter-rotating vortices. Additional heat flux to the calorimeter surface from enhanced convection is also expected for these conditions due to the formation of the vortical structures.

The potential formation of the secondary flame zone observed in this experiment can be assessed from the size of the vortical structures. The size of these structures is, in turn, related to an appropriate characteristic object length scale. Under quiescent conditions, the diameter of the vortices observed in this experiment were on the order of one half the plate width. Accordingly, this coupling can be expected when an object is located within a distance equal to or less than one half its width from the fuel pool. Asymmetries in wind conditions may produce vortical structures of unequal size. The entire width of the object therefore serves as a reasonable upper bound for the distance required to avoid the formation of a secondary flame zone.

The horizontal variation in heat flux to the front surface of the calorimeter for the time period identified during experiment 3 is given in Figure 3.23. The most significant variation in horizontal heat flux (97 to 110 kW/m^2) was observed for these conditions. The magnitude and character of this variation is consistent with the small wind component in the negative x direction as illustrated in Figure 3.23.

As mentioned previously, the vortices are formed on front surface of the plate primarily due to the restriction of entrained air. The wind adds an additional compo-

nent to the flow and therefore the exact size and location of the vortices is expected to be defined by the resultant flow component at the edges of the plate. A schematic illustrating the resultant flow vectors is given in Figure 3.23. Two effects can be identified which would result in the heat flux distribution shown in Figure 3.23. First, the highest heat flux is likely to be somewhere between the two vortices due to the presence of flame cover on both sides (and hence increased optical thickness) and due to increased convection caused by the impinging flow. The wind will tend displace the vortices towards the leeward side of the plate in a manner consistent with the data shown in Figure 3.24. Furthermore, the vortex on the windward side of the plate may be larger since the resultant flow vector is directed towards the centerline of the plate instead of away from the plate as evident on the lee side. Due to obscuration of the view it was not possible to compare the relative size and precise position of the vortices from inspection of the video record and confirm the preceding speculations.

The size of the vortices is expected to be smaller than several optical paths, and therefore the heat flux to the calorimeter will also be influenced by the temperature field beyond the individual vortices. Slight tilting of the primary flame zone, and increased mixing (and hence a high temperature region) on the leeward side of the instrumentation arrays placed in front of the calorimeter may therefore also explain the nonuniform horizontal heat flux distribution shown in Figure 3.23.

A plot of the hemispherical heat flux distribution, as measured by the HFGs in the plane directly in front of the calorimeter, is given in Figure 3.25. The trend is very similar to that given in Figure 3.13. In cases where two HFGs are placed on top of each other at approximately the same location, a significantly higher heat flux is measured by top HFGs at locations near the plate at the middle and top elevations. At the bottom elevation, and away (2.0 to 2.5 m) from the plate, a slightly higher

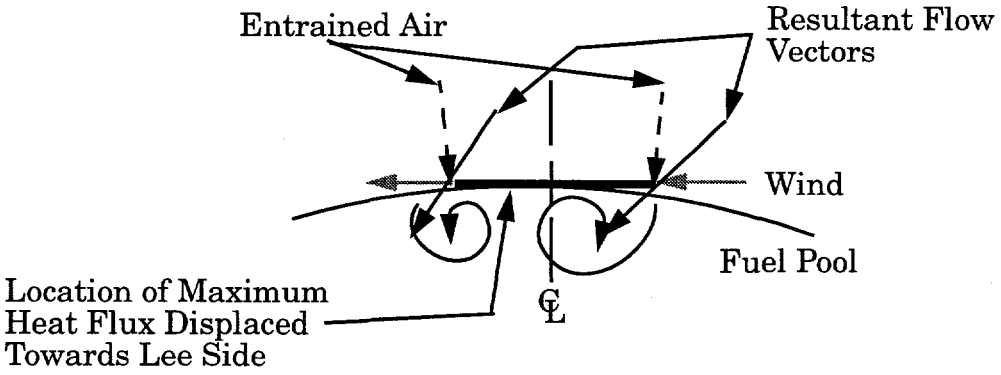

Figure 3.24 Influence of Wind and Entrained Air on Horizontal Heat Flux Distribution

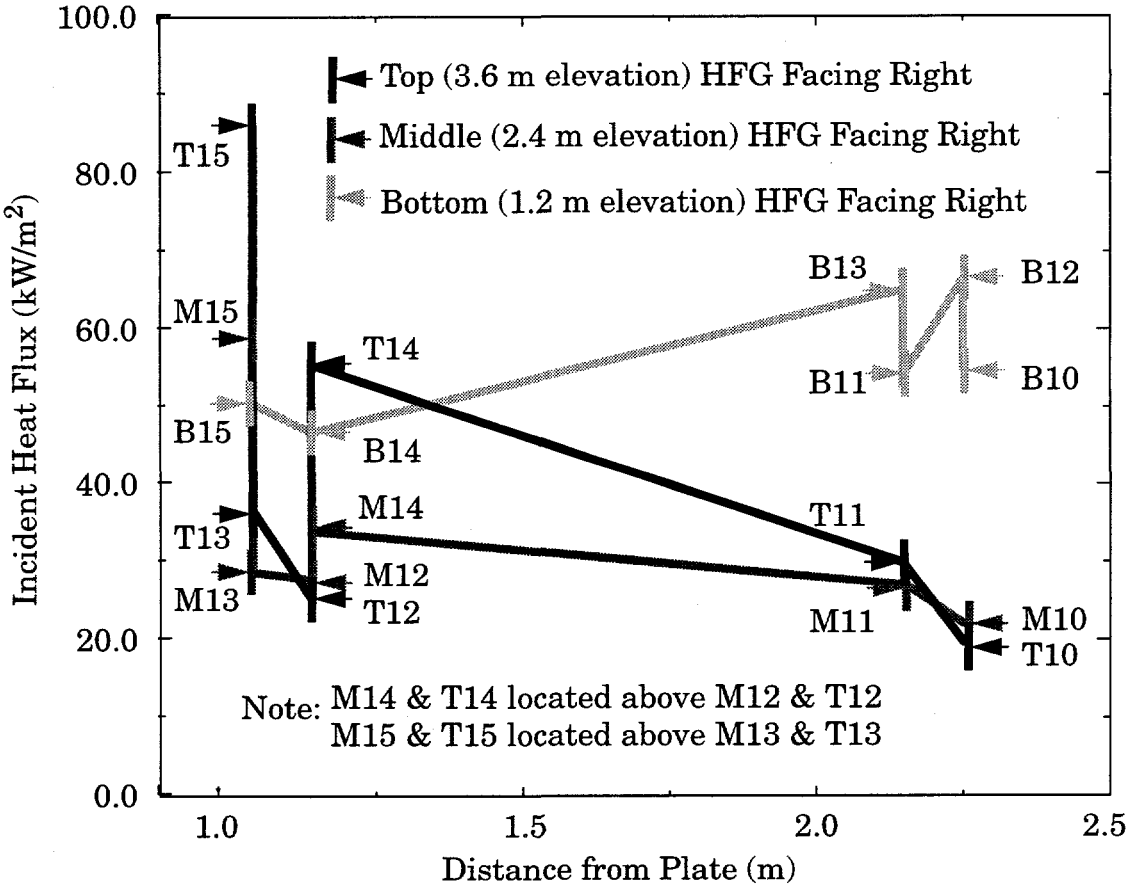

Figure 3.25 Hemispherical Heat Flux Distribution- Exp. 3

heat flux is measured by the bottom HFG. Since this location corresponds to the lower part of the primary flame zone, as shown in Figure 3.19, it is expected that the bottom HFG would be subjected to a greater incident heat flux. In this case, the local heat flux gradients appear to dominate the localized mixing effects caused by the lower HFG.

The time-averaged thermocouple temperatures measured along the plane away from the calorimeter are shown in Figure 3.26. It is again important to recognize the differences inherent between thermocouple and actual media temperatures. Several overall trends are evident which lend additional insight into the character of the fire in the region away from the calorimeter.

The main trends shown in Figure 3.26 are typical of a fire under calm conditions. This temperature distribution in this plane does not appear to be significantly influenced by the small wind component. The presence of a low temperature, oxygen-

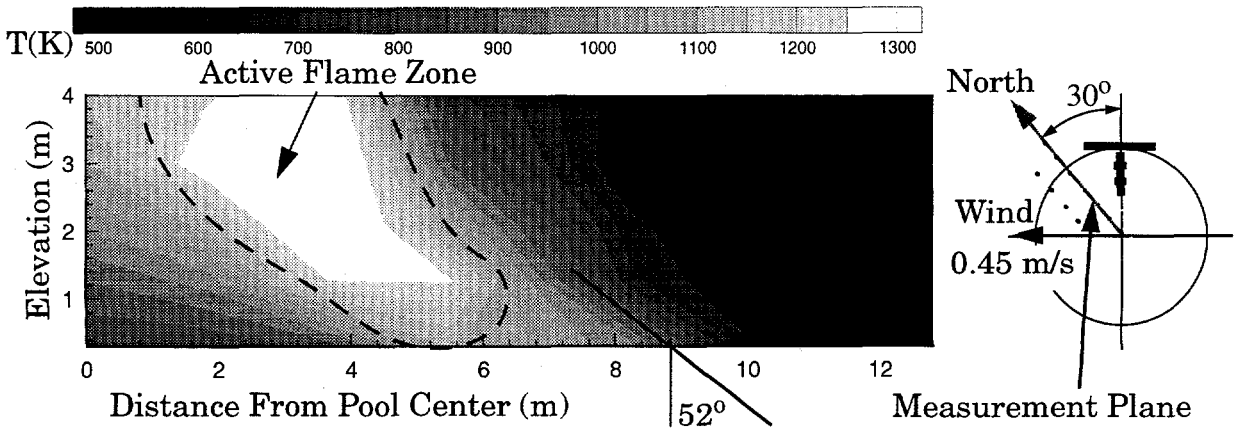

Figure 3.26 Fire Thermocouple Temperature Distribution, Plane Through Pool Center - Exp. 3

starved interior is shown by the region of low (~800 K) temperatures which extends up to nearly 4 m at the centerline and to an elevation of approximately 0.3 m at a distance of approximately 5 m from the pool center. A large, active flame zone with temperatures near 1300 K is shown in Figure 3.26 which increases in width with increasing elevation. This increase in the width of the active flame zone is consistent with the increased ability to mix air into the flame interior with increasing distance from the ground plane (which effectively limits air entrainment at the fuel surface).

The necking of the flame zone which occurs just above the ground plane is also clearly evident in Figure 3.26. This necking is due in part to the momentum of the entrained air. Inspection of the contour lines shows the angle at which the flame zone necks to be approximately 52° near the foot of the flame. As expected, the contour lines become increasingly vertical with increasing elevation. These results do, however, show that the flame zone profile still forms a significant angle from the vertical, and therefore is continuing to neck, at an elevation of 4 m.

The thermocouple temperature distribution along the plane farthest from the calorimeter is shown in Figure 3.27. The same basic flame zone shape is evident, however the cold region in the interior of the flame zone is smaller. This trend is consistent with the expected decrease in the size of the oxygen-starved region with increasing distance from the pool center.

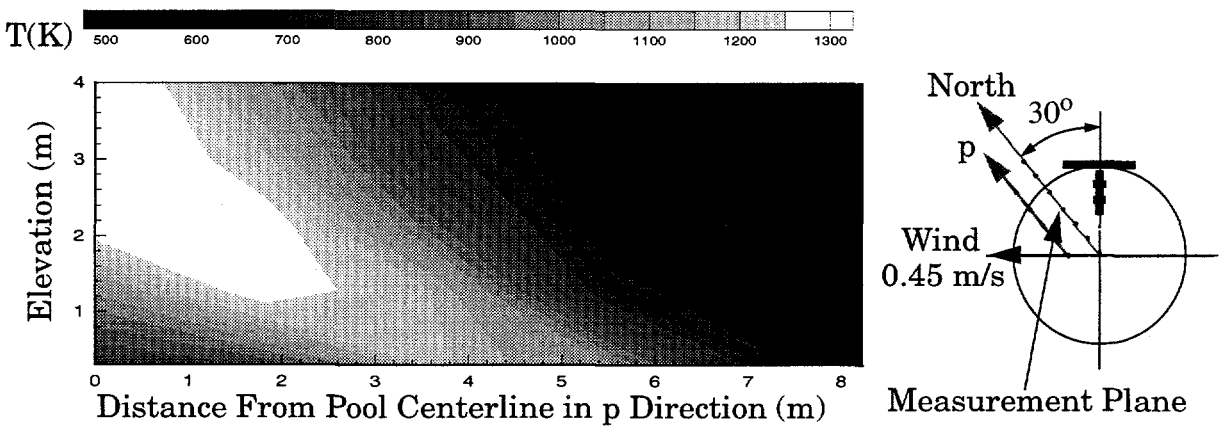

Figure 3.27 Fire Thermocouple Temperature Distribution, Plane West of Pool Center - Exp. 3

4. Summary and Conclusions

4.1 Summary of Results

As part of the full scale fuel fire experimental program, a series of 18.9 m diameter JP-4 pool fire experiments with a large (2.1 m X 4.6 m) flat plate calorimeter adjacent to the fuel pool were recently performed at NAWCWPNS. The instrumentation employed, the conditions under which each experiment in the series was performed, the data collected during this series, and qualitative interpretation of the results in terms of relevant physical mechanisms, is presented here. The data are presented in a manner suitable for comparison with model predictions. The trends in the data offer additional insight into the relevant physical mechanisms in fires and therefore support the further development of our understanding of fire phenomena and the development of improved computational models. Although a comprehensive knowledge of "free fires" (i.e. fires without objects) has yet to be obtained, a principal benefit of this series of experiments is the data and insight gained for conditions where an object of significant size compared to the size of the fire is subjected to the fire environment. Under these conditions, the presence of the object influences the fire and the resulting fire environment is more difficult to envision a priori.

Differing wind conditions for each of the three experiments resulted in cases where the calorimeter is fully engulfed, not engulfed, and partially engulfed by a secondary flame zone. Results from this series of experiments include the following:

1. Average JP4 fuel consumption rates increased from 0.069 kg/m^2-s (5.4 mm/min) to 0.081 kg/m^2-s (6.4 mm/min) with increasing average wind speeds of 0.65 to 2.0 m/s, respectively.
2. The temperature of the calorimeter increased slowly during the experiment, reaching a maximum of 1000 K near the fuel surface under partially-engulfed conditions.
3. The uncertainty associated with determining the average incident heat flux to the calorimeter was negligibly affected (4%) by the increase in temperature as a function of time and strongly (15%) affected by assumptions relating to the surface radiative properties.
4. The highest incident heat fluxes (130 kW/m^2) were observed under fully engulfed conditions.
5. The highest thermocouple temperatures (1280-1480 K) were recorded near the plate under fully engulfed conditions.
6. Horizontal variation in the heat flux to the plate ranging from 6 to 20% was observed during the series of experiments. The largest variation occurred under partially engulfed conditions subject to low (0.45 m/s) winds.

7. Heat fluxes representative of previous data for the emissive power of the smoke layer (20 kW/m^2) were observed at elevations of 3.5 to 4.5 m when the calorimeter surface was 2.0 m outside of a flame zone which was directed away from the calorimeter by the wind.
8. Under quiescent conditions, restriction of entrained air by the calorimeter results in a secondary flame zone in the form of standing vortices at the calorimeter edges. Incident heat fluxes on the calorimeter of 100 - 115 kW/m^2 (within 10-15% of the fully engulfed case) at elevations from 0.5 to 4.5 m were measured.

4.2 Conclusions

The results presented here emphasize the importance of the object/wind/flame interactions in determining the heat flux from a fire to an object. A subset of these phenomena can be referred to as "object-induced turbulence" since the fuel/air mixing and the fine structure turbulence, which strongly defines the character of the fire, is affected due to the presence of the object. Under these conditions, the thermal hazard posed by the fire is coupled with the object geometry, location and orientation. Since, under quiescent conditions, the length scale of the flow structures is related to the size of the object, this coupling can be expected when the object is located within a distance from the fuel pool equal to the appropriate characteristic length of the object.

The importance of these scenarios is emphasized by the data presented here. Differences greater than a factor of 2 are observed between the measured heat fluxes and heat flux estimates which neglect these features and treat the object as being located a finite distance from a cylindrical flame zone. For two of the cases presented here, only small (10-15%) differences in the absorbed heat flux for fully and partially engulfed scenarios were observed. In order to obtain credible estimates of heat fluxes, these features must be represented.

These results also confirm previous work regarding the extent of oxygen-starved regions in the interior of large pool fires, and the coupled thermal response of large, thermally massive objects and participating media on the heat flux to an object in a large hydrocarbon pool fire. The influence of small objects, such as HFGs, on the local fire environment is also emphasized by these results and should be considered in experimental design.

5. References

[1] Gritzo, L. A., Moya, J. L., and Nicolette, V. F. "Use of Simplified Deterministic Fire Models to Estimate Object Response for Probabilistic Fire Safety Assessments," Proceedings of the NIST Annual Conference on Fire Research, Rockville, MD., October 18-22, 1993.

[2] Nicolette, V.F, Tieszen, S.R., Gritzo, L.A., Holen, J. and Magnussen, B.F., "Field Model Validation for Pool Fires", Poster Presented at Fourth International Symposium on Fire Safety Science, Ottawa, Canada, June 13-17, 1994.

[3] Lopez, A.R., Gritzo, L.A., and Sherman, M.P. "Risk Assessment Compatible Fire Models (RACFMs)", SAND Report in Final Preparation. Sandia National Laboratories, Albuquerque, NM.

[4] Mudan, K. S., and Croce, P. A. "Fire Hazard Calculations for Large, Open Hydrocarbon Pool Fires," *The SFPE Handbook of Fire Protection Engineering, First Edition*, National Fire Protection Association, Quincy, MA, 1990.

[5] Gritzo, L.A., Castleberry, J.A., Jakway, A.L., and Moya, J.L. "Heat Flux Measurements in Large, Engulfing Fires - Design and Calibration of a Robust, Cost-Effective, Hemispherical Heat Flux Gauge" SAND Report in Final Preparation, Sandia National Laboratories, Albuquerque, NM.

[6] Gritzo, L.A., Nicolette, V.F., Tieszen, S.R., and Moya, J.L. "Heat Transfer to the Fuel Surface in Large Pool Fires," *Transport Phenomenon in Combustion*, S.H. Chan, ed., Taylor and Francis, 1996.

[7] Handbook of Aviation Fuel Properties, Coordinating Research Council, Inc., Atlanta, Georgia, CRC Report No. 530, 1983.

[8] Blinov, V.I., and Khudyakov, G. N. "Diffusion Burning of Liquids," English Translation: U.S. Army Engineering Research and Development Labs, Fort Belvoir, VA, Report AERDL-T-1490-A, 1961

[9] Blackwell, B.F., Douglass, R.W., and Wolf, H. "A User's Manual for the Sandia One-Dimensional Direct and Inverse Thermal (SODDIT) Code" SAND85-2478, Sandia National Laboratories, Albuquerque, NM, Reprinted 1990.

[10] Longenbaugh, R.S., Sanchez, L.C., and Mahoney, A.R. "Thermal Response of a Small Scale Cask-Like Test Article to Three Different High Temperature Environments - Appendix B, Thermal Radiative Properties of Pyromark Series 2500 Black Paint", SAND 88-0661, Sandia National Laboratories, Albuquerque, NM, 1989. Alternate Reference DOT/FRA/ORD-90/01, February 1990.

[11]Koski, J.A., Gritzo, L.A., Kent, L.A., and Wix, S.D."Acitvely-Cooled Calorimeter Measurements and Environment Characterization in a Large Pool Fire", *Fire and Materials*, Vol. 20, pp. 69-78, 1996.

[12]incropera, F. P., Dewitt, D.P., *Fundamentals of Heat and Mass Transfer*, Second Edition, Wiley & Sons, New York, 1985.

[13]Gritzo, L.A., Gill, W., and Keltner, N. "Thermal Measurements to Characterize Large Fires," Proceedings of The 41st International Instrumentation Symposium, Denver, CO, May 7-11, 1995.

[14]Nicolette, V. F. and Larson, D. W. "The Influence of Large Cold Objects on Engulfing Fire Environments," Heat and Mass Transfer in Fires. J. G. Quintiere and L. Y. Cooper (eds), ASME HTD Vol. 141, pp. 63-70, 1992.

[15]Gritzo, L.A., and Nicolette, V.F. "Coupled Thermal Response of Objects and Participating Media in Fires and Large Combustion Systems", *Numerical Heat Transfer, Part A*, 28:531-545, 1995.

[16]Gritzo, L.A., Time-Averaged Photographs of Experiments Perfromed NAWC. Copies available by request.

[17]Gritzo, L.A., Moya, J.L. and Nicolette, V.F. "Continuous Flame Zone Measurements and Analysis from Large, Open JP-4 Pool Fires including the Effects of Wind," Proceedings of the 1994 NIST Annual Conference on Fire Research, Gaithersburg, MD, October 1994

[18]Cetegen, B. M., and Ahmed, T.A. "Experiments on the Periodic Instability of Buoyant Plumes and Pool Fires" *Combustion and Flame*, Vol. 93, pp. 157-184, 1993.

[19]Gritzo, L.A., Nicolette, V.F., and Tieszen, S.R "Preliminary Comparison of KAMELEON Fire Model Results to Data from Large Open Pool Fires Including the Effects of Wind and Objects", Presented at the Open Forum on Fires and Combustion at the 1993 ASME Winter Annual Meeting.

Appendix A - Flat Plate Calorimeter Design Drawings

Calorimeter Design by Larry Kent, Thermal Characterization and Simulation, Department 2735, Sandia National Laboratories.

Plate Calorimeter

Drawing name
PL-CALF

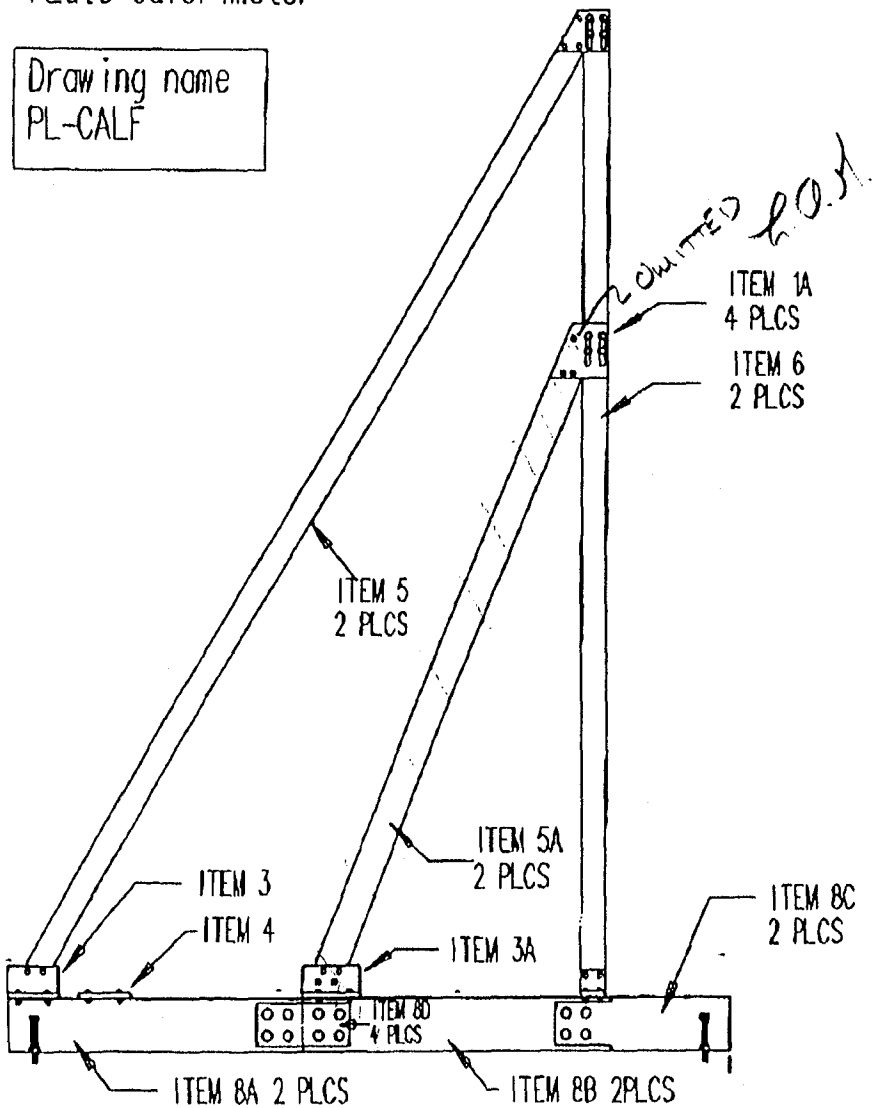

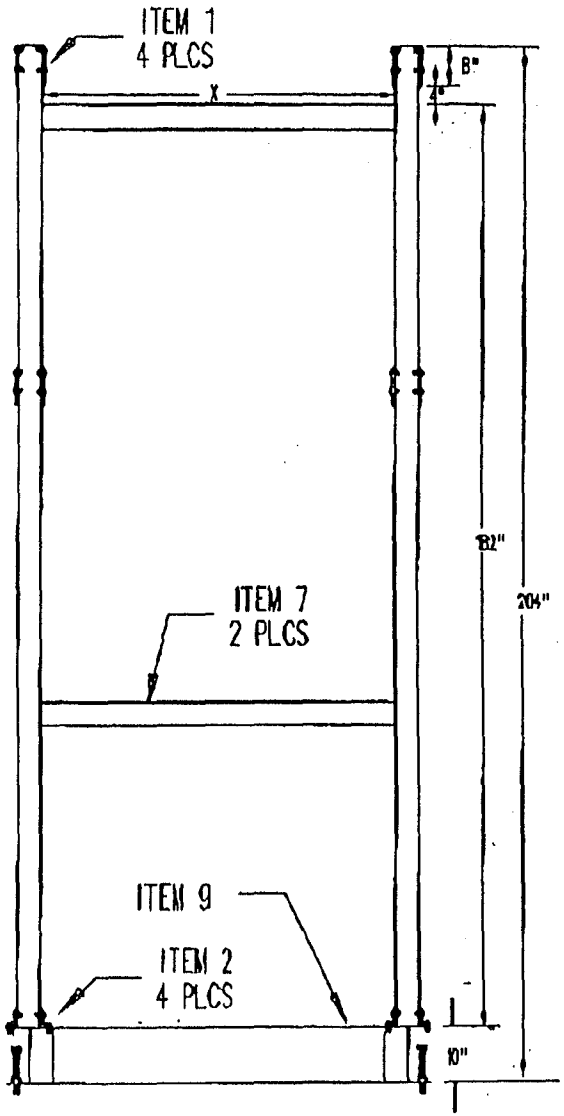

ITEM 1
4 EACH
0.25" THICK MILD STEEL

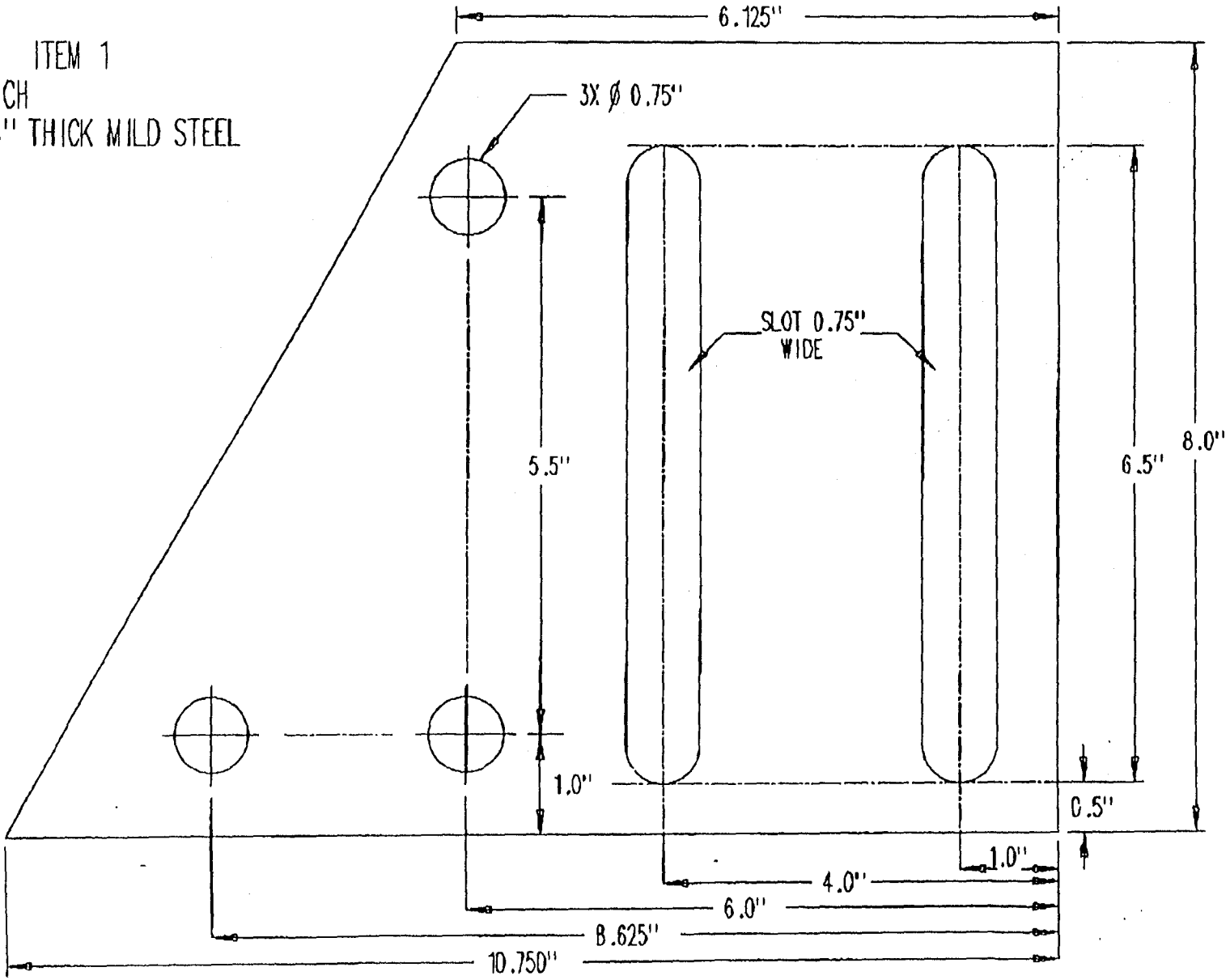

ITEM 1A
4 EACH
0.25" THICK MILD STEEL

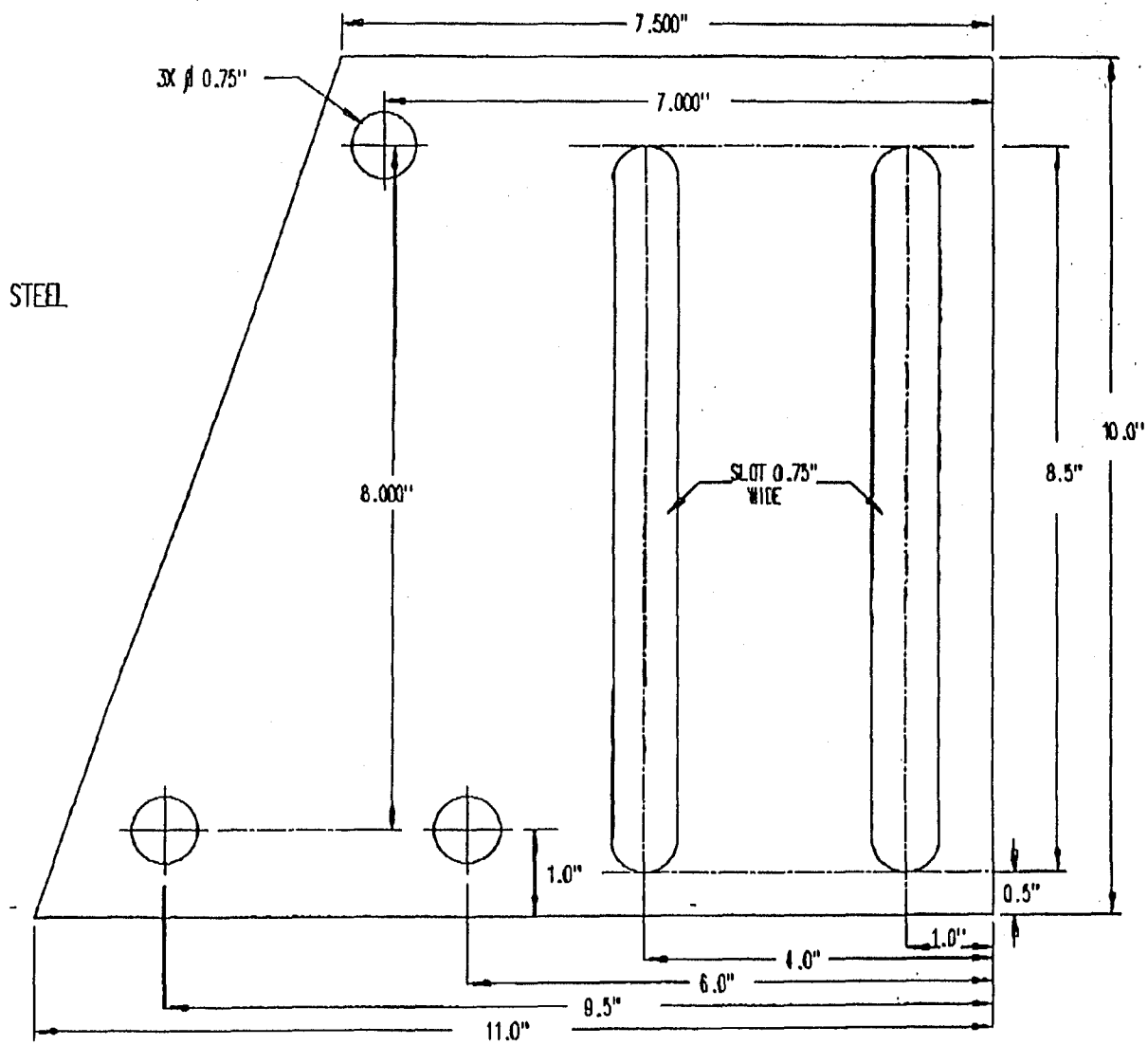

ITEM 2

4 EACH
0.25" THICK MILD STEEL

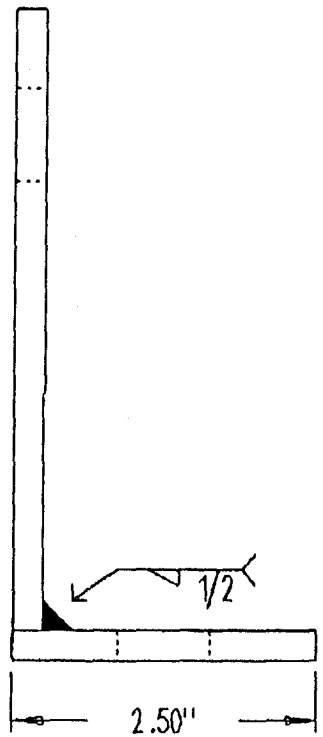

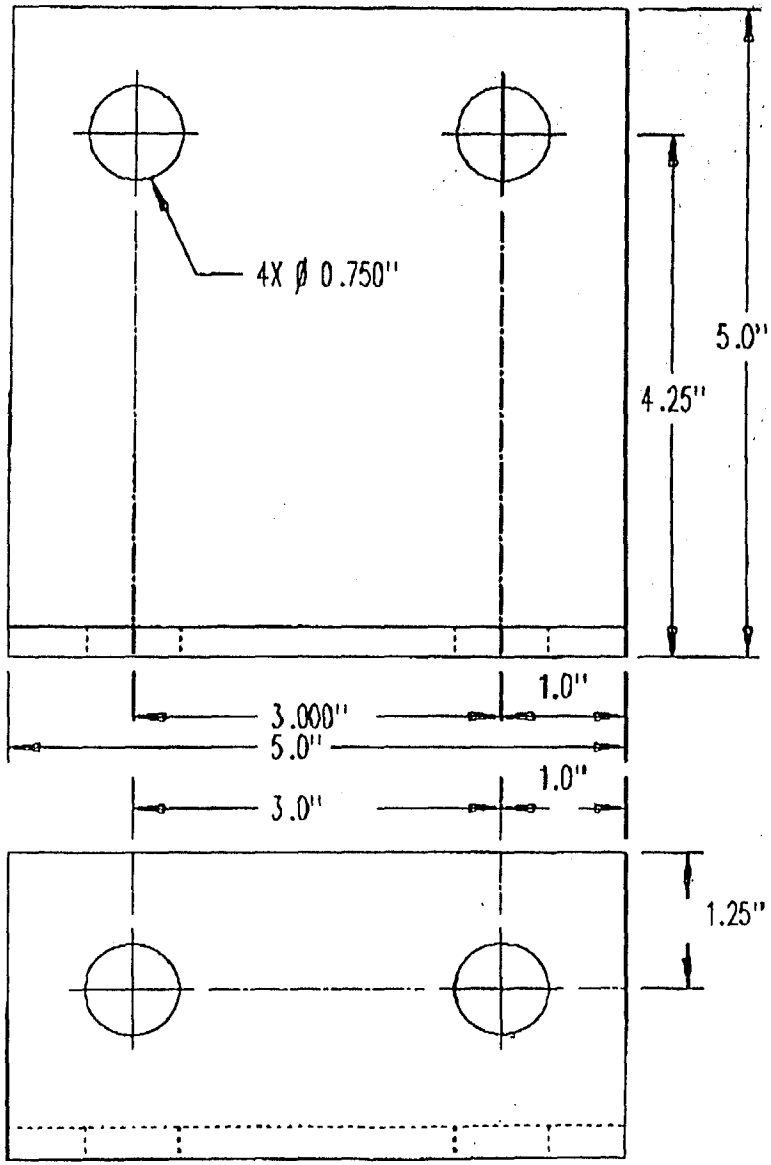

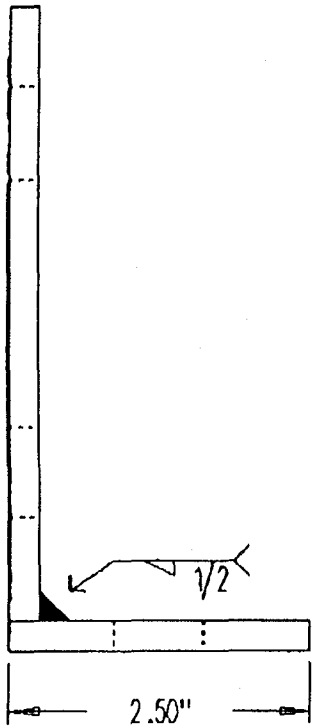

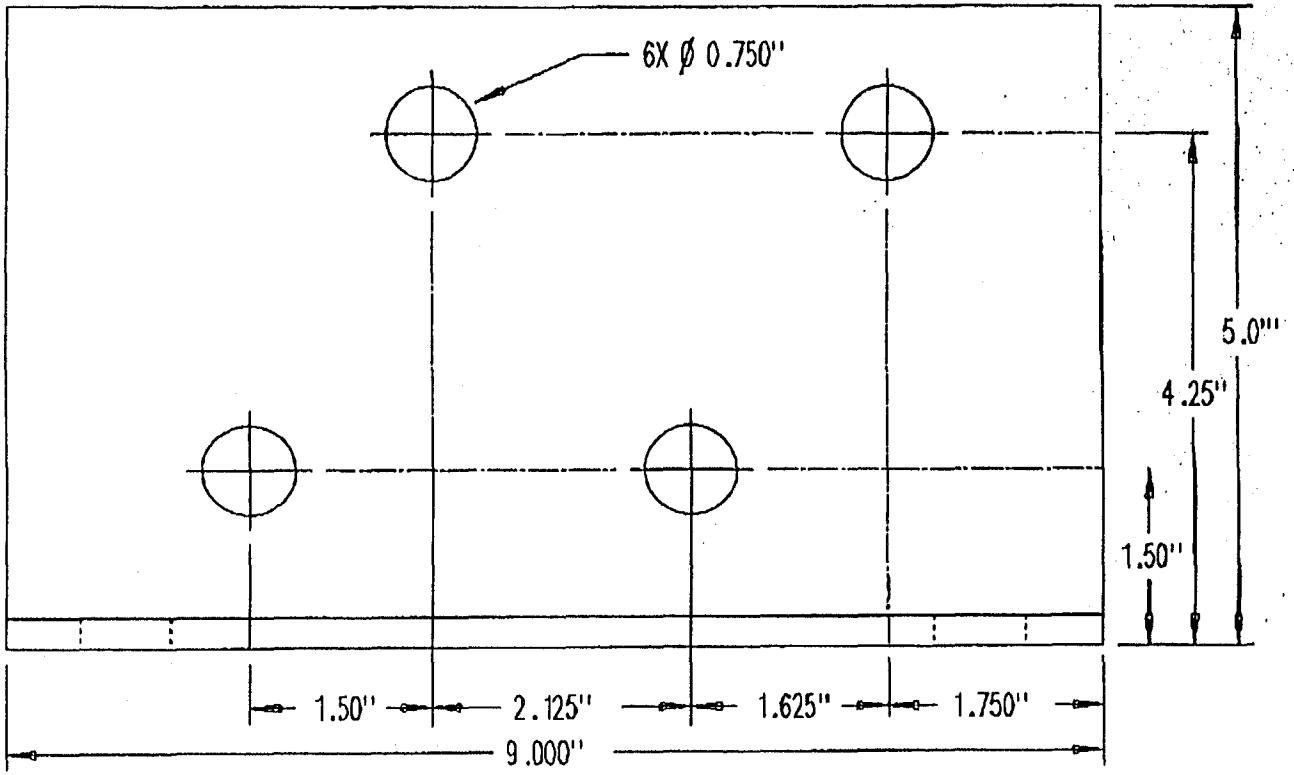

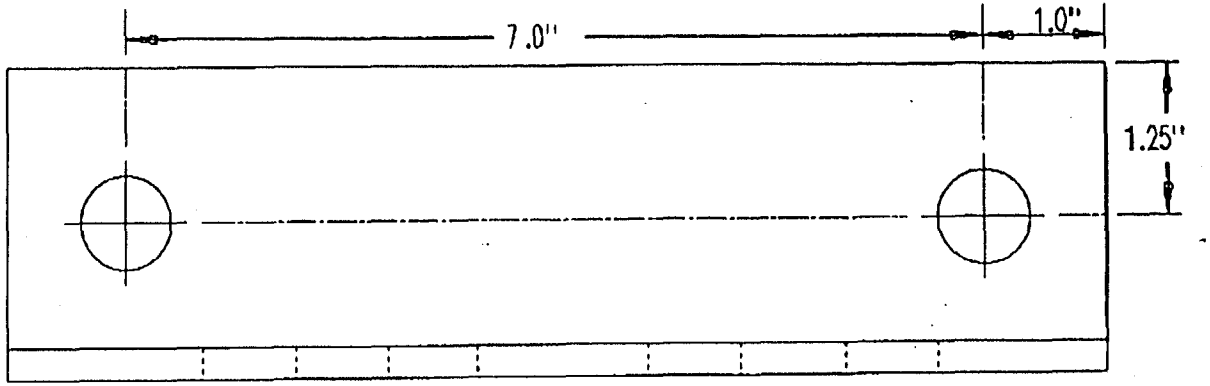

ITEM 3

4 EACH

0.25" THICK MILD STEEL

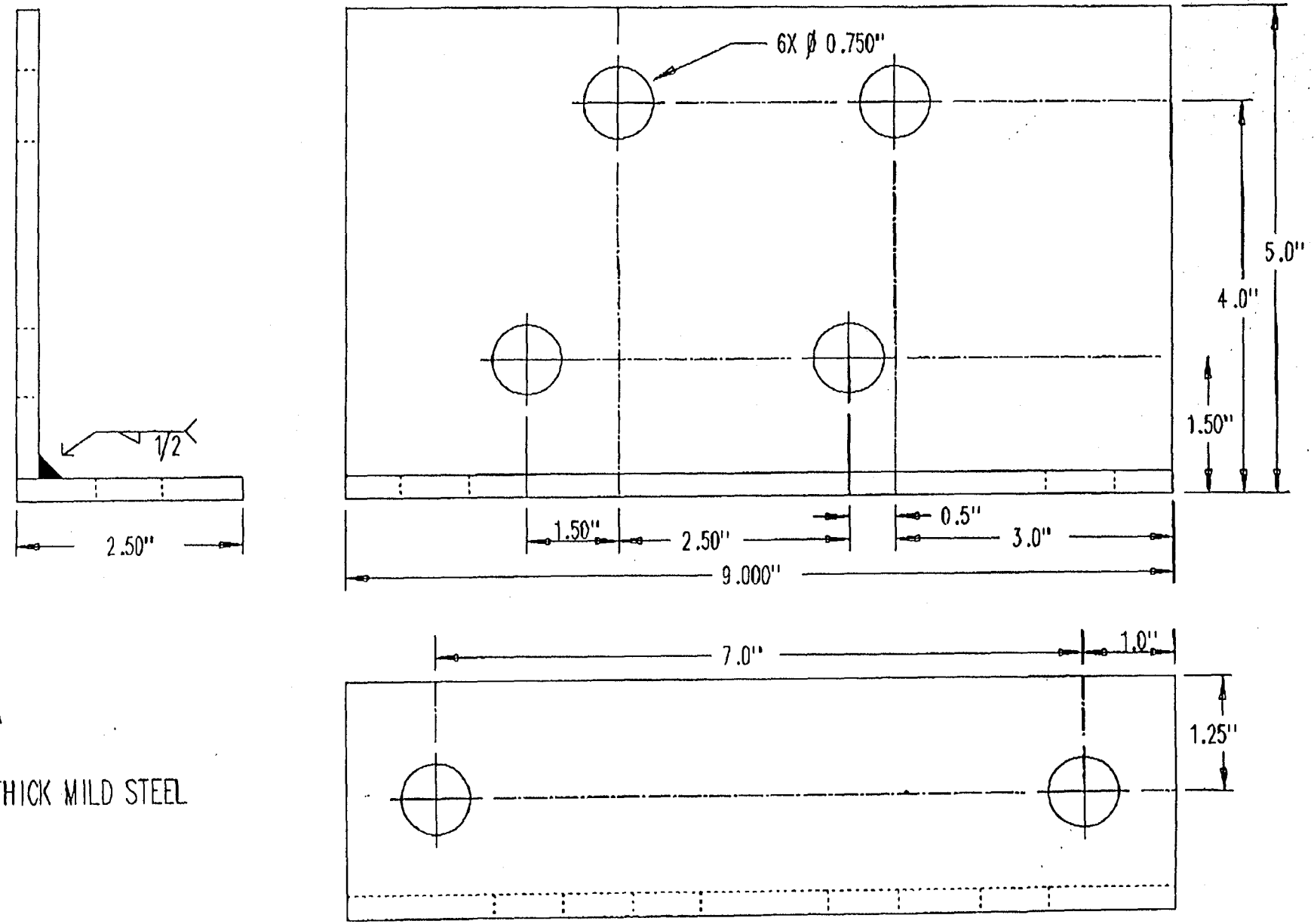

ITEM 3A

4 EACH
0.25" THICK MILD STEEL

ITEM 4
2 EACH
0.25" THICK MILD STEEL

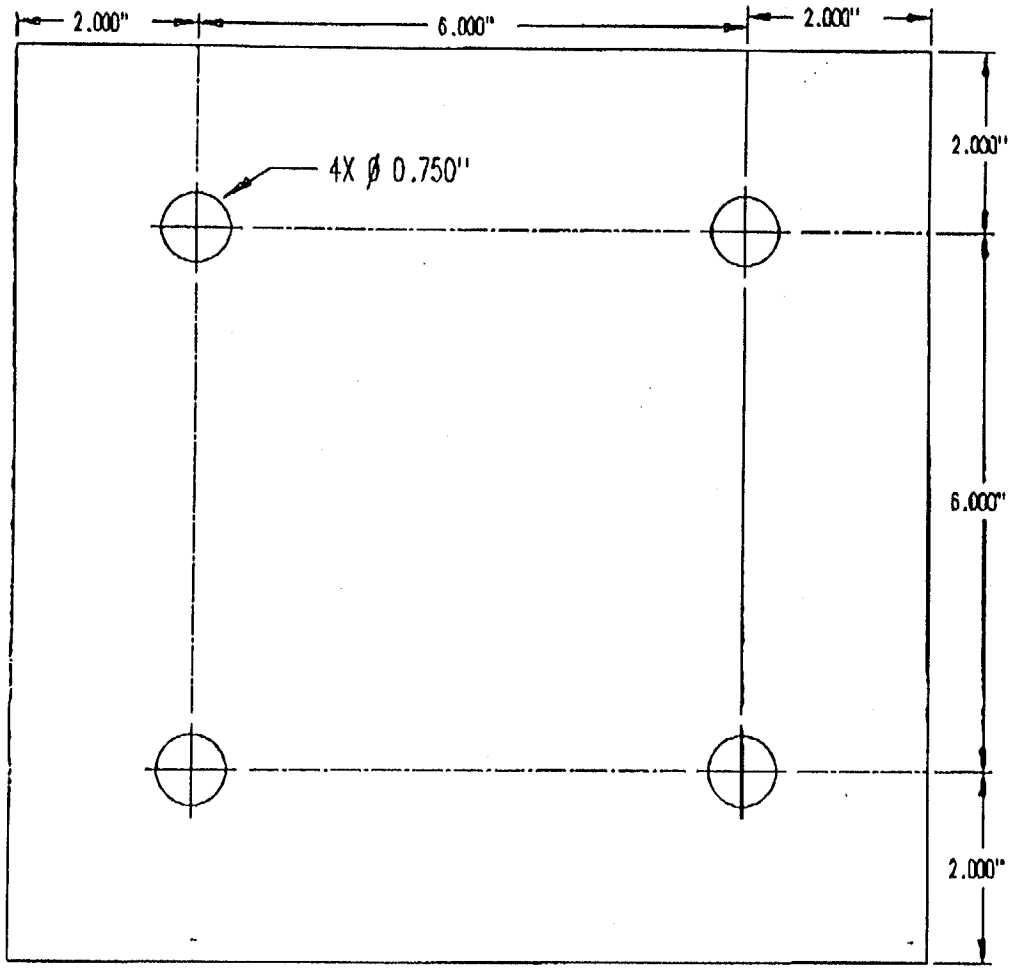

ITEM5

2 EACH
WFB 5X5

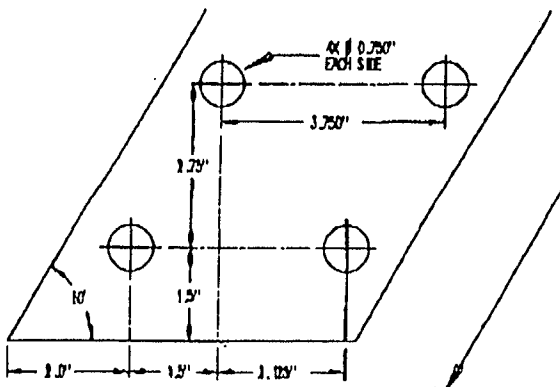

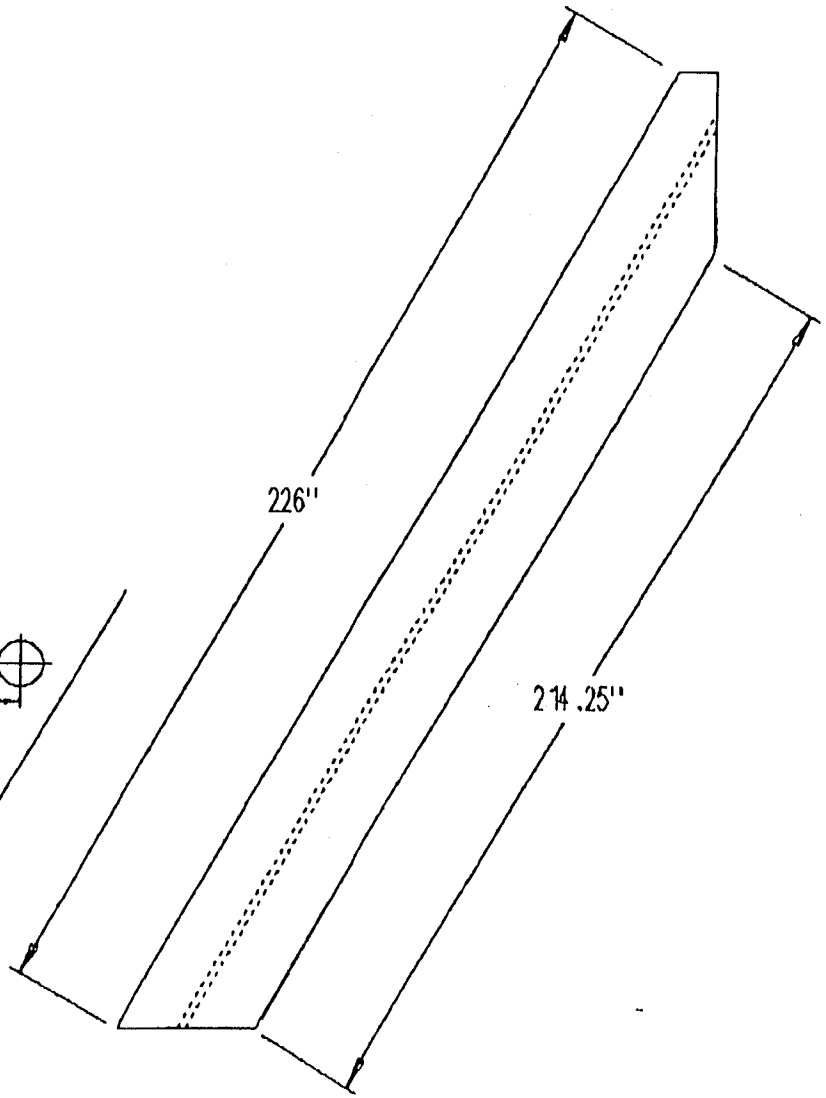

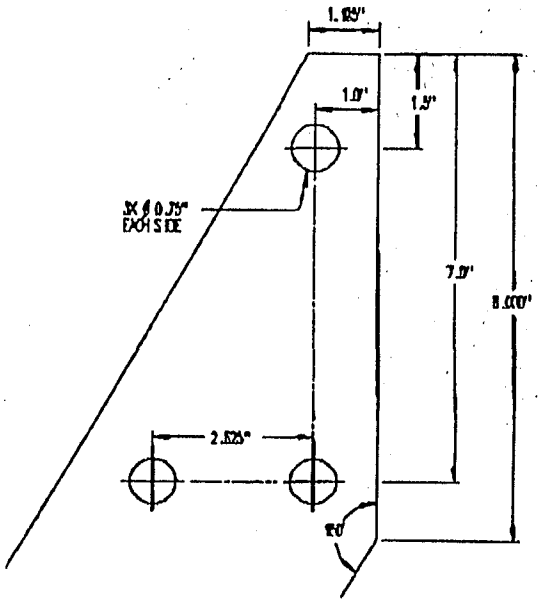

09

ITEM5A

2 EACH

WFB 5X5

ITEM6
2 EACH
WFB 5X5

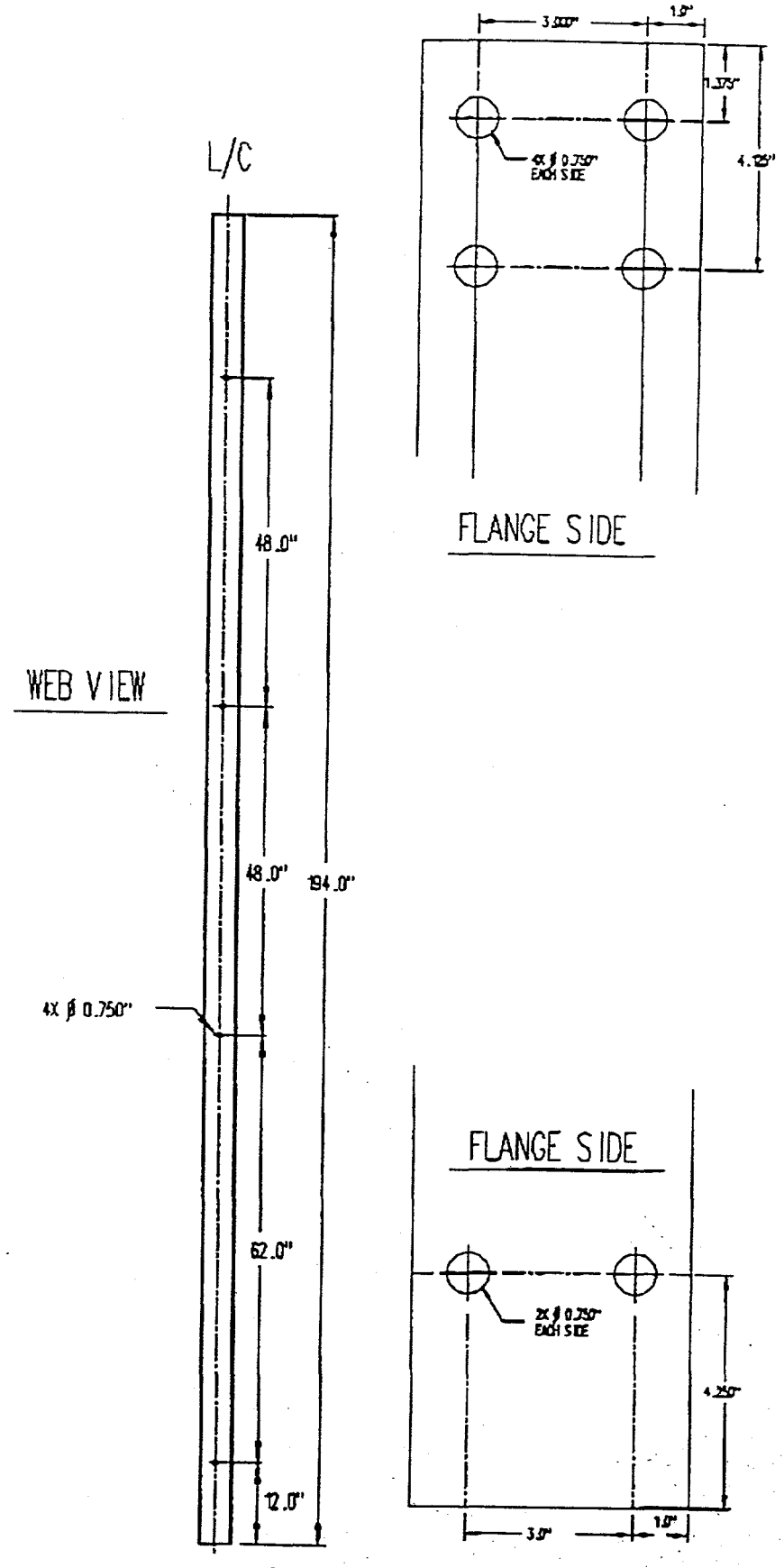

ITEM7
2 EACH
WFB 5X5

ITEM8
W 10X49

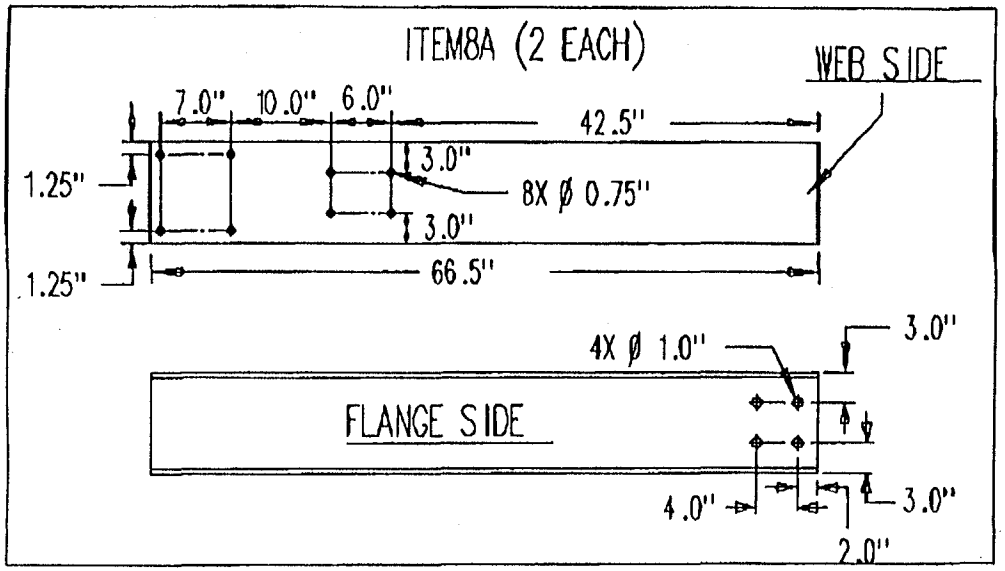

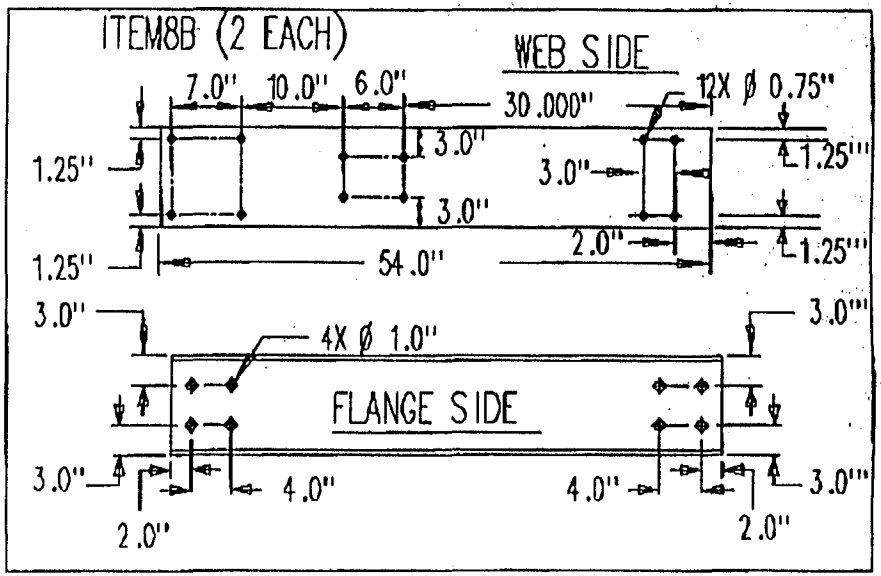

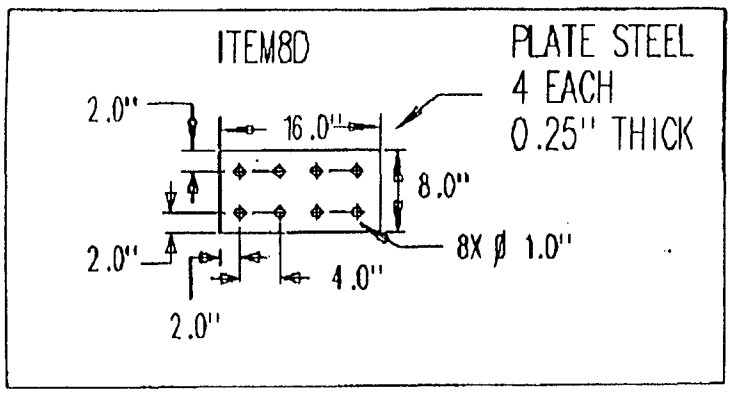

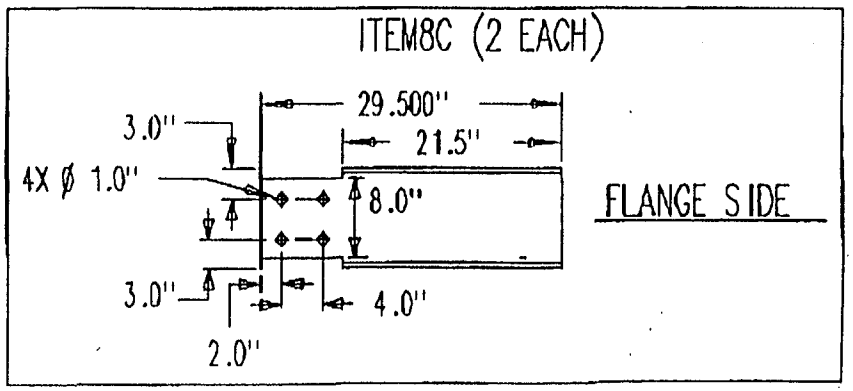

ITEM9
1 EACH
W 10X49

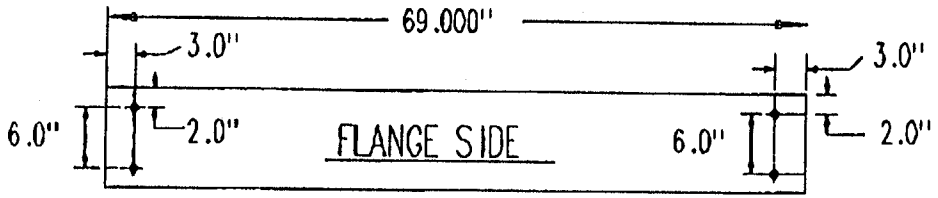

ITEM 10
1 EACH
1.25" STEEL PLATE

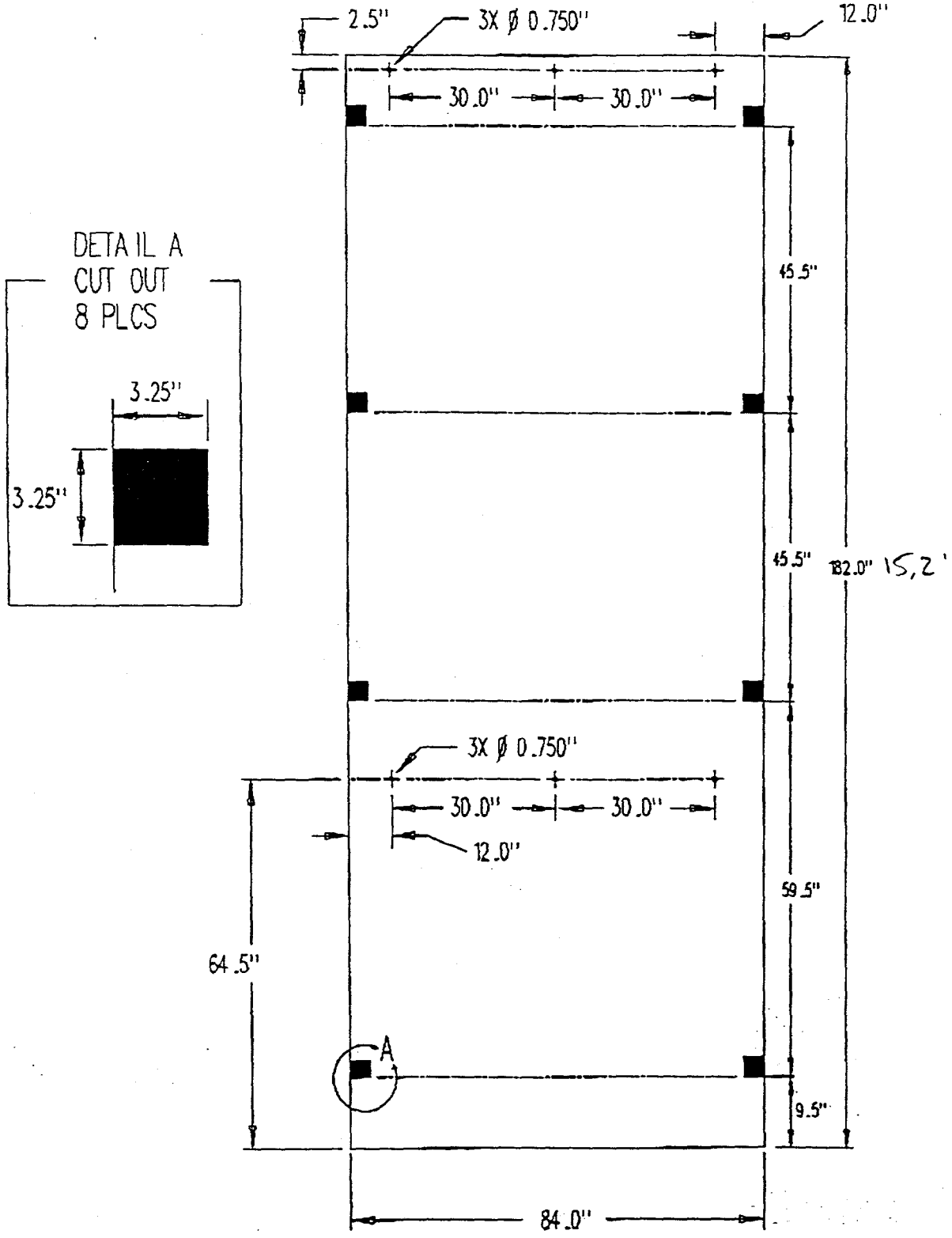

ITEM 11
1 EACH
0.125" STEEL PLATE

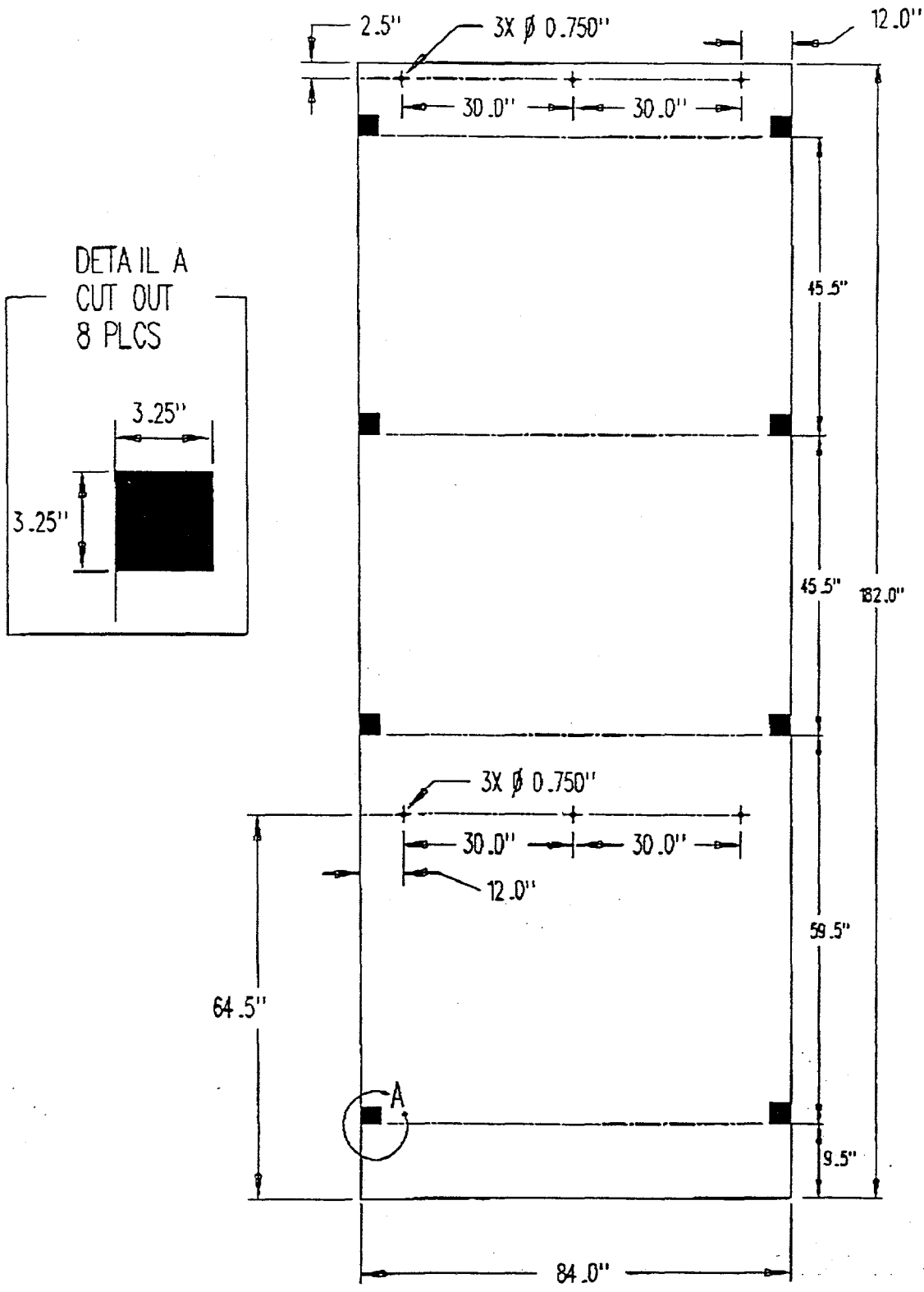

ITEM 12
WASHER
16 EACH
0.125" MILD STEEL

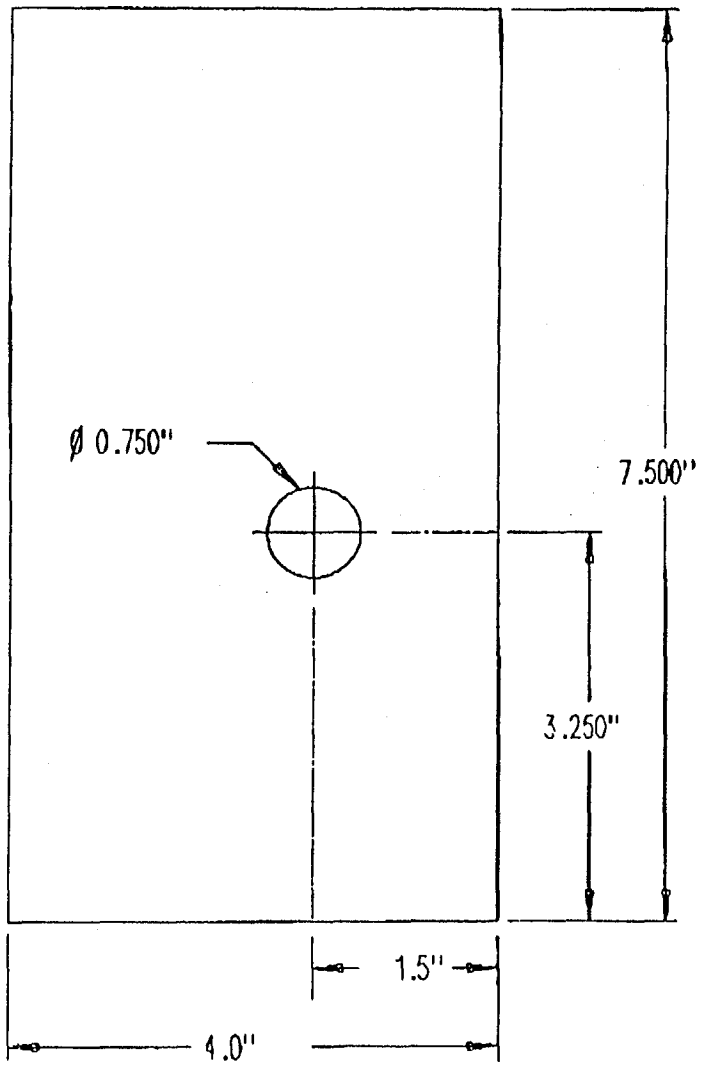

(Left Blank Intentionally)

Appendix B - Justification for the Simple SODDIT Model

SODDIT was used to solve the one-dimensional inverse conduction problem associated with estimating the temperature and heat flux at the surface of the calorimeter. A detailed model which includes the air gap behind the Semi-Rigid insulation, and the corrugated back plate, is shown in Figure A.1. A simplified model, which assumes no heat loss from the back of the insulation, is shown in Figure A.2.

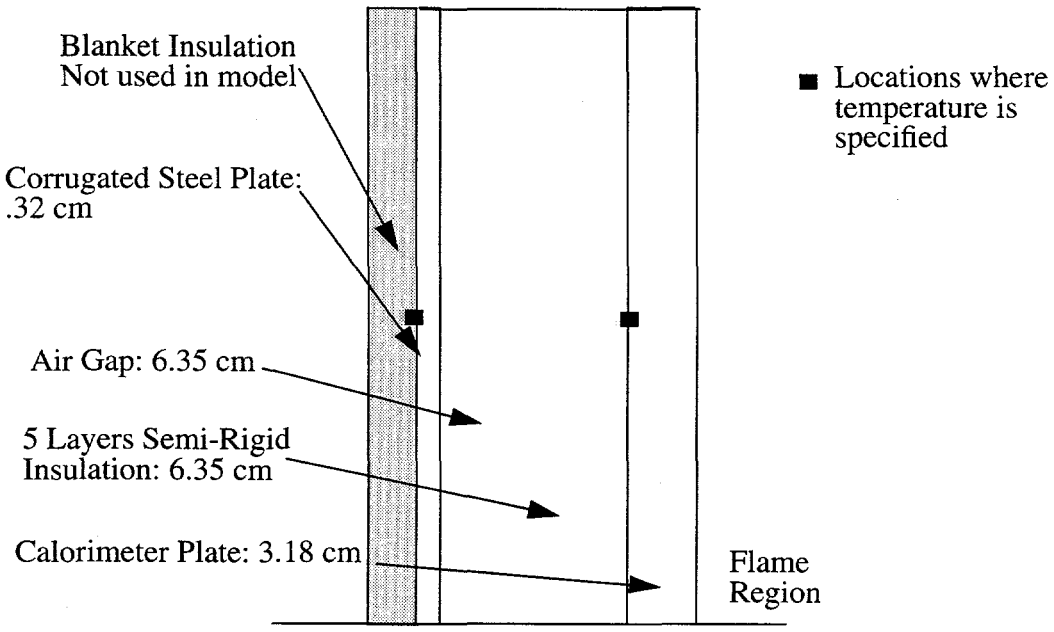

Figure A.1 Detailed SODDIT Calorimeter Model

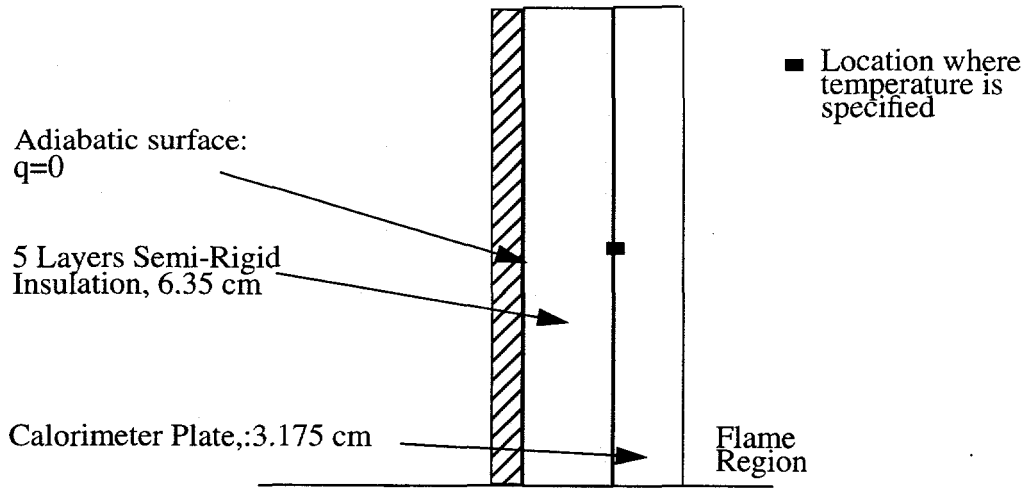

Figure A.2 Simplified SODDIT Calorimeter Model

To determine the required level of complexity, SODDIT was run on both models for the middle height. All program parameters were held constant, except for the addition of the air gap and back plate. Both models used the same known temperature history at the interface between the front steel plate and the insulation. For the actual model, the rear boundary condition was a measured temperature at the back of the back plate. For the simplified model, An adiabatic rear boundary condition was employed in the simplified model. The results from the two models are the same. The simplified model, therefore, represents the essential features of the assembly and was used to provide all of the heat flux estimates presented here.

Table A.1: SODDIT Output for Detailed and Simplified Models

Quantity	Model Predictions	
	Detailed	Simplified
Average surface T^4 (K^4)	0.356559E12	0.356559E12
Highest surface T^4 (K^4):	0.477914E12	0.477914E12
Lowest surface T^4 (K^4):	0.255727E12	0.255728E12
Average surface flux (W):	118001	118001

Appendix C - Selection of SODDIT Parameters

SODDIT parameters for the numerical simulation were selected as follows:

- Temperature Dependent property data for the ANSI mild steel plate were taken from Incropera and Dewitt, [12]. Data were input for 200 K increments from 300K to 1000K; SODDIT interpolates where necessary.
- Property data for the ceramic fiber were taken from manufacturer's documentation, and assumed to be constant over the whole temperature range of operation.
- The calorimeter model used for the simulation is shown in Figure B.1 below
- The 3.175 cm steel plate and the 6.35 cm insulation layer were each divided into 25 elements.
- The duration of the simulation extends from before the fire starts to beyond the region of interest, to assure consistency of the results during pre and post fire periods.
- The boundary conditions are (1) an adiabatic back surface (q=0) and (2) a specified temperature history at the steel/insulation interface.
- A fully implicit numerical scheme [theta = 1] was used.
- 5 future times were used to obtain each estimate of surface flux.
- Data at 10 second intervals were used as input to prevent unstable behavior.

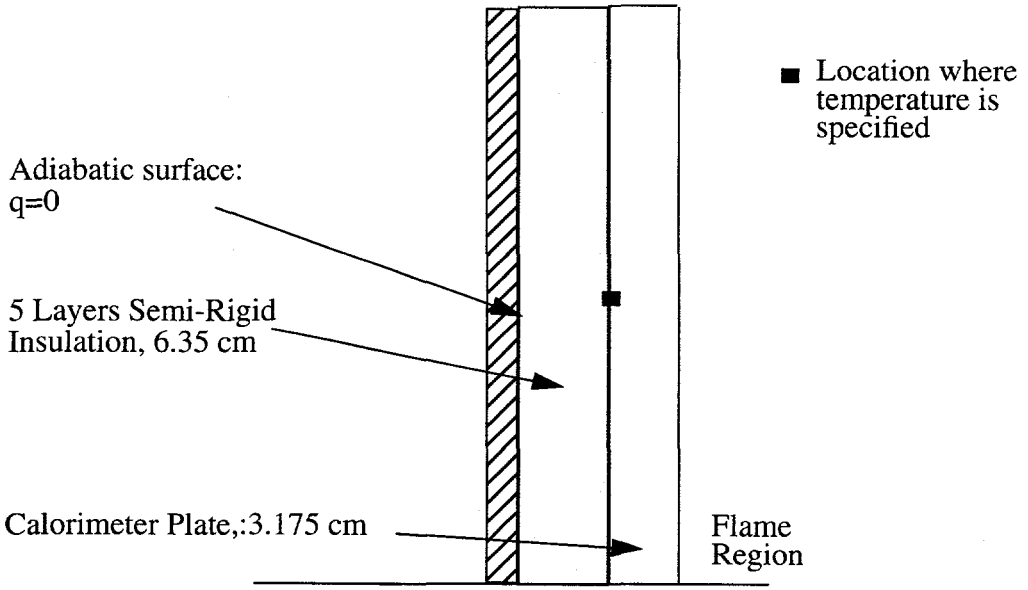

Figure B.1: Calorimeter Model Used for Inverse Calculations

Distribution

Copies	Mail Stop	Org.	Name
1	0841	9100	P. J. Hommert
1	0507	9700	K. G. McCaughey
1	0828	9102	R. D. Skocypec
1	0827	9111	W. Hermina
1	0834	9112	A. C. Ratzel
1	0835	9113	T. Bickel
1	0835	9113	R. Cochran
1	0835	9113	S. P. Burns
1	0826	9114	R. T. McGrath
1	0825	9115	W. H. Rutledge
1	0825	9115	A. R. Lopez
1	0836	9116	C. W. Peterson
15	0836	9116	L. A. Gritzo
1	0836	9116	S. R. Tieszen
1	0836	9116	V. F. Nicolette
2	0865	9735	J. L. Moya
1	0405	12333	D. D. Carlson
1	1139	6423	T. Y. Chu
1	0717	6642	J. A. Koski
1	0737	6412	S. P. Nowlen
1	0483	2165	R. E. Glass
1	9018	8940-2	Central Technical Files
5	0899	4414	Technical Library
2	0619	12630	Review and Approval desk For DOE/OSTI

1 Director, Defense Special Weapon Agency
Attn: Major Joe Crews
6801 Telegraph Road
Alexandria, VA 22310-3398

1 Director, Defense Special Weapon Agency
Attn: James V. Brackett
6801 Telegraph Road
Alexandria, VA 22310-3398

1 U.S. Coast Guard R&D Center
Attn: L. Nash
1082 Shennecossett Road
Groton, CT 06340-6096

1 U. S. Department of Energy
Albuquerque Operations Office
Albuquerque Headquarters
Attn: H. T. Season
P. O. Box 5400
Albuquerque, NM 87115

1 U. S. Department of Energy
Albuquerque Operations Office
Albuquerque Headquarters
Attn: R. O. Gergen
P. O. Box 5400
Albuquerque, NM 87115

1 U. S. Department of Energy
Albuquerque Operations Office
Albuquerque Headquarters
Attn: Roger Cartee
P. O. Box 5400
Albuquerque, NM 87115

1 U. S. Department of Energy
Albuquerque Operations Office
Albuquerque Headquarters
Attn: Karl Rueb
P. O. Box 5400
Albuquerque, NM 87115

1 Exxon Production Research
Attn: J. Barnhart
3319 Marcer St.
Houston, TX 77027

1 En'Urga Inc.
Attn: Y. Sivathanu
1291-A Cumberland Ave.
West Lafayette, IN 47906

2 FAA Technical Center
Attn: Thor Eklund, Richard Lyon
Fire Research Branch, AAR-423
Atlantic City International Airport
Atlantic City, NJ 08405

1 JM Technical
Attn: J. Mansfield
531 NW Canyon Drive
Redmond, OR 97756

1 K-Tech Corp.
Attn: Ned Keltner
901 Pennsylvania NE
Albuquerque, NM 87110

1 Lawrence Livermore National Laboratories
Attn: Doug Stevens
P. O. Box 808, L-85
Livermore, CA 94550

1 Logicon RDA
Attn: Art Barondes
6940 South Kings Highway, Suite 210
Alexandria, VA 22310

1 Los Alamos National Laboratories
Attn: Ron Flurry
P. O. Box 1663, MSC931
Los Alamos, NM 87545

1 Los Alamos Technical Associates
Attn: Lou Reidl
2400 Louisiana Blvd. NE
Building 1, Suite 400
Albuquerque, NM 87110

1 Massachusetts Institute of Technology
Attn: Professor A. Ghoniem
Room 3-342
77 Massachusetts Ave.
Cambridge, MA 02139

3 National Institute of Standards and Technology
Attn: D. Evans, R. Gann, H. Baum
BFRL, Building 224
Room B250
Gaithersburg, MD 20899

1 Commander
Naval Air Warfare Center
Attn: Doug Murray
Code 528200D
China Lake, CA 93555

1 Commander
Naval Air Warfare Center - Weapons Division
Attn: Leo Budd
Code 418300D
China Lake, CA 93555-6001

1 Commander
Naval Air Warfare Center - Aircraft Division
Attn: Bill Leach
Code 43520, B562-3
Lakehurst, NJ 08733-5100

1 Commander
Naval Surface Warfare Center - Carderock Division
Attn: Usman Sorathia
Code 643, Bldg. 60
9500 MacArthur Blvd.
Bethesda, MD 20084-5000

1 NWI
Attn: Col. John Curry, Technical Director
1651 First Street SE
Kirtland AFB, NM 87117

1 NWI
Attn: Dr. Dermod Kelleher, Technical Director
1651 First Street SE
Kirtland AFB, NM 87117

1 NWIE
Attn: Micheal Martinez
1651 First Street SE
Kirtland AFB, NM 87117

1 PLG Inc.
Attn: David Johnson
4590 MacArthur Blvd. Suite 400
Newport Beach, CA 92660

1 Purdue University
Attn: Prof. J. P. Gore
Thermal Sciences and Propulsion Center
West Lafayette, IN 47907-1003

2 SINTEF/Norwegian Institute of Technology
Attn: J. Holen, B. Magnussen
Applied Thermodynamics
Kolbjorn, Hejes Vei 1B
Trondheim, Norway N-7034

1 University of Connecticut
Attn: Professor B. M. Cetegen
Department of Mechanical Engineering
191 Auditorium Rd.
Storrs, Connecticut 06269-3139

1 University of Kentucky
Attn: Professor K. Saito
Department of Mechanical Engineering
Lexington, Kentucky 40506

1 University of Notre Dame
Attn: Professor K. T. Yang
Aerospace & Mechanical Engineerging Dept.
Notre Dame, Indiana 46556

1 Wright Laboratories
Attn: M. Bennett
FIVS Bldg. 63
1901 Tenth Street
Wright Patterson Air Force Base, Ohio 45433-7605

1 Wright Laboratories
Attn: M. Roquemore
POSC Bldg. 490
1790 Loop Road N.
Wright Patterson Air Force Base, Ohio 45433-7103